THESIS

CHARACTERIZATION OF SCANDIUM OXIDE THIN FILMS FOR USE IN INTERFERENCE COATINGS FOR HIGH-POWER LASERS OPERATING IN THE NEAR-INFRARED

Submitted by

Erik M. Krous

Electrical and Computer Engineering Department

In partial fulfillment of the requirements

For the Degree of Master of Science

Colorado State University

Fort Collins, Colorado

Summer 2010

COLORADO STATE UNIVERSITY

July 13, 2010

WE HEREBY RECOMMEND THAT THE THESIS PREPARED UNDER OUR SUPERVISION BY ERIK M. KROUS ENTITLED CHARACTERIZATION OF SCANDIUM OXIDE THIN FILMS FOR USE IN INTERFERENCE COATINGS FOR HIGH-POWER LASERS OPERATING IN THE NEAR-INFRARED BE ACCEPTED AS FULFILLING IN PART REQUIREMENTS FOR THE DEGREE OF MASTER OF SCIENCE.

Committee on Graduate Work

Mario C. Marconi

John D. Williams

Advisor: Carmen S. Menoni

Department Head: Anthony A. Maciejewski

ABSTRACT OF THESIS

CHARACTERIZATION OF SCANDIUM OXIDE THIN FILMS FOR USE IN INTERFERENCE COATINGS FOR HIGH-POWER LASERS OPERATING IN THE NEAR-INFRARED

The work presented in this thesis aims to investigate scandium oxide (scandia), deposited using dual ion beam sputtering, as a high-index material for interference coatings to be implemented in high-power lasers. Ion beam sputtered scandia coatings have the potential to allow for the power scaling of high-power lasers operating in the near-infrared. Ion beam sputtering is the technique currently used by many commercial companies to produce low-loss, high-damage-threshold coatings required by lasers operating with high fluences.

The development of scandia, and other thin film materials, requires the reduction of defects in the material through modification of growth processes and post-deposition treatment. Material defects give rise to absorption of laser light and laser-induced damage initiation sites. The growth parameter investigated in this work is the oxygen partial pressure in the deposition chamber during the reactive sputtering process of a metal Sc target to form Sc_2O_3. The film properties are sensitive to the oxygen partial pressure. At 2 µTorr oxygen partial pressure, the films are metallic and highly absorbing with an absorption, at $\lambda = 1.064$ µm, of $> 10^4$ ppm. The absorption decreases to 10 ppm at 5 µTorr oxygen partial pressure and at 38 µTorr, the absorption reaches a value of 35 ppm. This, along with the increase in absorption near the optical band edge, suggests an increase in shallow-type defect concentrations for increasing oxygen partial pressures. The observed defects contain unpaired elec-

trons, as assessed by electron paramagnetic measurements, that have a paramagnetic absorption signal with principle g-values $[g_{xx}, g_{yy}, g_{zz}] = [2.018, 2.019, 2.058]$. Generally, the concentration of the paramagnetic species increased with increasing oxygen partial pressure. These spin defects are possibly O_2^- interstitials in the deposited films. These defects contribute to an approximately 40% increase in the film stress observed in x-ray diffraction measurements and measurements of stress-induced fused silica substrate curvature.

Erik Mitchell Krous
Electrical and Computer Engineering Department
Colorado State University
Fort Collins, CO 80523
Summer 2010

Acknowledgments

This work was supported by the Office of Naval Research and Joint Technology Office from the United States Department of Defense.

The PCI data presented was taken at Stanford University by Dr. Ashot Markosyan. Dr. Dinesh Patel made some of the surface roughness measurements and Dr. Pat McCurdy took some of the XPS data, both at Colorado State University. Aid was also received from Colorado State's Dr. Sandeep Kohli and Don Heyse in using the EPR, XRD, VASE and FTIR equipment.

I thank my friends who worked with me on this and other thin film studies: Dr. Dinesh Patel, Peter Langston, Jonathan Tollerud and Dr. Ben Langdon.

I appreciate the work of my committee members, Dr. John Williams and Dr. Mario Marconi, for their revisions and aid in completing this thesis.

I also thank my thesis adviser, Dr. Carmen Menoni, for her support and guidance of this thesis and all of my research at Colorado State Univesity.

Contents

List of Tables

List of Figures

Chapter 1

Introduction

This introductory chapter provides the background theory that leads into the motivation for the experiments discussed in this thesis on the growth and characterization of scandium oxide (scandia) thin films.

1.1 Project Background

This section covers the background theory in this project concerned with the research and development of multilayer dielectric interference coatings for high-power lasers operating in the near-infrared wavelength regime. First is a discussion on the basic theory of lasers and the free electron laser at Jefferson National Laboratory for which the interference coatings are designed. Also, the requirements of the coatings will be discussed, followed by the theory and design of dielectric interference coatings. The nature of the dielectric materials chosen for study and the fundamental processes of radiation absorption and damage mechanisms will then be presented.

1.1.1 High-power lasers: the free-electron laser at Jefferson National Laboratory

"Laser" is an acronym for "light amplification by the stimulated emission of radiation." Consider Figure 1.1(a)-(c), which is a schematic of two possible discrete energy

levels that an electron can have in an atom.

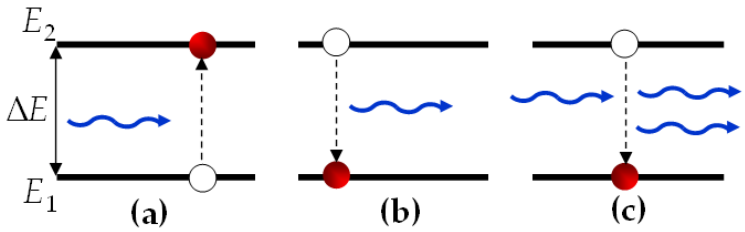

Figure 1.1: Schematic of absorption (a), spontaneous emission (b) and stimulated emission (c) of photons in a two-level system.

The two levels are separated in energy by ΔE. The most probable energy state for an electron is the lowest energy level E_1 based on the Maxwell-Boltzmann distribution.[1] The electron can be promoted into the higher energy state E_2 when sufficient energy is absorbed, for instance, from a photon with energy $\geq \Delta E$ (see Figure 1.1(a)). The excited electron will tend to decay into E_1 in an average time τ_{21} after excitation, thus emitting a photon with energy ΔE to conserve energy, in a process called spontaneous emission (Figure 1.1(b)). A second deexcitation process is possible where a photon of energy $\approx \Delta E$ induces or stimulates the excited photon to jump back to energy state E_1 and emit a photon of energy ΔE (Figure 1.1(c)). In the stimulated emission process, the emitted light propagates in the same direction, with the same polarization and in phase with the stimulating light, effectively duplicating and amplifying the incident light.[1] Lasers can operate in continuous-wave (CW) mode, where the emission is constant over time, or in pulsed mode, where the radiation is emitted in discrete pulses in time characterized by the peak power, pulse width and repetition rate of the pulses. The time-averaged power delivered by CW lasers is typically higher than that of pulsed lasers, while pulsed lasers typically deliver higher instantaneous power at the peak of a pulse.

A schematic of the typical laser is given in Figure 1.2.

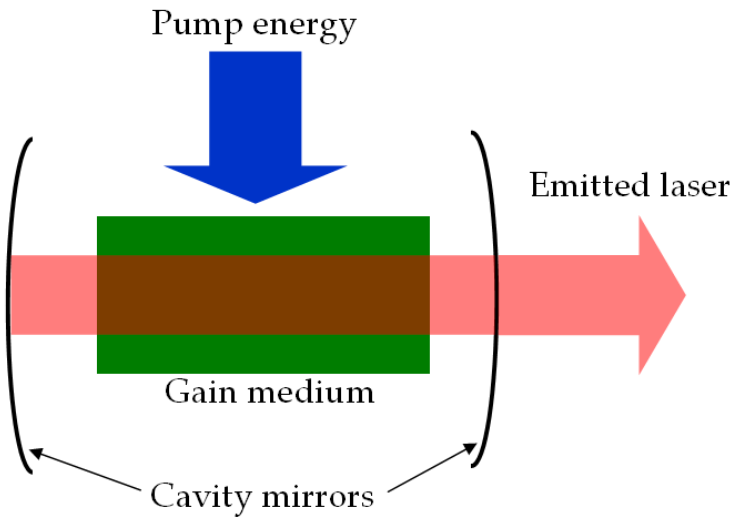

Figure 1.2: Schematic of the typical laser.

The gain medium is matter in which spontaneous emission is amplified via the stimulated emission process such that the emitted light is monochromatic, directional and in phase (coherent). Each emitted photon can stimulate other photon emissions and an avalanche effect occurs. In order for a material to function as a gain medium, population inversion must be achieved. In other words, energy must be pumped into the material such that more atoms have electrons in the higher energy state E_2 than in the lower energy state E_1. The light amplification is further increased by making photons pass through the gain medium multiple times by creating an optical cavity enclosed by mirrors. One of the mirrors is nearly perfectly reflecting while the other (the output coupler) is partially transmitting to allow some light to escape the cavity and be a useful laser. The maximum output power of a laser is generally determined by the net gain in the gain medium, how much light is lost from the cavity mirrors due to scatter and absorption of the light and the maximum fluence (energy per area) the cavity mirrors and gain medium can support without being damaged.

A free electron laser (FEL) has the same basic components of a typical laser (pump energy, gain medium and cavity mirrors) except that instead of relying on discrete atomic electron energy transitions, optical gain is produced by accelerated free electrons. A schematic of the Jefferson National Laboratory (JLab) FEL is given in Figure 1.3.

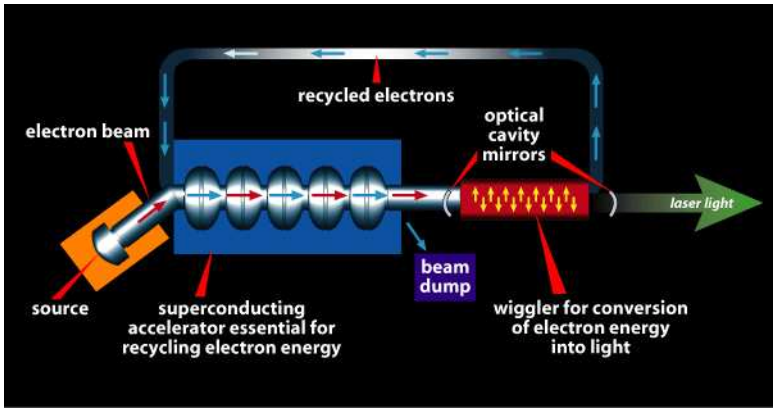

Figure 1.3: Schematic of the FEL at JLab. Taken from Ref 2.

The free electrons are generated in bunches through photoemission from a cesiated GaAs wafer.[3;4] The electron bunches are accelerated in a superconducting radio frequency (SRF) linear accelerator (linac), which makes use of the near-zero electrical resistance of cryogenically cooled niobium and Lorentz force generated by azimuthal temporally-sinusoidal magnetic fields.[5] The accelerated electrons travel, at relativistic speeds, into a wiggler inside an optical cavity, which acts like the laser gain medium.

The wiggler consists of a series of magnets with consecutive magnets having opposite polar orientations. The force on the electrons moving with velocity $\mathbf{v}$ due to a magnet with field strength $\mathbf{B}$ is $\mathbf{F} = -e\mathbf{v} \times \mathbf{B}$. The alternating magnets cause the electrons to change direction such that they oscillate, or "wiggle," in a plane perpendicular to the magnet dipole orientation. The oscillating electrons emit synchrotron radiation at the frequency of their oscillation in the wiggler (the fundamental), as well as higher harmonics (frequencies with integer multiples of the fundamental).[1] The wiggler oscillation frequency is dependent on the velocity and the geometric frequency of the magnets. The wavelength of emitted radiation can be tuned by tuning the wiggler oscillation frequency. The coupling of the radiation and electron-oscillation frequencies ensures the coherence of the light; furthermore, the co-propagation of the radiation field of the correct frequency stimulates further radiation from the oscillating electrons causing optical amplification as in a typical laser.[6]

High-power lasers, like the FEL, make use of multilayer interference coatings to produce the proper reflectivities from cavity mirrors. The design and theory of multi-

layer interference coatings will be discussed in the following section. The ability of the mirrors to withstand high laser irradiances (energy per area) will allow for higher output power from the laser. The JLab FEL imposes other challenges on the performance of the cavity optics.[7] The output of the FEL of concern is in the wavelength range 1 to 10 μm, with pulsewidths $<$ 1 ps and output powers $>$ 10 kW. The cavity optics are exposed to harmonics of the fundamental (with wavelengths at integer multiples of the fundamental wavelength) and are subject to deformation upon absorption of radiant energy.[7] Sufficiently large distortions in the cavity mirrors causes saturation of the laser output power.[8]

1.1.2 Theory and design of dielectric interference coatings

As discussed in the previous section, many lasers utilize an optical cavity, consisting of a highly reflecting mirror and a partially reflecting ($\simeq$ 90% reflecting) output-coupler mirror, to increase the rate of stimulated emission in the gain meadium. The mirrors consist of a stack of transparent layers of contrasting optically properties with precise thicknesses. With these multilayer coatings the amount of incident light reflected and transmitted can be controlled for a given wavelength, incident angle and polarization. In the case of a laser cavity, one mirror needs to reflect all light to contain it in the cavity. The second mirror is less reflective so that some the light can escape and become the laser beam. The surface on the other side of the second mirror is made completely transmissive by an anti-reflection coating.

The propagation of light in a medium is governed by Maxwell's equations. Assuming a region of isotropic space, Maxwell's equations can be expressed as

$$\nabla \times \mathbf{E} = -\mu \frac{\partial \mathbf{H}}{\partial t}, \tag{1.1}$$

$$\nabla \times \mathbf{H} = \sigma \mathbf{E} + \epsilon \frac{\partial \mathbf{E}}{\partial t}, \tag{1.2}$$

$$\nabla \cdot \mathbf{E} = \rho \tag{1.3}$$

and

$$\nabla \cdot \mathbf{H} = 0, \tag{1.4}$$

where $\mathbf{E}$ and $\mathbf{H}$ are the electric field and magnetic field vectors, respectively.[9] The region of space is characterized by the permeability μ, the conductivity σ, the charge density ρ and the permittivity ϵ. A solution of Maxwell's equations for periodic fields $\mathbf{E}$ is $\mathbf{E} = \mathbf{E_0} \cos\left[i\omega(t - z/v)\right]$ (with a similar expression for $\mathbf{H}$ with the directions of $\mathbf{E_0}$, $\mathbf{H_0}$ and $\mathbf{z}$ being mutually orthogonal). This is the equation of a traveling wave moving along $\hat{z}$ with speed v and angular frequency ω and with a vector amplitude with components along the x- and y-directions. Also necessary for this polarized plane-wave to be a solution to Maxwell's equations, the equation

$$\frac{\omega^2}{v^2} = \omega^2 \epsilon\mu - i\omega\mu\sigma \tag{1.5}$$

must be satisfied.[9] In free space, $\epsilon = \epsilon_0$, $\mu = \mu_0$, $\sigma = 0$ and the speed of the traveling wave is $c = (\epsilon_0\mu_0)^{-1/2}$. Multiplying Equation 1.5 by $(c/\omega)^2$ gives

$$\tilde{n}^2 \equiv \frac{c^2}{v^2} = \frac{\epsilon\mu}{\epsilon_0\mu_0} - i\frac{\mu\sigma}{\omega\epsilon_0\mu_0}. \tag{1.6}$$

Taking the square root and renaming variables, the equation for the complex refractive index is

$$\tilde{n} = n + i\kappa \tag{1.7}$$

The interpretation of n for a given medium is that it is the ratio of the velocity of the light wave in free space to the velocity of light in the medium. When $\kappa \neq 0$, a decay term $\exp\left(-2\pi\kappa z/\lambda\right)$ is multiplied to the amplitude of the traveling wave of wavelength λ. In other words, κ is related to the absorption of the medium.

The operating principle of multilayer interference coatings is reflection at an interface of two dielectric materials (materials for which $\sigma = \kappa = 0$) of contrasting refractive index n. The reflected and transmitted waves add (interfere) to produce a net reflectivity and transmissivity. Light incident on an interface is diagrammed in Figure 1.4.

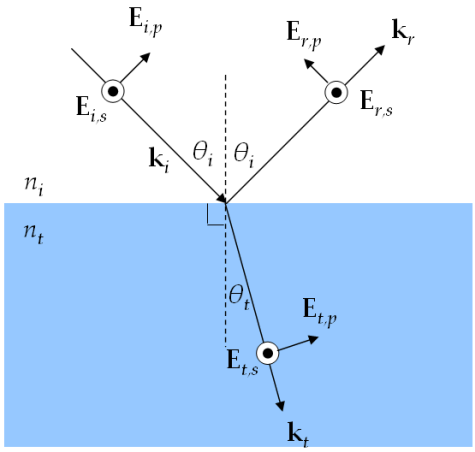

Figure 1.4: Schematic of the simple dielectric interface showing the components of the polarized electric field and the angles, relative to the interface normal, of the incident, reflected and transmitted light.

The arrows represent rays, or the direction of propagation of the plane waves, where $\mathbf{k}$ has a magnitude $2\pi/\lambda$ and its direction is that of propagation. Incident light is reflected specularly (at the same angle as the incident ray) while light is transmitted at an angle such that Snell's law, $n_i \sin(\theta_i) = n_t \sin(\theta_t)$, is satisfied.[1] The ratio of the amplitudes of the reflected electric field and incident electric field is denoted $r_{p,s}$ while the ratio of amplitudes of the transmitted and incident electric field is $t_{p,s}$ and are called the Fresnel amplitude reflection and transmission coefficients, respectively. The p and s subscripts represent the p- and s-polarized components of the fields, relative to the interface, as shown in Figure 1.4. The Fresnel coefficients, determined from solving Maxwell's equations at an abrupt interface, are

$$r_s = \frac{n_i \cos\theta_i - n_t \cos\theta_t}{n_i \cos\theta_i + n_t \cos\theta_t}, \tag{1.8}$$

$$r_p = \frac{n_t \cos\theta_i - n_i \cos\theta_t}{n_i \cos\theta_t + n_t \cos\theta_i}, \tag{1.9}$$

$$t_s = \frac{2n_i \cos\theta_i}{n_i \cos\theta_t + n_t \cos\theta_t} \tag{1.10}$$

and

$$t_p = \frac{2n_i \cos\theta_i}{n_i \cos\theta_t + n_t \cos\theta_i}.^{[1]} \tag{1.11}$$

The simplest thin film coating structure is shown in Figure 1.5(a) (refraction of the transmitted beams has been schematically ignored).

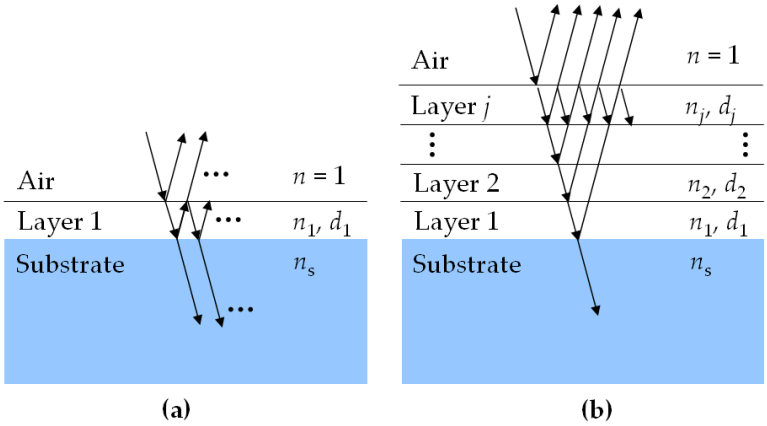

Figure 1.5: Schematic of a single thin dielectric layer on a substrate with air as the incident medium (a) generalized to a stack of j layers with refractive index n_j and thickness d_j on a substrate with refractive index n_s (b). A select number of the infinite number of reflected and transmitted light rays at each interface are represented.

A thin transparent layer (negligibly small κ at the wavelengths of interest) is placed on a smooth, thick solid (the substrate). The terms "thick," "thin" and "smooth" are relative to the wavelength of incident light λ. The fluctuations in a smooth surface are fractions of λ. Thin layers are $\sim \lambda$ and thick layers are $>> \lambda$. The light reflected from layer 1 is a sum of the light reflected at the initial air-layer interface and subsequent transmitted beams, into the air, that have undergone multiple reflections at the layer-substrate and the air-substrate interfaces. Likewise, the beam transmitted through the structure is a sum of multiple beams traveling in the same direction. The amplitude

of the reflected and transmitted electric fields (and the intensity, which is $I \propto \mathbf{E}^*\mathbf{E}$) is diminished at each interface according to Equations 1.8 to 1.11. The total reflection from the structure is the summation of the electric fields traveling against the direction of the incident field in the incident air medium. For a given free-space wavelength λ_0 and film thickness d_1, the summation of the reflected beams is a maximum when the equation

$$d_1 \cos(\theta_1) = (2m+1)\frac{\lambda_1}{4} \tag{1.12}$$

is satisfied, where θ_1 is the angle (relative to the surface normal) of the transmitted beam into the film, $\lambda_1 = \lambda_0/n_1$ is the wavelength of the light as it propagates in the film, and $m = 0, 1, 2, ...$ is an integer.[1] Similarly, a minimum in the observed intensity is seen when

$$d_1 \cos(\theta_1) = 2m\frac{\lambda_1}{4}.^{[1]} \tag{1.13}$$

In this case, m cannot be 0.

Due to energy conservation, a maximum in the reflected intensity from the structure corresponds to a minimum in the transmitted intensity. The calculated intensity reflectance and transmittance versus wavelength of illumination are shown in Figure 1.6 for a layer of TiO_2 200 nm thick on SiO_2 (the substrate), where, at $\lambda_0 = 500$ nm, $n_1 = 2.4$ and $n_s = 1.5$.

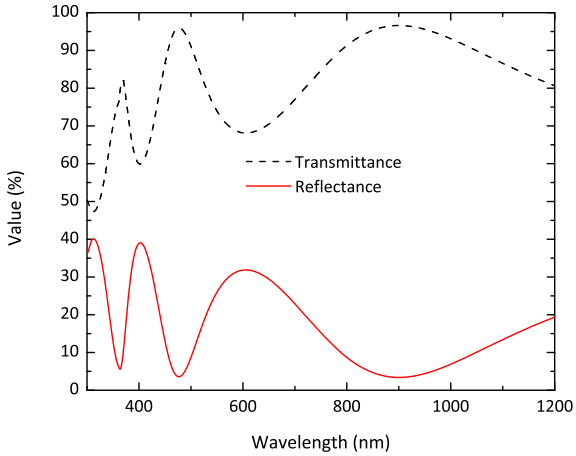

Figure 1.6: The reflectance and transmittance (reflected and transmitted intensities normalized to the incident intensity, respectively) for a 200-nm thick TiO_2 layer on an SiO_2 substrate at various wavelengths of incident illumination.

The calculation was done using the Essential Macleod thin film design software package.

A schematic of a generalized thin film filter is shown in Figure 1.5(b). The jth material is characterized by its thickness d_j and its refractive index n_j. Two special cases, which are relevant to the this work, will now be considered: high reflecting (HR) coatings and anti-reflection (AR) coatings. With HR coatings, the goal of the designer is to maximize the reflectance (or attain a specified value of reflectance for a laser output coupler (OC)) of the thin-film structure over a wavelength range. Considering Equation 1.12 for a single layer, at normal incidence, at a given wavelength λ_0, depositing a layer with refractive index n_1 and thickness $d_1 = \lambda_0/(4n_1)$ produces a maximum reflectance. If a second layer with $n_2 \neq n_1$ and thickness $d_2 = \lambda_0/(4n_2)$ is deposited on top, then the reflectance at both interfaces is high and the total reflectance from the structure is increased. One can generalize, depositing two different materials in alternating fashion, for a total of $(2p+1)$ layers, with $d_j = \lambda_0/(4n_j)$ and with either the odd or even layers having a relatively high index n_H compared to the other layers with lower index n_L such that the total reflectance of the multilayer stack is[9]

$$R = \left(\frac{1 - (n_H/n_L)^{2p}(n_H^2/n_s)}{1 + (n_H/n_L)^{2p}(n_H^2/n_s)} \right)^2 . \tag{1.14}$$

Equation 1.14 shows that maximizing the reflectance from a HR stack involves maximizing the number of layers (p) and the ratio n_H/n_L. Often, in the case of OC design, for a given n_H/n_L, p is chosen to reach the desired value of R. The Essential Macleod calculation of the reflectance of an HR design at $\lambda_0 = 1064$ nm for 15 pairs of HfO_2 ($n_H = 1.97$ at $\lambda_0 = 1064$ nm) and SiO_2 ($n_L = 1.45$ at $\lambda_0 = 1064$ nm) on an SiO_2 substrate is given in Figure 1.7.

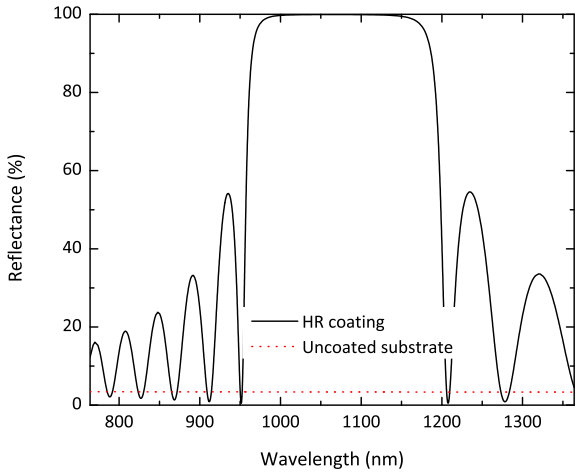

Figure 1.7: Calculated reflectance of a 15-pair quarter-wave stack of HfO_2 and SiO_2 on a SiO_2 substrate HR coating at $\lambda_0 = 1064$ nm with the reflectance of an uncoated substrate for comparison.

AR coating designs are less straight forward than HR coatings, with the goal to minimize R, thus maximizing the transmittance T. Reference 9 gives a number of strategies for designing AR coatings. A design for $\lambda_0 \approx 1064$ nm is shown in Table 1.1, with its corresponding calculated transmittance in Figure 1.8, was developed using Essential Macleod.

Layer	Material	Thickness
1	HfO_2	$0.06\lambda_0/n_H$
2	SiO_2	$0.11\lambda_0/n_L$
3	HfO_2	$0.26\lambda_0/n_H$
4	SiO_2	$0.25\lambda_0/n_L$

Table 1.1: Four-layer AR coating design centered near $\lambda_0 = 1064$ nm. Layer 1 is nearest the SiO_2 substrate.

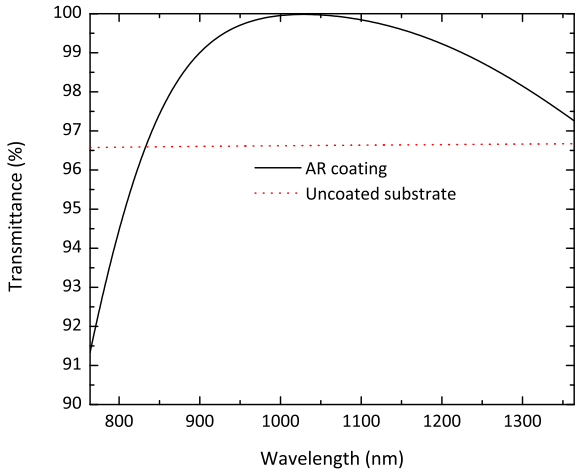

Figure 1.8: Calculated transmittance of a four-layer AR coating design (Table 1.1) on a SiO_2 substrate centered near $\lambda_0 = 1064$ nm with the transmittance of an uncoated substrate for comparison.

The design features HfO_2 and SiO_2 layers on an SiO_2 substrate and was arrived at assuming the layer structure and target of $T = 1$ at $\lambda_0 = 1064$ nm; a fitting algorithm was used to determine a thicknesses of each layer to reach the targeted T.

1.1.3 Dielectric material properties: metal oxides and the absorption and laser-induced damage mechanisms

Metal mirrors provide high reflectivities over broad wavelength ranges but lack the ability to transmit light as required by output couplers and cannot provide high reflectivities and damage thresholds and low absorption compared to dielectric interference coatings.[10] Dielectrics are the materials chosen to produce the high damage-threshold, low-loss optical coatings for power scaling of high-power lasers, including FELs. More specifically, the type of dielectrics chosen are metal oxides.

Metal oxides are inorganic materials with chemical structures of metal atoms bonded to oxygen atoms. These materials are widely used in optical coatings because of their transmissivity over visible and near-infrared wavelengths and the ability to fabricate thin layers of these materials using the methods described in the following section. Low-index materials most commonly used are SiO_2 and occasionally Al_2O_3 while high-index materials include TiO_2, Ta_2O_5, HfO_2 and Sc_2O_3. To understand why metal

oxides are used for high-performance optical coatings in the visible and near-infrared, one must understand the fundamental processes of absorption and photon-induced damage in materials. Though scattering from optical materials is a form of optical loss, it is mostly a function of the method of fabrication than an inherent property of the material. The following two subsections are dedicated to the fundamental processes of optical absorption and damage in materials.

Optical absorption in materials

Optical absorption is the phenomenon in which the energy of an incident photon is deposited into a material and converted into another form of energy such as luminescence, chemical energy, thermal energy or electrical energy resulting in heating the material.[11] The nature of the material interacting with the photons is now considered.

As alluded to in Section 1.1.1, an atom not influenced by external potentials has electrons bound with discrete energy levels as described with quantum mechanics.[12] Atoms in a solid are in close proximity and interact with each other. At large interatomic distances, the atoms do not interact but as they are brought closer together, the interatomic interaction causes the discrete energy levels to broaden into many levels, creating a nearly continuous distribution of energy levels as diagrammed in Figure 1.9 for an atom with a partially filled p-shell.[13]

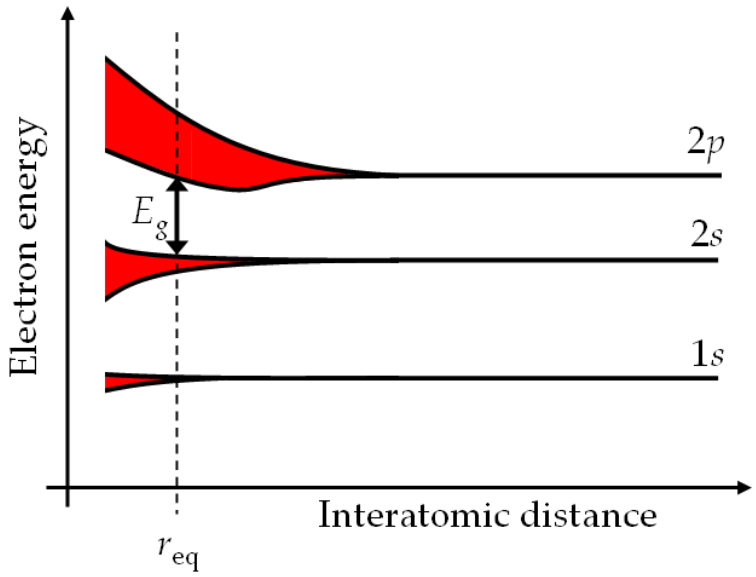

Figure 1.9: Diagram of the energy levels in atoms with a partially filled p-shell at 0 K as a function of interatomic distance. In a pure crystalline solid, the atoms are a fixed distance r_{eq} from one another. At r_{eq}, pseudo-continuous energy bands are separated by forbidden energy regions. The forbidden region between the $2s$ and $2p$ states is called the band gap and spans an energy E_g. After Tyagi.[13]

Between the pseudo-continuous energy bands are energy states that are forbidden to any electron. In a pure crystalline solid, there exists an equilibrium interatomic distance r_{eq} that the atoms maintain. The forbidden energy region between the highest completely filled energy level at absolute zero (valence band) and next highest energy level (conduction band) is called the bandgap and separates the valence band and conduction band by the bandgap energy E_g.

Photons interacting with a solid have an energy, related to their wavelength in a material λ, expressed as

$$E_p = \frac{hc}{\lambda}, \tag{1.15}$$

where h is Planck's constant and c is the speed of light in vacuum. A photon is absorbed by the material when the energy (and momentum) of the photon can be converted to another process like electron excitation. At room temperature, a vast majority of the atoms in a solid will have electrons occupying the valence band, relative to the conduction band.[13] When $E_p < E_g$, the photon does not have enough energy to

promote a valence electron to the conduction band and has a negligibly small probability of being absorbed by the material and the material is transparent to photons of these energies. When $E_p \geq E_g$, a photon has enough energy to promote an electron into the conduction band and, with some probability, the photon is lost to electron excitation in the material.

In conductors, like metals, the conduction band and valance band overlap, therefore, there is no forbidden energy gap. The electrons in a metal are modeled as a free-electron gas (Drude model) that can absorb photon energies corresponding to energies of electron oscillations.[14] The free electrons and ions in the metal are considered a plasma with the oscillating electrons having a natural plasma frequency. At optical frequencies below the plasma frequency (usually in the UV), light is strongly absorbed and above the plasma frequency the conductor is transparent.[1] Metals have reflectivities of 85% to 95%,[1] leaving the other 5% to 15% of the visible and infrared energy to be deposited into the conductor, compared to the 0.001% absorptivity for 1-cm thick fused SiO_2 at $\lambda = 1064$ nm.[15]

Insulators (dielectrics) are superior to conductors in terms of optical absorption. A table of bandgaps for some metal oxides is given in Table 1.2 with the corresponding wavelength for $E_p = E_g$.

Metal oxide	E_g (eV)	Wavelength for $E_p = E_g$
TiO_2	3.3[16]	375 nm
Ta_2O_5	3.8[16]	326 nm
HfO_2	5.1[16]	243 nm
Sc_2O_3	5.7,[17] 6.3[18]	218 nm, 197 nm
Al_2O_3	6.5[16]	191 nm
SiO_2	8.3[16]	149 nm

Table 1.2: Bandgaps of metal oxide materials used for optical coatings along with the wavelength of photons with energy $E_p = E_g$.

Table 1.2 suggests that the metal oxide materials used for optical coatings are negligibly absorbing and transparent in the visible and near-infrared wavelengths (wavelengths of interest in the development of high-power lasers). Up to this point, perfect materials have been considered. Any real material, especially a synthesized thin film,

will deviate from the ideal material. Non-idealities (impurities) will now be considered along with their effects on the energy structure and absorption of the material.

Materials in the solid state are composed of atoms in a crystal structure. A pure crystal has the same three-dimensional periodic array over the entire extent of the material. Different types of defects can occur in a crystalline lattice.[13;14] A vacancy is the omission of an atom from a point in the crystalline matrix where it is expected and an interstitial defect is an atom that is wedged in the lattice where an atom normally would not be. Substitutional impurities are defects in which an atom B is in a location where an atom A is expected. Stoichiometric defects exist where, say for compound A_xB_y, the ratio of atomic concentrations of A and B $\neq x/y$. Of relevance to this work are amorphous materials, which are solid state materials with finite order. In other words, an amorphous solid is composed of a collage of ideal crystals joined together by bonds with distorted bond angles.[19] For amorphous solids, defects are more difficult to define but exist in some form. Also, the finite extent of the material is a disturbance to the periodic array; surfaces and interfaces of materials are inherently defects (with dangling bonds, etc.). In thin films, where surface and interface regions become a higher percentage of the entire material volume, the surface and interface defects are important.

Defects in the crystal lattice and surface affect the electronic energy levels for the electrons in the solid.[13] Defects can form "donor" or "acceptor" energy levels in the energy structure of the material at E_d below the conduction band and E_a above the valence band, respectively. These so-called acceptor and donor energy levels are shown in Figure 1.10.

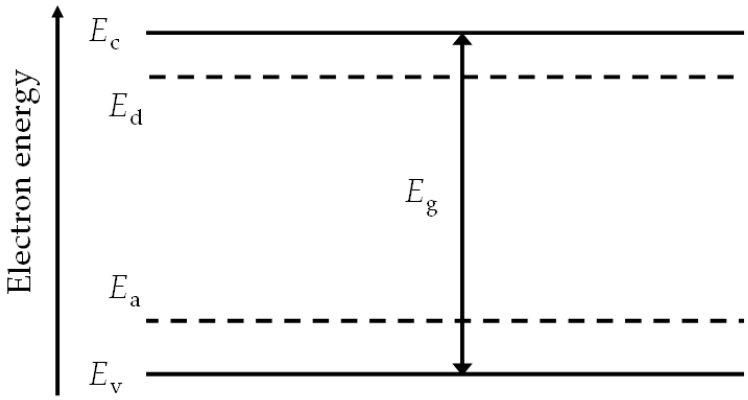

Figure 1.10: Diagram of the energy levels in a solid material with impurities creating donor (E_d) and acceptor (E_a) energy levels in the bandgap between the highest valence (E_v) and lowest conduction (E_c) band states separated by the bandgap E_g.

The acceptor and and donor levels lie near the valence and conduction bands, respectively and are referred to as shallow levels. With these available shallow states, photons with energy $E_p < E_g$ can be absorbed and excite electrons. Minimizing the absorption in engineered materials involves the reduction of impurity defects that create band states that increase the probability of photon absorption.

Laser-induced damage in materials

Laser-induced damage in a surface occurs when any permanent change is observed in the characteristics of the surface as a result of laser irradiation of the surface.[20] The mechanisms of laser-induced damage are usually considered in two regimes: the long-pulse regime (including continuous wave (CW) operation) for pulses with pulsewidths $\tau \gtrapprox 20$ ps and the short-pulse regime $\tau \leq 10$ ps.[21] Stuart *et al*. measured the damage fluence of bulk fused silica (Figure 1.11) and SiO_2/HfO_2 multilayer coatings ($\lambda = 1053$ nm and 825 nm at 10-Hz repetition rate) and saw that for $\tau \gtrapprox 20$ ps, the damage fluence increased with $\tau^{1/2}$, consistent with heat deposition into the material.[21] The long-pulse damage mechanism is now examined.

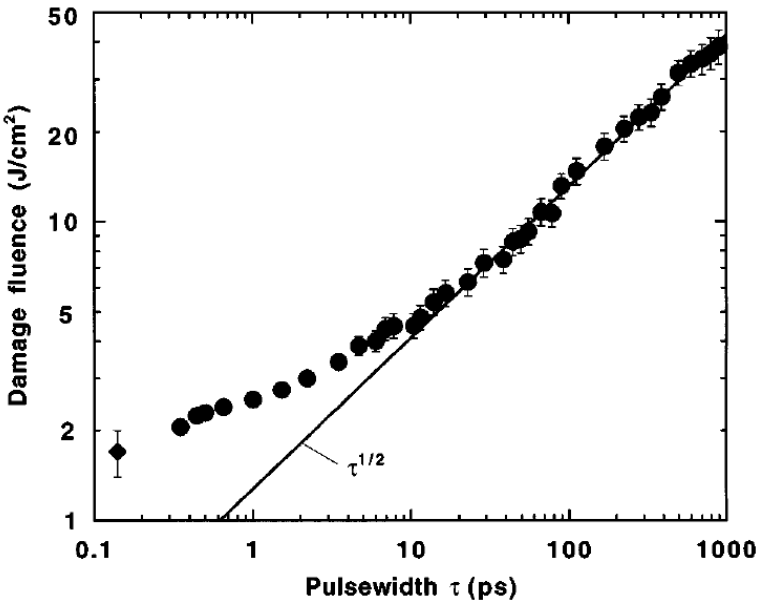

Figure 1.11: Plot of the pulsewidth dependence of the damage threshold at 1053 nm (●) and 825 nm (◆) in pure bulk fused silica taken from Stuart, *et al*.[21] The actual fit in the long-pulse regime was $\tau^{0.504}$.

The damage mechanism steps in the long-pulse regime for wide bandgap dielectrics are 1) photon absorption/electron excitation into the conduction band, 2) electron lattice heating and 3) melting followed by ablation.[22]. In oxides, more than one infrared photon ($E_p \approx 1$ eV) is still required to excite valence electrons into the conduction band. Multiphoton absorption (a non-linear process in which the energy of multiple photons excites one electron) creates conduction-band electrons in most oxide materials.[22;23] The importance of multiphoton absorption is illustrated in Figure 1.12, which shows the long-pulse (3 ns) damage fluence for a deuterated potassium dihydrogen phosphate (DKDP) crystal as a function of photon energy.

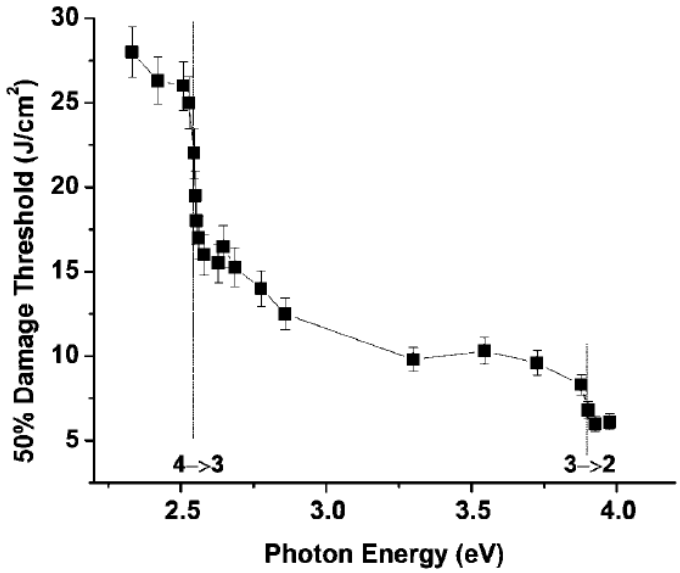

Figure 1.12: The damage threshold in a deuterated potassium dihydrogen phosphate (DKDP) crystal versus photon energy with long pulsewidths (3 ns) taken from Carr, *et al*.[23] The steps in the fluence curve correspond with transitions from two- to three-photon and three- to four-photon absorption processes.

The step transitions in the fluence curve correspond with integer fractions of the bandgap. As the number of photons required to reach the conduction band goes from two to three and three to four, the damage threshold jumps to higher values.[23] The work of Carr *et al*. also showed that certain sites within the radiated zone were damaged first, indicating discrete regions with higher concentrations of point defects. After excitation, the electrons transfer energy to and heat the material lattice through phonons,[22] where phonons are lattice vibrations with quantized energy.[14] Sufficient heating causes the irradiated region to melt, thus being damaged by the laser radiation. Ablation (removal of atoms from the solid) of the irradiated material can also occur when the heated region expands, as a rarefaction wave propagates from the surface into the material.[22]

Short-pulse damage is initiated in the same way as long-pulse damage: through multiphoton excitation of electrons. However, the pulsewidths are too short to allow for excited electrons to transfer energy to the crystal.[21] Instead, conduction band electrons transfer energy to valence electrons through collisions. Conduction band electrons are further excited by photon absorption similar to the way electrons in a

metal absorb radiation. These excited electrons have enough energy to collide with valence electrons to excite them and remain in the conduction band. This avalanche effect causes an exponential increase in the conduction band population. Once the population reaches a critical value, the conduction band electrons become highly absorbing. In turn, this gives rise to lattice instabilities and electrical breakdown. This is when femtosecond damage is considered to occur.[21;24]

Though the FEL light source output has sub-ps pulsewidths (short pulse regime), a pulse arrives at the mirrors every ≈ 50 ns,[7] making the light incident on the cavity mirrors quasi-CW. This makes the damage modeling regime for the application to the JLab FEL somewhat ambiguous. Regardless of the modeling regime, damage seems to be initiated by multiphoton absorption; a process that is enhanced by defects in the material creating energy states within the bandgap. This, along with reducing (linear) absorption, necessitates depositing materials with low defect concentrations. The metal oxides mentioned here are good choices for materials because of the relatively high bandgaps.

1.1.4 Modern thin film deposition techniques

This section is focused on describing the subset of modern deposition techniques used to deposit thin films for optical coatings. Deposition processes are categorized as either chemical vapor deposition (CVD), where vapor-phase chemical reactions are used to form a solid thin film or physical vapor deposition (PVD), where physical methods (i.e. thermal and momentum transfer) are used to create a vapor-phase material to be deposited. A single deposition process can be a hybrid of CVD and PVD. The CVD processes covered here are atomic layer deposition (ALD) and plasma-enhanced chemical vapor deposition (PECVD). The PVD processes discussed are evaporation (both thermal and electron beam) and magnetron sputtering. The combination of PVD and CVD methods is called reactive evaporation or reactive sputtering. Reactive PVD is required when forming a compound, such as a metal oxide, when using a metal source material. The reactive gas, like oxygen, is flowed into the chamber to chem-

ically react with the condensed metal to form a compound, as in the CVD method. Reactive ion beam sputtering is the focus of this thesis and is covered in Section 2.1.

A schematic of a CVD system is given in Figure 1.13.

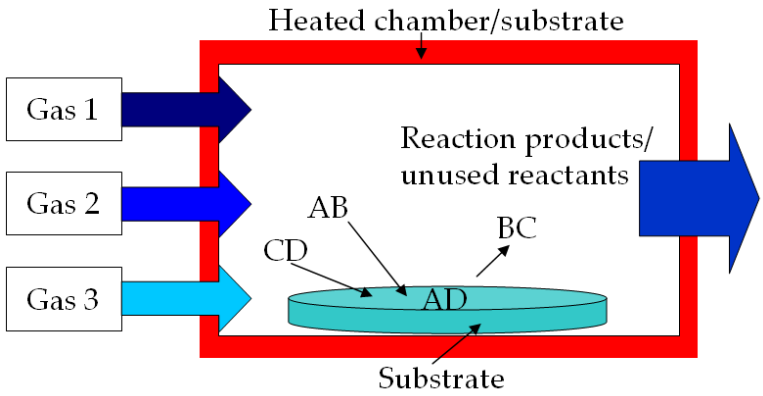

Figure 1.13: A schematic of the general CVD process. Precursor gases are flowed into a reaction chamber where chemical reactions occur forming desired chemical compounds on the surfaces in the chamber.

CVD involves a vacuum chamber containing substrates, which are both heated. Precursor gases of compounds containing elements desired for the thin film are flowed into the chamber at precisely controlled flow rates. The gases diffuse to all surfaces in the chamber and adsorb at the surfaces. Following adsorption, events such as dissociation, surface diffusion and chemical reaction occur. Products then can diffuse away from the surface or desorb from the surface.[25;26] Reaction byproducts and unreacted reactants are pumped from the vacuum chamber. An example CVD reaction for forming SiO_2 is

$$SiH_{4(g)} + O_{2(g)} \longrightarrow SiO_{2(s)} + 2H_{2(g)}, \tag{1.16}$$

where the subscripts represent the molecules in the gas (g) and (s) phases and the precursor gases are O_2 and SiH_4.[25] Hydrogen gas is a byproduct of the reaction while SiO_2 forms at the surface continually to form a film. Often, a non-reactive diluent (carrier) gas like N_2 is used to dilute the precursors and reduce spontaneous reactions between the precursor gases.[25]

The properties of a deposited film are fundamentally related to the chemical com-

position and mechanical structure of the film. Process parameters affecting the composition and structure of the film include relative gas flow rates, gas compositions, substrate temperature, reactor wall temperature, substrate surface conditions and impurities in the chamber and gases.[25]

Advantages of the CVD process include the ease of achieving a desired stoichiometry, the ability to form conformal coatings (all surfaces are coated evenly regardless of topography as apposed to PVD processes, which are directional) and the packing density of the films is relatively high, leading to high refractive indices and minimal water absorption in the film.[10] The main disadvantages of using CVD are that the deposited films are usually stressed tensively and may include organic impurities when organic precursors are used.[10]

A variation of the CVD process is plasma enhanced CVD (PECVD), where a plasma discharge of the process gases is generated. For example, a microwave pulse can be propagated into the reaction chamber that ionizes the process gases. Some of the advantages of using the plasma process is enhanced film properties and faster deposition rates without the need to heat the deposition chamber and substrates.[10]

The final variation of CVD discussed here is atomic layer deposition (ALD) in which the CVD is performed in a series of steps. Each precursor is flowed in individually, depositing a single layer of atoms (a monolayer) in one cycle step. To form a binary compound AB, the precursor containing A is flowed in with a carrier gas like N_2. A monolayer of A is deposited on all surfaces, then the system is purged using the carrier gas. Then, the precursor containing B is flowed into the reaction chamber and reacts with the monolayer of A to form a monolayer of the compound AB. The cycle is completed with a final purge. The cycle is repeated until the proper number of monolayers has been formed to achieve the desired layer thickness. The obvious disadvantage of this method is the increased time of layer deposition. The advantages include precise control and repeatability of film thickness and uniformity of composition and properties over the area and thickness of the deposited films.[27]

The next set of thin film deposition techniques are the PVD processes. Schematics

of the thermal (a) and electron beam (b) evaporation systems are given in Figure 1.14. A thermal evaporator consists of a vacuum chamber containing substrates and source material placed in a metallic vessel. Current is passed through the vessel, which is resistively heated, and the source material begins to melt and evaporate in the low-pressure atmosphere. The evaporated material condenses on the substrates. The substrates are typically rotated in order to make the coating more uniform as the vapor of evaporated material is highly directional. The directionality of the vapor flux also makes the coating non-conformal, thus making the use of smooth substrates a necessity. Though relatively cheap and easy to use, thermal evaporation produces porous films, requires source materials that can be melted with resistive heating (mainly metals) and is a "dirty" process in that the heated metal and source material can mix and heated elements in the vacuum chamber off-gas and introduce high impurity concentrations into the film.

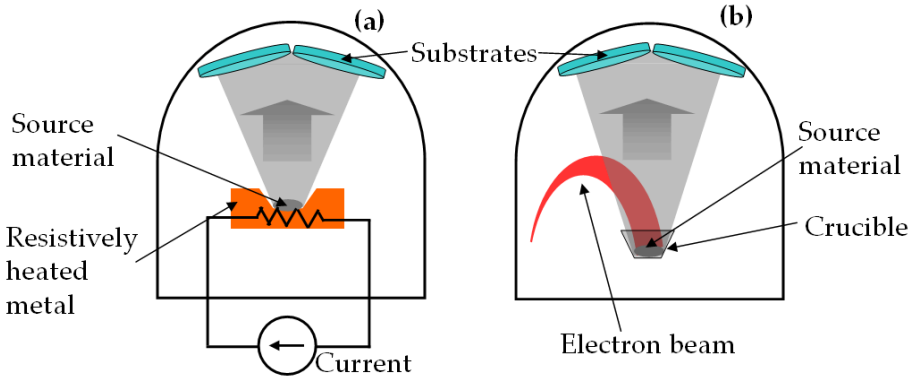

Figure 1.14: Schematic of a thermal evaporator (a) and electron beam evaporator (b). The source material is heated, melted and evaporated. The vapor condenses on substrates.

The electron beam deposition process is similar to thermal evaporation except that the vapor of the source material is generated by magnetically bending an electron beam onto the source material held in a water-cooled crucible. Electron beam deposition is the most widely used method for depositing optical coatings.[28] Electrons are generated through thermionic emission from a cathode and accelerated through electrical potentials between 3 kV to 9 kV, corresponding to energies of 3 keV to 9 keV.[10]

Electron beam evaporation is superior to thermal evaporation in that local heating by the electron beam makes the process more efficient, oxides can be directly evaporated and contamination from a filament/boat is avoided.[10] Electron beam evaporated coatings are still porous, causing refractive index shifts in the films, when exposed to humidity, due to water absorption in the film.[28] In both the near-infrared and UV wavelength regimes, electron-beam deposited coatings have relatively high damage thresholds as reported by Gallais, *et al*., for 11-ns pulses at 10-Hz repetition rates.[29]

The density of the deposited films is dependent on the mobility of the atoms adsorbed to the substrate surface.[28] The addition of energy via an ion beam, directed at the substrate surface, can increase the surface mobility and increase the adhesion and packing density of the films.[10;28] The addition of the ion "assist" beam to electron beam evaporation is termed ion beam assisted deposition (IBAD). Ion beams will be discussed more thoroughly in Section 2.1.2. Though the surface roughness and density of the films increase using IBAD, the films have slightly lower damage thresholds than those grown by conventional electron beam evaporation.[28]

Instead of heating a material and evaporating it, a vapor can be created from a solid through momentum transfer collisions from bombarding ions. This process of removing surface atoms from a solid through momentum transfer is called sputtering.[30] The process of sputtering will be considered in greater detail in Section 2.1.3. The two sputtering techniques most commonly used are magnetron and ion beam sputtering. A schematic of a planar magnetron sputtering system is shown in Figure 1.15. Argon, or other sputtering gases, are flowed into an evacuated chamber. The sputtering target (source material) is negatively biased relative to system ground near 600 V.[10] The bias is either DC or radio frequency. DC magnetron sputtering is often used for sputtering of a metal, while RF magnetron sputtering is used on insulating targets.[31] Magnets generate a magnetic filed near the target surface, which is perpendicular to the electric field, confining any electrons ($\mathbf{F} = -e\mathbf{v} \times \mathbf{B}$) to circular paths near the target. Electrons collide with neutral argon atoms and generate Ar ions in an Ar plasma (discussed in Section 2.1.2). The electrons eventually escape due to the

repulsion of the negatively-charged target but the circular path increases the probability of collision with a neutral atom. The positively-charged argon ions are accelerated towards the negatively charged sputtering target with enough energy to knock out surface atoms from the target forming a vapor of the target material. The target material vapor then condenses on a substrate placed above the target. In the sputtering process, electrons are also emitted from the target (called secondary electrons) that participate in collisions with the Ar gas, generating more ions for the sputtering process. As with evaporation, magnetron and other sputtering techniques can be assisted by ion beams.

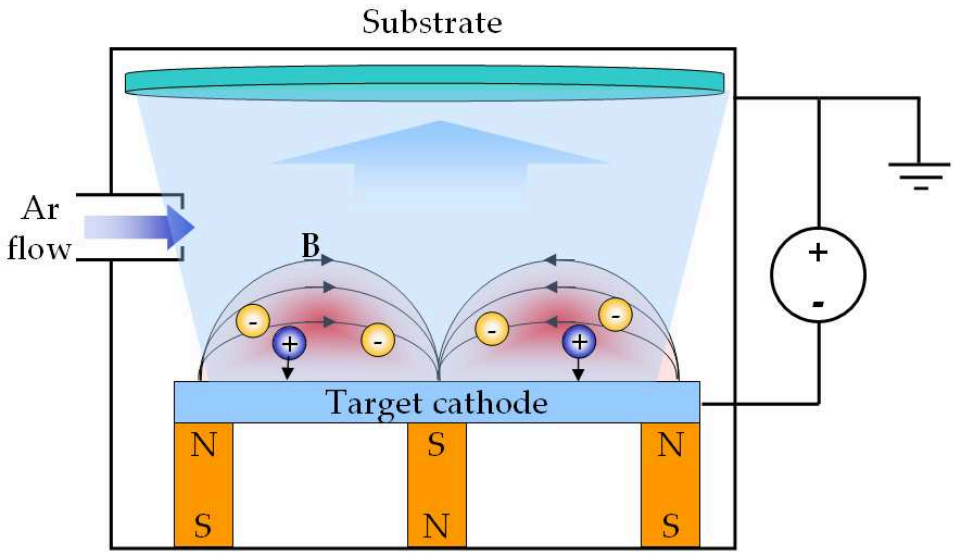

Figure 1.15: Schematic of a planar magnetron sputtering system. Secondary emitted electrons, from the target, are confined by a magnetic field. The electrons collide with Ar (or other sputtering gases) to ionize them. The ionized atoms are accelerated towards the target and remove surface atoms, creating a vapor that condenses on the substrate above the target.

The advantage of magnetron sputtering, and all sputtering processes, over evaporative processes is the increased kinetic energy of the atoms arriving at the substrate (by $\sim 10\times$).[10] This leads to higher packing densities and stable, dense films. The high energy of deposition also typically results in compressive stresses in sputtered films.[32] Magnetron sputtering is used to deposit large-area optical coatings.[31;32] Three of the top manufacturers of optical coatings for high power lasers use ion beam sputtering (IBS) to fabricate high performance optical coatings due to the robustness,

low scattering, low absorption and high-damage thresholds of the films and repeatability and control of the process.[33;34;35] Ion beam sputtering is a process in which a target is ablated by a beam of ions that is generated in an ion source and accelerated toward the target. The generation of the ion beam is independent of the substrate and target.

The main advantages of ion beam sputtering over magnetron sputtering include the independence of the substrates and target from the process plasmas, the lower process pressure that can be maintained (magnetron sputtering requires a higher gas pressure to maintain the discharge plasma), the ability to control substrate temperature and independent control of the sputtering energy, flux and angle, resulting in a more controlled process and fewer defects.[36;37] Chapter 2 is dedicated to the method and characterization of ion beam sputtered coatings.

1.2 Project Motivation and Previous Work

1.2.1 Previous work

Sc_2O_3 has previously been investigated as a high-index material for UV laser coatings in the wavelength regime 248 nm to 355 nm.[17;38;39;40] Sc_2O_3 has been paired with low index materials such as SiO_2 and MgF_2 to demonstrate interference coatings with high damage thresholds in the UV regime.[38;39] Rainer *et al*. found the damage threshold of electron-beam-evaporated Sc_2O_3/SiO_2 and Sc_2O_3/MgF_2 HR and AR coatings to be > 6 J/cm^2 at $\lambda = 248$ nm and for 20-ns pulsewidths.[38] The damage threshold for Sc_2O_3/SiO_2 e-beam-evaporated HR structures was found to be as high as 4.7 J/cm^2 at 355 nm and 0.4 ns by Tamura *et al*.[39] In these reports, however, no consideration is given to the mechanisms that affect the laser damage threshold.

The physical and optical properties of scandia films depend on the growth method. The sol-gel (a process of dip coating from a chemical solution) coatings of Grosso *et al*. had surface root-mean-square (rms) roughness of 1.2 nm as measured via AFM, a UV transmittance cut-off of $\lambda = 215$ nm and low refractive indices at $\lambda = 355$ nm

of 1.62.[17] Al-Kuhaili demonstrated electron-beam evaporated scandia coatings that had density gradients in the thickness of the films.[41] Amorphous films with refractive index near 1.75 at $\lambda = 800$ nm were obtained at low growth temperatures, while crystalline films were obtained, with a higher refractive index of 1.9 at $\lambda = 800$ nm, when deposited with heated substrates. The refractive index of reactive thermally evaporated scandia was reported to be 1.89 at $\lambda = 550$ nm and 1.86 from $\lambda = 900$ to 2000 nm by Heitmann.[42] These reactively evaporated films were also seen to have infrared absorption signatures likely due to water incorporation in the films. Atomic layer deposition was successfully implemented to deposit scandia. These films had a slight excess of oxygen ($Sc_2O_{3.1}$), likely due to hydroxyls in the film, and smooth surfaces with surface rms roughness $\leq$ 3.6 nm.[43] Reactive pulsed laser deposition (PLD; a PVD process where a pulsed laser is used to ablate a target) was used to deposit scandia thin films on GaN with varying substrate temperatures and oxygen partial pressures during film growth.[44] An increase in substrate temperature made the films more crystalline and created smooth films with 0.5 nm rms surface roughness, while increasing the oxygen partial pressure made the surface rougher and less crystalline. MOCVD-deposited Sc_2O_3 films by Xu *et al*. were amorphous when grown on substrates heated to 450 °C and became less optically transmissive, more crystalline and had higher refractive indices (slightly higher than 1.95 at $\lambda = 1$ µm) when the substrate temperature was raised to 600 °C.[40]

The scaling law of Mero *et al*. compared with the table of bandgaps (Table 1.2) suggests that the near-IR, short-pulse (pulsewidths below 10 ps) damage thresholds of Sc_2O_3 should be higher than HfO_2, Ta_2O_5 and TiO_2. The model of Mero *et al*. assumes that breakdown occurs when a critical carrier density is reached in the conduction band. The model is based on a rate equation for the carrier concentration and the loss terms in the rate equation are in the form of native and laser-induced defects in the material. It is through these terms that the structural properties of the material are incorporated.

1.2.2 Motivation for presented work

The variety of film properties, as shown in the previous section, that is obtained by varying the deposition process and conditions within each process shows the necessity to understand how the deposition conditions affect the structural and optical properties of thin-film oxides, on a microscopic level. The motivation of this thesis is to study the impact of the deposition conditions on the structural and optical properties of amorphous scandia films deposited by reactive ion beam sputtering.

Ion beam sputtering produces higher-density amorphous films than any of the deposition methods discussed. Systematic characterization of the structural properties of the films allows for the assessment of the type of defects that play a role in affecting the absorption loss in the films.

Both absorption and damage are defect-driven processes, so an understanding of the nature of the defects and what causes them during growth is necessary. A thorough study of defects present in scandia films, regardless of deposition technique, has not been published. In this thesis, defects are explored through optical absorption, x-ray diffraction, electron paramagnetic resonance and x-ray photoelectron spectroscopy experiments. This work is motivated by the need to engineer optical coatings for high-power infrared lasers.

The ion beam sputtering technique used to prepare the films is discussed in Chapter 2 along with the characterization techniques employed to analyze the films. Chapter 3 presents the details, results and discussion of experiments conducted on a set of scandium oxide thin films grown with different oxygen partial pressures in the deposition chamber. Conclusions and suggestions for future work on this topic are presented in Chapter 4.

Chapter 2

Experimental Techniques and Theory

This chapter presents the experimental techniques used throughout the course of this work. It begins with a discussion of the Spector® ion beam sputtering system donated to Colorado State University by Veeco. This system was used to deposit the thin films that were studied. The thin films were analyzed using a suite of analysis techniques. Each technique will be discussed in terms of the principles of operation and how it was used during the project.

2.1 Spector Dual Ion Beam Sputtering System

2.1.1 General description

The system used to generate the thin films studied in this work is the Veeco Spector® dual ion beam sputtering (DIBS) deposition system.[45] A schematic of the deposition chamber is shown in Figure 2.1.

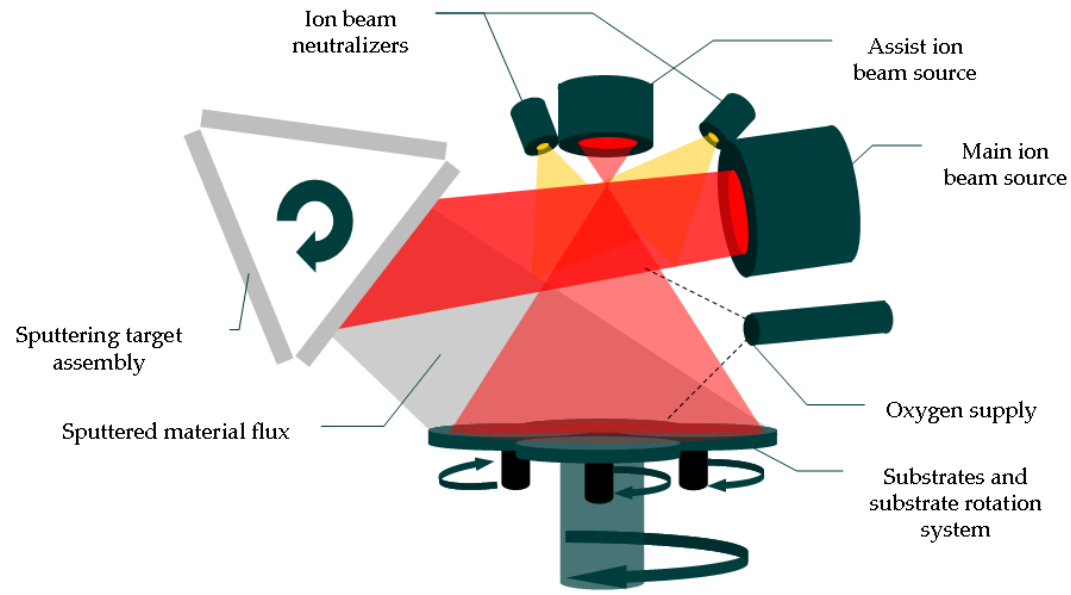

Figure 2.1: Schematic of the thin film deposition chamber showing the sputtering targets, ion beams and sources, ion beam neutralizers, reactive gas inlet and planetary substrate rotation system.

Thin films are generated by sputtering of a solid-state target by an ion beam. The sputtered material forms a flux of gaseous-state particles, which can condense on surfaces in the vacuum chamber including any substrates placed in the chamber. The ion beam sources are radio frequency (RF) ion guns. The main beam is responsible for sputtering the target and generating the vapor-phase material required to form the thin film on the substrate. A second beam, called the assist ion beam, is directed at the substrate surface to influence the depositing film in the same way as the ion beam assisted evaporation process discussed in Section 1.1.4. To maintain charge neutrality in the deposition chamber and to ensure proper operation of the ion beams, RF neutralizers inject electrons into the chamber. Reactive gases can be flowed into the chamber to chemically react with the depositing material and are necessary, in the form of oxygen, when one wants to deposit metal oxides using metal targets. Substrates are moved mechanically throughout the particle flux distribution to generate uniformity in deposited thin films. A shutter, not shown in Figure 2.1, obscures the substrates from the sputtered gas to control when film growth occurs. The sections following this one, 2.1.2 to 2.1.4, will be dedicated to further discussing the ion beam sources, sputtering processes and film growth.

Two substrate rotation fixtures can be used in the Spector and are required to uniformly deposit films from the non-uniform sputtered flux distribution. A simple single-axis rotation system can be used in which the rotation about an axis can be set up to $\sim$ 1000 rotations per minute (rpm). Substrates are placed in a radially symmetric holder that is mounted to a rotation motor. The single-axis rotation fixture requires a shadow mask for uniform deposition. The shadow mask is a stainless steel piece shaped in a specific geometry so that, in a single revolution, the integrated sputtered flux on the substrate is constant over the entire radius from the fixture rotation axis. The second available substrate rotation mechanism, and the system used for most of the work presented here, is a planetary rotation system. As diagrammed in Figure 2.1, substrates are held in rotationally symmetric holders that are analogous to planets in a solar system. There are four of these rotating "planets" affixed to the outside of a larger rotating platform. The rotational periods of the large platform and individual substrate holders are set so that a substrate does not reach the same position in space for many minutes. This pseudo random motion allows for uniform deposition over much larger areas and without shadow masks compared to the single-axis rotation fixture. Both rotation systems have shutters, which totally obscure substrates from any flux of sputtered atoms when closed.

Connected to the deposition chamber is a CTI-Cryogenics On-Board cryogenic pump,[46] or cryopump, that evacuates the deposition chamber to high vacuum. High vacuum must be achieved in the deposition chamber to minimize defect-incorporation in the deposited film, to minimize collisions of the sputtered particles on their way to the substrate and to allow the operation of the ion beams. The cryopump works by trapping gas particles by adsorbing or condensing them on cold surfaces. The pump has two arrays of parallel surfaces: the first is held at 65 K to trap water and hydrocarbon vapors and the second array, which is coated with charcoal granules, is fixed at 15 K and condenses nitrogen, oxygen and argon gases. Closed-cycle refrigeration cools a two-stage cold head, which provides the cooling to the two arrays. High pressure helium, compressed by an external compressor, adiabatically expands and cools the cold

head and returns to the compressor to complete the refrigeration cycle. The cryopump cannot operate at atmospheric pressure; thus, a mechanical roughing pump reduces the vacuum pressure from atmospheric pressure ($\sim$ 700 Torr) to crossover (typically 0.2 Torr), after which, the gate valve to the cryopump from the chamber is opened. The 1-m diameter and 1-m tall vacuum chamber can be pumped to $\approx 9 \times 10^{-8}$ Torr in a 24 hour period. Periodically, condensed species must be purged from the cryopump system in a process called regeneration where the pump is isolated, heated to room temperature to allow condensed species to sublimate, purged with nitrogen gas to dilute the contents, pumped by an external pump to evacuate the contents of the cryopump and cooled back down to operational temperatures. During deposition, the chamber-cryopump gate valve is open, allowing for continuous pumping of the chamber. The chamber pressure is monitored with an ion gauge.

The partial pressure of individual atomic and molecular species is measured with a residual gas analyzer (RGA). The particular RGA system used is an Inficon Transpector2 Gas Analysis System. The RGA identifies particles by their charge to mass ratio. The Transpector2 sensor is composed of an ionizer, a quadrupole mass filter and an ion detector.[47] Gases from the deposition chamber are introduced into the ionizer. The ionizer consists of a filament, which is heated to thermionically emit electrons. The electrons are accelerated through an electrostatic potential from the filament (cathode) to a positively biased metal mesh (anode) that allows gas species to flow into the region where the electrons are accelerated. The fast-moving electrons ionize atoms and molecules through electron impact ionization processes, leaving the atoms and molecules charged such that they are accelerated from the ionizer region by a negatively biased (relative to the anode mesh) focusing lens. The focusing lens is an electrode with a hole in the center that allows for passage of the ions into the quadrupole mass filter.

The quadrupole mass filter consists of a four parallel rods arranged in a square array. Rods opposite of each other in the array are electrically connected. The voltage applied to the first pair is $V_1 = V_{\mathrm{RF}} \cos(\omega t) + V_{\mathrm{DC}} + V_0$ and the voltage applied to

the second pair of poles is $V_2 = V_{\mathrm{RF}} \cos(\omega t + \pi) - V_{\mathrm{DC}} + V_0$ and is 180° out of phase from the first pair and reversed biased. V_{RF} is the peak-to-peak RF voltage amplitude, $\omega/(2\pi)$ is the RF frequency, V_{DC} is the DC bias and V_0 is a reference or "center" voltage. A narrow range of mass/charge is passed by the quadrupole filter. The minimum mass/charge ratio allowed to pass through the filter is determined by ω and V_{RF} as low-mass/charge species move in phase with the RF electric field and become neutralized by colliding with the poles. The DC potential governs the upper limit as heavier (larger mass/charge ratio) ions are deflected enough by the DC potential to collide with the poles.

Ions passing through the quadrupole filter are measured by a Faraday cup. A Faraday cup is an electrode onto which ions impinge and are neutralized by electrons in the electrode. The flow of neutralizing electrons to the electrode is an electrical current and is detected in a circuit and is generally equal to the incident ion current. An electron multiplier can be used to enhance the sensitivity by accelerating ions to a surface that emits secondary electrons after impact. A series of surfaces afterwards can be used to amplify electron emission so that for every incident ion, many electrons are generated. These electrons are then measured by a Faraday cup. The electron multiplier enhances sensitivity by many orders of magnitude but the electron gain can be unstable, yielding variable quantitative results. The current, for a given atomic mass, measured by the Faraday cup is equal to the partial pressure of that atomic mass through a proportionality constant that depends on the nature of the analyzer and measured substance. The computer software used to control the RGA and extract data, computes the partial pressure of the substance from the measured current.

The RGA was mainly used to measure gas that was flowed into the chamber during deposition (argon and oxygen). The partial pressure measurement of the RGA was calibrated with an ion gauge for argon and oxygen, respectively, by flowing one of the gases into the chamber at a time and simultaneously measuring the partial pressure of the gas specie with the RGA and the total chamber pressure with the ion gauge. The partial pressure of the gas species was approximately the total pressure in the cham-

ber as other species (background pressure) were present at partial pressures at least $\sim$ 100 times less than that of the gas flowed into the chamber. A sample calibration curve for molecular oxygen is given in Figure 2.2.

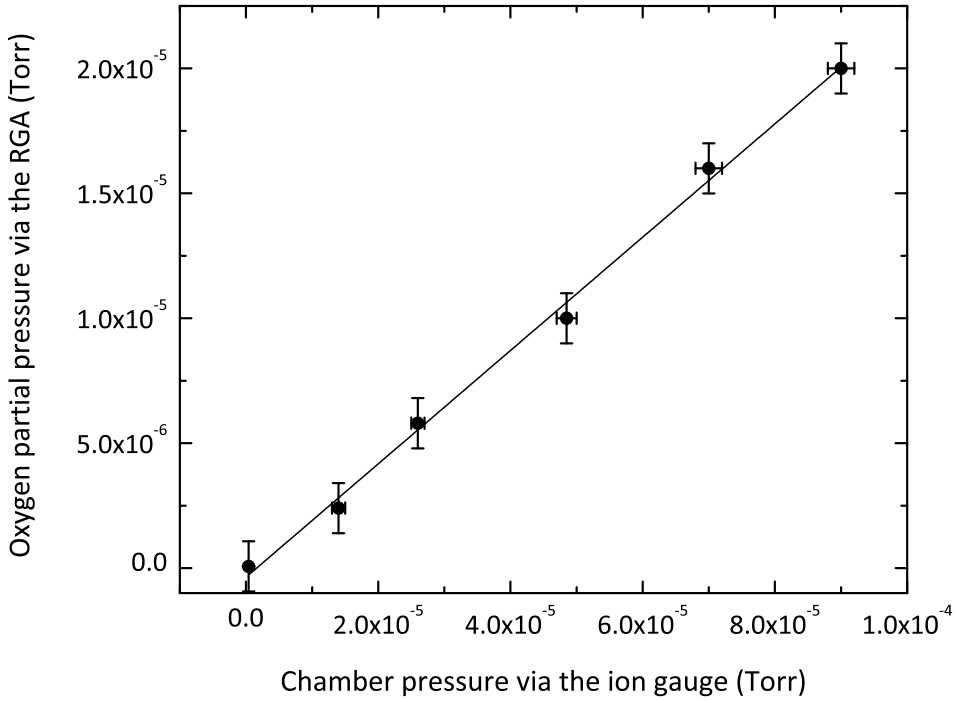

Figure 2.2: Curve used to calibrate the partial pressure of molecular oxygen in the Spector vacuum chamber measured by the RGA with an ion gauge. A linear fit is included with the data.

Since no ionizing source was present to generate atomic oxygen from the flowed molecular oxygen, the partial pressure measured at 16 amu was assumed to be an artifact of the RGA measurement; therefore, the partial pressures of 16 and 32 amu were summed in recording the partial pressure of molecular oxygen in the deposition chamber.

Oxygen gas is flowed into the deposition chamber during film growth to form metal oxide films when a metal target is used. Attached to the gas inlet is an Advanced Energy (AE) inductively coupled plasma (ICP) source, a schematic of which is shown in Figure 2.3.

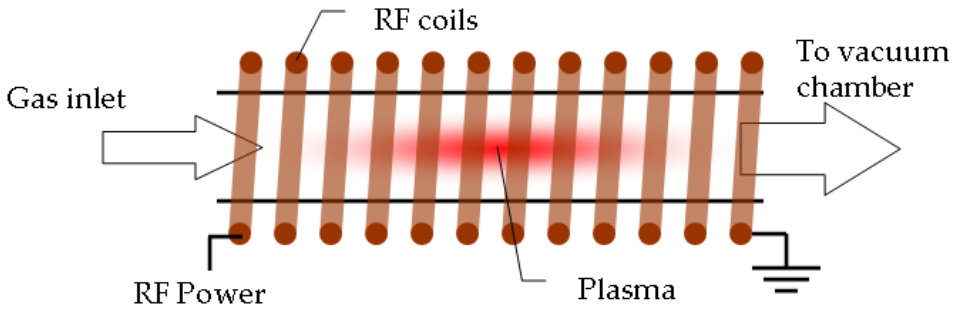

Figure 2.3: Schematic of the AE ICP reactive gas source.[48]

The ICP source generates a plasma by inductively coupling radio frequency (RF) electrical power into the reactive gas as it flows through the source. This is the same method in which the plasma is generated in the ion beam sources and will be discussed further in Section 2.1.2. Theoretically, the ICP source can dissociate molecular gases and generate excited species, which flow into the deposition chamber, and may provide the possible benefits of higher deposition rates and improved film stoichiometry due the increased reactivity of the injected species.[48] Though the ICP might generate excited and atomic gas species, we have found minimal to no enhancement in the deposition rates and film properties when using the ICP source. No increase was measured in the partial pressure of atomic oxygen (16 amu) when the ICP source was turned on compared to it being off when oxygen was flowed into the deposition chamber.

The deposition process is monitored and controlled through computer software and all gas flows are controlled with gas flow controllers. A coating is made through a set of programs called recipes. A typical recipe is outlined below with typical values enclosed in parenthesis. A table summarizing typical gas flows and ion beam source parameters used is shown in Table 2.1.[45;49]

1. The substrate fixture rotation is turned on, the fixture shutter is closed and the chamber is pumped to 5×10^{-5} Torr

2. The substrate fixture shutter is opened, quartz heaters are turned on and the chamber is baked at 150°C to increase the rate of water desorption from the substrate and chamber surfaces

3. The chamber is cooled to 100°C and maintained at that temperature for the rest of the deposition process

4. The substrate fixture shutter is closed and the chamber is pumped until the desired base pressure is reached (7×10^{-7} Torr)

5. Main (argon) and assist (oxygen) ion source, associated neutralizer (argon) and reactive target (oxygen) gases are turned on to stabilize flows (see Table 2.1)

6. The main and assist ion sources are turned on, after RFN electron emission is established, so that the plasma discharges are created and allowed to stabilize

7. The assist ion beam, source and oxygen flow are all turned off and the argon flow to the assist source is turned on and stabilized

8. The assist ion source argon plasma is created, following RFN emission, and stabilized

9. With the fixture shutter still closed, the desired target is set, target oscillation is begun and the main ion beam is turned on to sputter clean the target before film deposition (the same parameters are used as for film deposition)

10. The reactive gas flow is set to the desired value, the fixture shutter is opened and the main and assist ion beams are turned on–beginning film deposition–[the delay is specified for the desired thickness based on previous calibrations]

11. Both ion beams are turned off

12. If multilayers are being deposited, the deposition steps (steps 10 and 11) are repeated for another material until the number of desired layers have been deposited

13. The RFN gas flows are turned off

14. When the chamber temperature ≤ 35°C, the chamber can be vented and coatings can be extracted

System component	Parameter	Value
Main sputtering beam	Beam current	300 to 600 mA
	Beam voltage, V_B	1250 V
	Accelerator voltage, V_a	150 V
	Argon gas flow	14 to 35 sccm
Assist ion beam	Beam current	50 to 200 mA
	Beam voltage, V_B	0 to 300 V
	Accelerator voltage, V_a	500 to 600 V
	Argon gas flow	10 to 15 sccm
RFNs	Argon gas flow	4 to 7 sccm
Reactive gas inlet	Oxygen flow	0 to 49 sccm

Table 2.1: Summary of typical ion beam source and gas flow parameters used for the work presented in this thesis.

2.1.2 Ion beam sources

As was shown in Figure 2.1, the Spector employs two similar ion beam sources: the 16-cm diameter main ion beam responsible for target sputtering and the 12-cm diameter assist ion beam directed at the substrate to enhance film growth. Each ion source has a corresponding neutralizer. A schematic of a RF ion source plus RF neutralizer (RFN) is given in Figure 2.4.

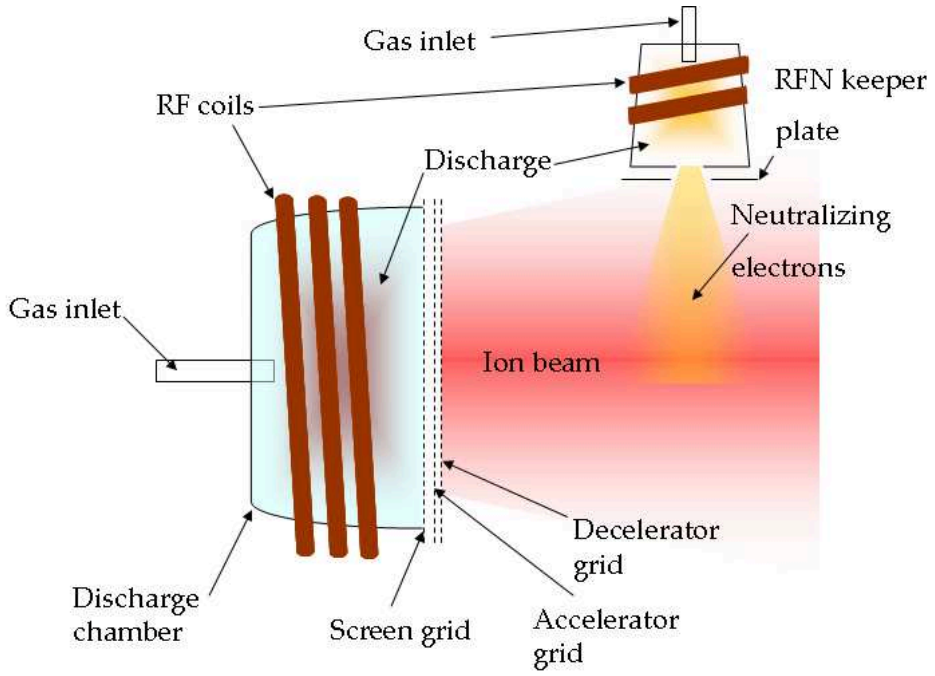

(a)

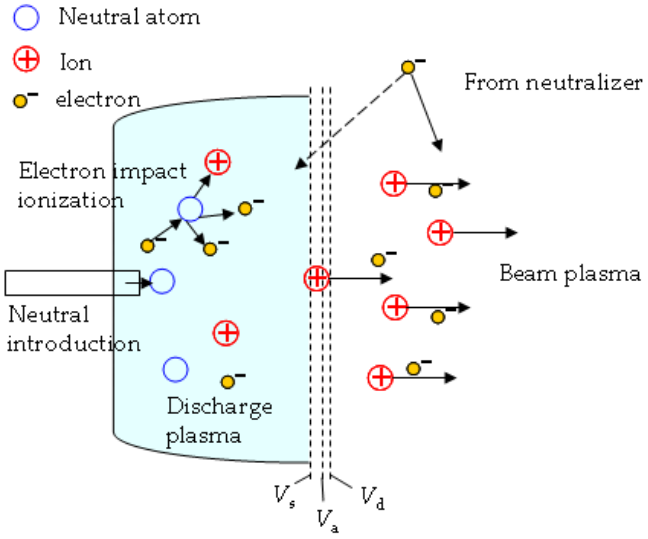

(b)

Figure 2.4: Schematic of the ion sources used in the Spector. The main components are shown in (a). In (b), the source and beam plasmas are diagrammed.

The main components are shown in Figure 2.4(a). Through an inlet, gas is fed into a quartz bowl, which is encircled by an RF antenna. Power from the antenna is coupled into the quartz bowl to create a plasma containing ions of the introduced gas species. At the opening of the bowl are three parallel molybdenum or pyrolytic graphite grids through which ions are extracted to form a beam. The RFN also includes a gas inlet

fed into a hollow chamber encircled by an RF antenna, which generates a plasma in the RFN chamber. At the open end of the RFN is a keeper plate, which is responsible for electron extraction from the RFN.[45]

The operation of the ion beam source is diagrammed in Figure 2.4(b). Neutral atoms are introduced, as a gas, through the inlet into the ceramic discharge bowl. A plasma discharge is created from the gas when RF electrical power (at 13.56 MHz, which is standardized by international communication authorities)[32] is inductively coupled to the discharge chamber via a water cooled antenna (RF coil). A transformer can be used to model the source with the RF coils as the primary coil and the plasma discharge as the single-turn secondary coil.[48] A variable complex impedance matching network is needed to minimize the reflected electrical power delivered to the variable-impedance source. The discharge is initiated using electrons reaching the discharge chamber from the RFN. Due to the Lorentz force, electrons with velocity components orthogonal to the RF solenoid antenna axis undergo cyclotron motion as the magnetic field generated by the RF current in the antenna oscillates. The electrons with enough energy (energy greater than the ionization energy) can ionize neutral atoms through electron impact ionization. The high-energy electron collides with a neutral atom and, with some probability, ionizes the atom resulting in the colliding electron with less energy, an emitted electron and an ion. Electrons from the neutralizer are needed to initiate the ionization reactions but after some time, enough electron-ion pairs are generated for the reaction to be self sustaining until the plasma reaches its steady-state. One characteristic of plasmas is that they are a quasineutral gas of mobile charged and neutral particles with the characteristic dimension of the plasma (called the Debye length) much less than the size of the system.[50] The quasineutrality condition implies that $n_{\mathrm{i}} \approx n_{\mathrm{e}}$ inside the discharge chamber, where n_{i} is the volume density of the positively charged ions and n_{e} is the volume density of the negatively charged electrons, either of which can be referred to as the plasma density. The Debye length is

$$\lambda_D \equiv \left(\frac{\epsilon_0 k T_e}{n_e e^2} \right)^{1/2}, \tag{2.1}$$

where ϵ_0 is the permittivity of free space, k is Boltzmann's constant and T_e is the temperature of the electrons, and e is the electronic charge. Outside the Debye length, Coulombic forces are screened.

Extraction of the discharge plasma ions is accomplished by a parallel perforated grid system containing three biased grids called the screen, accelerator and decelerator grid, as shown in Figure 2.4(a). Holes in the grids are precisely aligned such that each set of holes generates an ion beamlet that passes through the holes without colliding with and sputtering the grid webbing. Because the electrons are much lighter than the ions, they initially collide with and coat discharge chamber surfaces at a higher rate resulting, at steady-state, in a discharge plasma potential that is $V_{dp} \approx 25$ V above the most positive discharge chamber surface (the screen grid).[45] A plot of the extraction grid potentials is given in Figure 2.5.

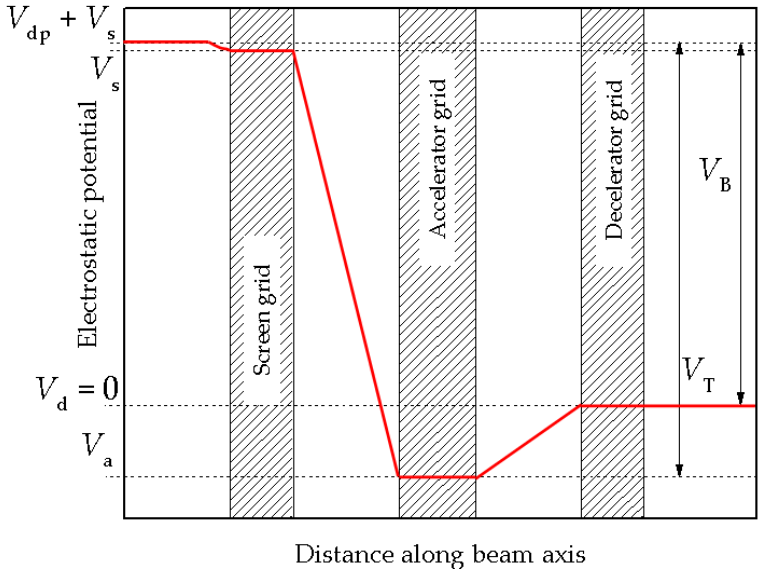

Figure 2.5: The electrostatic grid potential energy, through the grids, plotted along the beam axis. Adapted from Franz.[51]

Positive ions in the discharge chamber might reach the screen grid, which is biased to voltage V_s, and gain kinetic energy as the potential drops V_{dp} across the plasma sheath. The ion is then accelerated from the screen grid to the accelerator grid, which is

biased at V_a and is usually negative of system ground. The negative voltage prevents neutralizer electrons from backstreaming into the discharge chamber during beam operation, which would result in a false beam current, and also allows for greater beam currents as the maximum allowable beam current that can be extracted is

$$I_{max} \approx \sqrt{\frac{e}{m_i}} \frac{4\epsilon_0 A_b V_T^{3/2}}{9 l_g^2}, \tag{2.2}$$

where A_b is the effective area of the beam (the grid area multiplied by the open-hole fraction), m_i is the ion mass, l_g is the spacing between the screen and accelerator grids and the total voltage is given by $V_T = V_B + |V_a|$, where V_B is called the beam voltage.[52] The operational beam current is determined by the RF power coupled to the discharge chamber as the plasma density increases proportionately with RF power to the discharge and the extracted beam current density is nearly proportional to the discharge chamber plasma density.[45] In normal operation, the desired beam current is set and the RF power delivered to the discharge is automatically adjusted to maintain the desired beam current. With ion beams operating, typical RF powers delivered to the 16- and 12-cm sources are $\simeq 400$ and $\simeq 250$ W, respectively.

The final grid is called the decelerator grid and is held at a potential $V_d = 0$. It provides for a defined ground-potential ion beam, that helps reduce beam divergence, and obstructs the accelerator grid from being coated by the sputtering process, which might cause grid-arcing.[51;53] Ions in the beam reach ground potential at the decelerator grid such that the kinetic energy of the beam ions when they reach the sputtering target is $eV_B = e(V_{dp} + V_s)$, where e is the fundamental charge.

Operation of the ion beams requires neutralization of ion current, volumetric space charge and surface charge. Without neutralization, the Coulombic repulsion of the ions would cause the beam to diverge.[51] The beam is neutralized not by recombination of the ions with electrons but by uniform distribution of electrons within the beam to form a beam plasma with $n_i \approx n_e$. Deposition chamber surfaces are neutralized when the positive ion current and negative electron current, reaching the surfaces, are equal. The electron current emission set at 150% of the corresponding ion current

emission during beam operation to ensure enough electrons were available for neutralization.[45] Prior to beam extraction with the application of V_a, free electrons from the neutralizer are used to ignite the discharge plasma. The operation of a RFN is similar to that of the ion source (see Figure 2.4(a)); 13.56 MHz power is inductively coupled to a gas, which has been fed into a hollow ceramic chamber. Once a plasma has been initiated within the RFN, electrons are accelerated out of the chamber when the keeper plate is biased positive of the electrically grounded metal shroud surrounding the ceramic discharge chamber. The keeper-sustained plasma allows electrons to easily flow between the remotely located RFNs and the beam plasmas.

A table of deposition parameters typically used is given in Table 2.1. The main 16-cm source grids were manufactured to operate at $V_B = 1.25$ kV. The assist beam voltage was kept at a relatively low voltage to not sputter and roughen the substrate in the cleaning process. In deposition mode, a non-reactive gas (argon) was chosen and the energy of the beam was varied to study the resulting film properties. The beam currents were chosen, within the presented range, to achieve a certain ion flux. The accelerator voltages were then chosen to minimize the damaging ion current flowing to the accelerator grid measured as the accelerator current. Ion source gas flows were selected such that stable operation of the ion sources was achieved. The reactive gas flows were varied as discussed in the following sections.

2.1.3 Target sputtering

Sputtering is defined as the removal of atoms from a solid-state surface due to energetic particle bombardment.[52] When energetic ions collide with the target surface, backscattered ions, sputtered target atoms and clusters, secondary and Auger electrons and light and x-rays can all be emitted from the target surface.[54] A schematic of the cascading sputtering process is given in Figure 2.6.

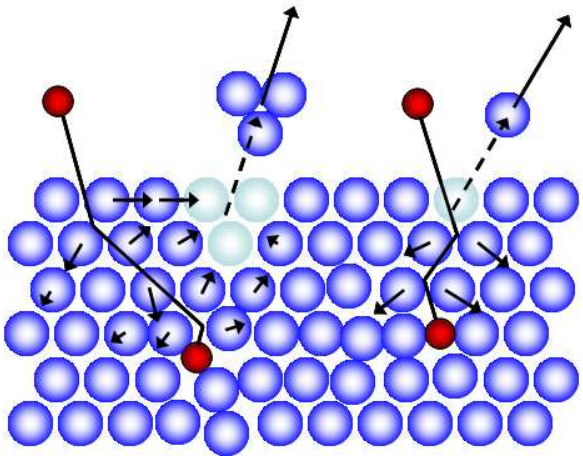

Figure 2.6: Schematic of the collision cascade sputtering process. Adapted from Pivin.[54]

The incoming ion can be backscattered or implanted in the target at some depth, dependent on its energy and collisions. Target atoms are displaced from their equilibrium with some coming to rest in the target matrix and some, if at or near the surface, being liberated from the target surface.[54]

The number of sputtered atoms emitted on average from the target surface per incident ion is called the sputter yield Y. Generally, the sputter yield is dependent on the mass of the sputtering ion and the target element being sputtered, the energy and angle of the incident ions relative to the target surface and the composition of the target, including crystallinity.[52]

The sputtered atoms and molecules have a wide energy and angular distribution. Typically, the most probable direction for sputtered particle emission is the "specular" direction relative to the beam (i. e. the angle between the beam and target surface normal equals the angle between the most probable emission direction and the surface normal). Generally, the angular distribution is widely spread about the specular direction but can be more or less peaked along the specular direction. The kinetic energy of sputtered atoms follows a Thompson distribution. As an example, sputtered Ti atoms (from a Ti target) can have speeds $\sim 10^3$ to $\sim 10^4$ m/s for a 1-keV Ar ion beam. Also, oxidation of the target surface by reactive gases can change the distribution of energy of sputtered atoms.[52] The process of target oxidation and its effect on the sputtering process will now be considered further.

During the reactive sputtering process, the surface of a metal target reacts with the reactive gas forming a compound at the surface. The reaction of an unbonded metal surface atom, M, with vapor-phase oxygen molecules to form a surface compound, M_mO_n, can be expressed as

$$M + \frac{n}{2m}O_2 \xrightarrow{k_1(T)} \frac{1}{m}M_mO_n\,, \tag{2.3}$$

where $k_1(T)$ is a temperature-dependent reaction rate constant.[55] Similarly, the reaction with oxygen atoms is

$$M + \frac{n}{m}O \xrightarrow{k_2(T)} \frac{1}{m}M_mO_n\,. \tag{2.4}$$

Oxide compound formation on the metal target surface begins with adsorption of molecular or atomic oxygen in a physisorption (discussed in the following section on film growth) process. Molecular oxygen is dissociated thermally at the surface and then n oxygen atoms chemically bond to m surface metal atoms forming the oxide compound M_mO_n.[55] The equilibrium target compound surface coverage, or the fraction of available compound-forming sites containing the compound on the target, is

$$\theta_t = \frac{k_t \vartheta_t^{n/2m}}{k_t \vartheta_t^{n/2m} + Y_c J/e}\,, \tag{2.5}$$

where k_t is the temperature-dependent compound-forming rate constant (Equations (2.3) and (2.4)), J is the ion beam current density, e is the fundamental charge, Y_c is the effective sputtering yield of the compound and ϑ_t is the steady-state adsorption coverage of the target, which is similarly defined as the compound surface coverage except for adsorption instead of chemical bonding.[55] The steady-state adsorption coverage is given by

$$\vartheta_t = \frac{K_t p_0}{1 + K_t p_0}\,, \tag{2.6}$$

where p_0 is the partial pressure of oxygen in the deposition chamber and K_t is the adsorption rate constant, which depends on the temperature of the surface adsor-

bant and the gas. When the adsorption is isothermal, Equation 2.6 is the Langmuir isotherm and K_t represents the equilibrium isothermal adsorption rate constant.[26]

The surface compound coverage θ_t is a result of the competing processes of oxygen adsorption leading to compound formation and compound removal through the sputtering process. Both Equations (2.5) and (2.6) assume that once a site has been occupied, it is no longer accessible to compound formation or adsorption, respectively. Equations (2.5) and (2.6) can be used to determine the total sputtering rate of metal atoms, including metal atoms bonded in the compound M_mO_n, as

$$R_m = \frac{JA_t}{e}\left[Y_m\left(1-\theta_t\right) + mY_c\theta_t\right], \tag{2.7}$$

where Y_m is the sputter yield of the unoxidized metal and A_t is the sputtered area of the target.[56] A plot of $R_m(p_0)$ and $\theta_t(p_0)$ is given in Figure 2.7.

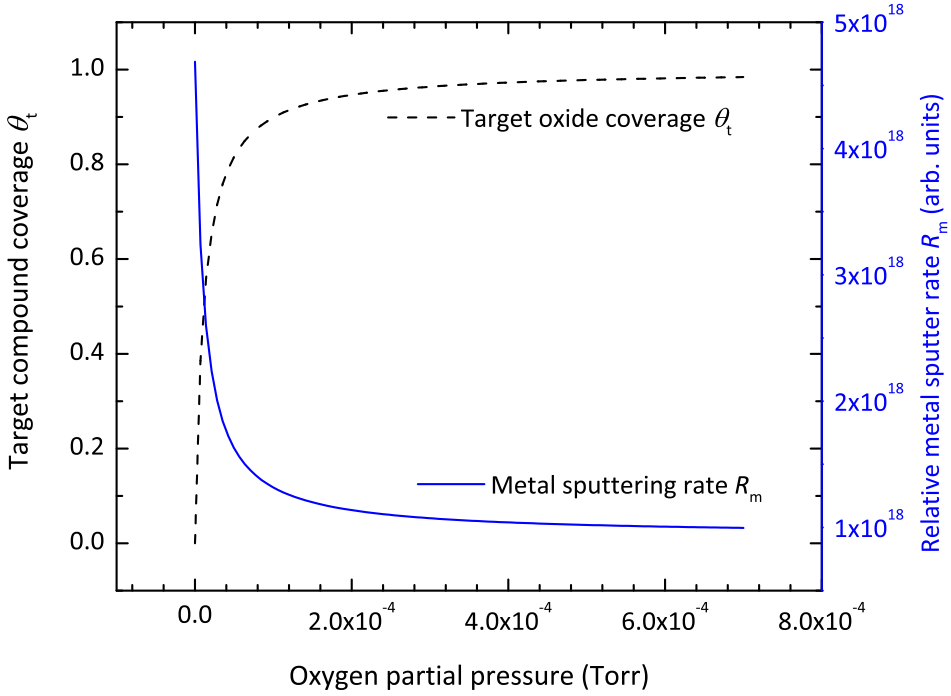

Figure 2.7: Target oxide compound surface coverage θ_t and metal sputtering rate R_m as functions of oxygen partial pressure p_0 for the values and isothermal expression for θ_t given by Berg and Nyberg.[56]

The parameters used for the determination of $\theta_t(p_0)$ and $R_m(p_0)$ are taken from Berg and Nyberg, as well as the isothermal expression for θ_t.[56] Figure 2.7 shows that as $p_0 \to \infty$, the target surface coverage saturates at 1 and the removal rate of metal atoms

saturates at some value less than $R_m(p_0, \theta_t = 0)$.

2.1.4 Film growth

Film deposition

As discussed in Section 1.1.4, there are two general classifications of thin film deposition techniques. Reactive ion beam sputtering is a combination of physical vapor deposition, from the kinetic sputtering process creating vapor-phase species, and chemical vapor deposition as the reactive gas combines with vapor-phase atoms condensing on a surface to form a chemical compound. The condensation process is a heterogeneous process with condensing adatoms of a different phase than the substrate. The process begins with adatoms adsorbing on the surface with two adsorption modes: physisorption and chemisorption. Physisorption is due to van der Waals or dispersion forces with bond strengths usually less than 0.2 eV, while chemisorption involves chemical bonding and typical bond strengths between 3 to 5 eV.[26] Chemical compound formation occurs after adatoms have physisorbed and diffused on the surface to react.[26;55] Following adsorption, nucleation of the film occurs, then the nuclei grow into islands as more adatoms adsorb on the surface, the islands grow into each other, forming a continuous network, and then thickness is added to the film.[57]

The nucleation process occurs in three different regimes called Frank-Van der Merwe, Volmer-Weber and Stranski-Krastanov modes.[57;58] In the Frank-Van der Merwe growth mode, single layers of atoms (monolayers) are deposited a layer at a time with no new monolayers added until the depositing monolayer has complete surface coverage. Volmer-Weber growth proceeds with formations of individual three-dimensional islands and occurs when the interaction between adatoms is greater than the adatom-substrate interaction. The Stranski-Krastanov mode combines the other two modes; the growth is layer-by-layer for the first few monolayers, followed by individual island growth.

The structure of the growing film depends on shadowing (geometric obstruction of available surface sites by previously adsorbed species), surface diffusion (mobility of

adsorbed species on the surface and interfaces typicslly dominated by high substrate temperatures T_s), bulk diffusion (the mobility of atoms or molecules in the bulk of the films dominated by T_s) and by crystallization (change of crystallinity) dominant at high T_s and large film thicknesses.[57] The structure of a film can be modeled using structure zone models. The simplest structure zone model consists of 3 zones in terms of the ratio of substrate to film melting temperature T_s/T_m: 1) $T_s/T_m < 0.3$ characterized by low adatom mobility resulting in a porous and fine-grained structure, 2) $0.3 < T_s/T_m < 0.5$ with surface diffusion resulting in a columnar structure in the film and 3) $T_s/T_m > 0.5$ characterized by bulk diffusion of atoms and a rough, equiaxed crystallite structure.[57]

The addition of ion bombardment to the depositing film, through an assist ion beam, can reduce defect formation in the film by keeping the substrate relatively cool while adding energy to the surface.[59] Some of the structural properties modified by low-energy ion bombardment are grain size, film density, columnar orientation and film stress. Though our group has studied the effects of the assist beam on film properties,[60] the effects of assist-bombardment are complex and beyond the scope of this work.

The metal oxide films that we have deposited and that are presented in the following chapter are amorphous in nature with crystalline grains with lengths $\sim$ 10 nm. Amorphous films are created when the atoms are cooled rapidly, in going from the vapor phase to the adsorbed state, such that complete crystallization does not occur.[19]

Reactive sputtering

The chemical kinetics of reactive sputtered film growth is similar to that of oxide formation on the sputtering target surface with the exception that compound formation requires the adsorption of both metal and oxygen species to form the desired compound M_mO_n. As discussed in the previous section on target sputtering, reactive gases in the sputtering chamber form compounds on the surface of the target as well

as at the film collection area. The collection area (substrate and chamber wall) receive adsorbed metal and metal oxide compound species sputtered from the target and adsorbed reactive oxygen from the chamber. The mass balance equation for the oxygen flow (basic units of volume per time) is

$$Q_0 = Q_\mathrm{t} + Q_\mathrm{s} + Q_\mathrm{w} + Q_\mathrm{p}, \tag{2.8}$$

where Q_0 is the gas flow into the chamber and $Q_{\mathrm{t,s,w}}$ are the oxygen flows to available (metal) sites on the surface of the target, substrate and wall, respectively, and Q_p is the flow of oxygen to the vacuum pump.[55] If the oxygen in the chamber has a partial pressure p, mass $m = 16$ or 32 amu (for atomic and molecular oxygen, respectively) and temperature T, then the flow of oxygen to the substrate is

$$Q_\mathrm{s} = \frac{\alpha p(1-\theta_\mathrm{s})A_\mathrm{s}}{\sqrt{2\pi k_\mathrm{B} T m}}, \tag{2.9}$$

where k_B is Boltzmann's constant, α is the effective sticking coefficient of the oxygen, A_s is the effective substrate area and θ_s is the fraction of the substrate covered with the compound $\mathrm{M}_m\mathrm{O}_n$.[56] Berg's model predicts the surface coverage of the compound at the substrate to saturate at 1 as the partial pressure of oxygen is increased in the chamber as shown in Figure 2.8.

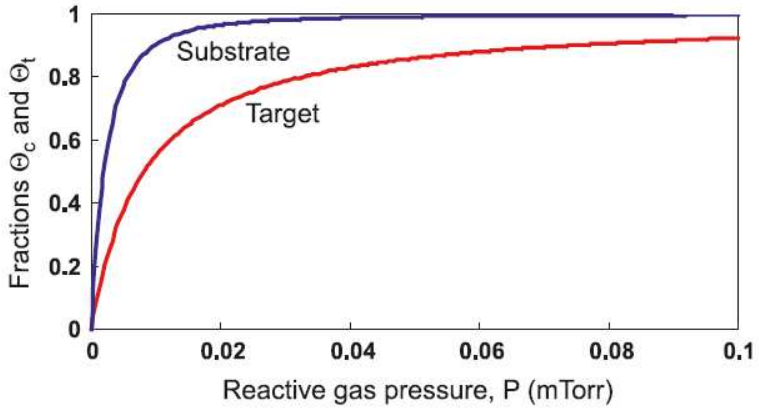

Figure 2.8: Target oxide compound surface coverage θ_t and substrate metal oxide coverage (labeled θ_c) as functions of oxygen partial pressure predicted by Berg's model. Taken from Berg and Nyberg.[56]

The deposition rate, as seen with the sputtering rate from the target in Figure 2.7,

decreases with oxygen partial pressure (shown in Figure 2.9).

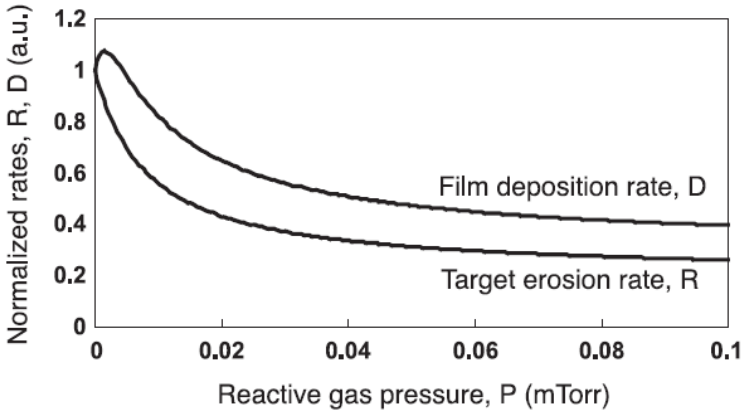

Figure 2.9: Normalized film deposition rate and rate of sputter from the metal target in reactive sputtering predicted by Berg's model. Taken from Berg and Nyberg.[56]

Defect growth

As discussed in Section 1.1.3, defects such as substitutions, vacancies, interstitials and astoichiometry exist in thin films. The vacancies in reactively sputtered metal oxides are likely oxygen vacancies. These might occur when the net adsorption rate of metal exceeds that of the oxygen according to the stoichiometric ratio m/n. The metal adatoms do not necessarily require specific adsorption sites, like the oxygen, such that oxygen adsorption is not likely to exceed metal adsorption. Vacancies can also occur when an assist beam is used because of preferential sputtering of one element over another. Oxygen is lighter than the metals typically used in metal oxide films and often has a higher sputtering yield.

Impurities from the background pressure, especially H_2O and hydrocarbons,[57] can adsorb onto the film and become incorporated as substitutions and interstitials. The deposition rate of the ith gas on the film surface is

$$F_i = \frac{p_i}{\sqrt{2\pi m_i k_B T_i}}, \text{ [57]} \tag{2.10}$$

suggesting defect incorporation from the remaining base pressure is linear with partial pressure of each contaminant.

Up to this point, it is apparent that the deposition process requires a maximum of

oxygen flow to avoid oxygen vacancies and astoichiometry in the deposited film. As the data presented in the next chapter suggest, however, it is also possible to obtain excess oxygen, likely in the form of interstitials, in the films at higher oxygen flows. As will be discussed in Section 3.2, it is possible that at higher-than-necessary oxygen flows, the oxygen sputtered from the target can be trapped in the film. A summary of the properties of reactively sputtered films is given in Figure 2.10, which is from Schiller *et al.*[61] published in Reference 32.

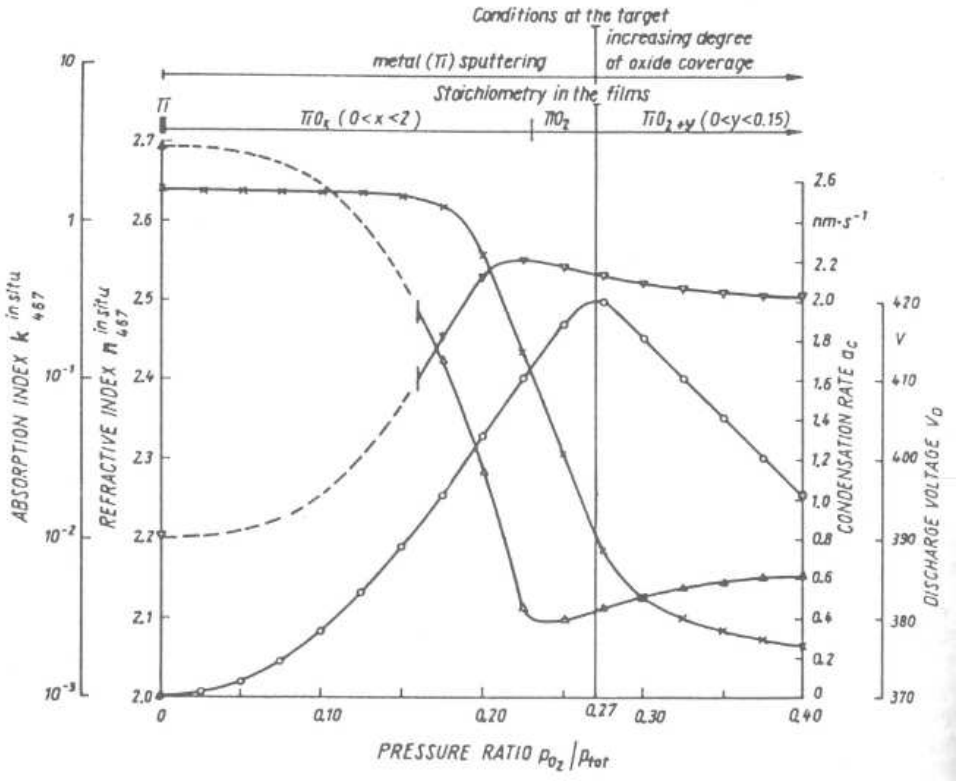

Figure 2.10: Stoichiometry, target condition, κ (absorption index here) ($\triangle$), deposition (condensation) rate ($\times$), refractive index ($\triangledown$) and discharge voltage ($\circ$) as a function of oxygen partial pressure (p_{O_2}/p_{tot}) for TiO_x deposition using reactive DC magnetron sputtering as reported by Schiller *et al.*[61] and published in Reference 32.

As the oxygen partial pressure increased during the deposition process, the sputtering target becam more oxidized and the deposition rate reduced. This was seen to cause the absorption in the reactive magnetron sputtered films to increase for increasing oxygen partial pressure and was correlated with an excessive oxygen stoichiometry (TiO_x where $x > 2$). A similar behavior is seen in scandia as discussed in Chapter 3.

2.2 Thin Film Analysis Techniques

This section briefly covers some of the thin film analysis techniques used to characterize scandia films. Other techniques used include atomic force microscopy (AFM), which was used to investigate the surface roughness of deposited thin films on the sub-nanometer scale; Fourier transform infrared (FTIR) spectroscopy, which was used to detect chemical bonds through absorption of infrared light via bond vibrations; and x-ray photoelectron spectroscopy (XPS), which used the electrons emitted from chemical species after x-ray bombardment to identify elements and chemical bonds. The first set of characterization techniques presented below address the optical properties of thin films and are UV/Vis spectrophotometry, variable angle spectroscopic ellipsometry and photothermal common-path interferometry. The second set of techniques presented are electron paramagnetic resonance spectroscopy and x-ray diffraction, which characterize the physical properties of thin-film materials.

2.2.1 UV/Vis spectrophotometry

A spectrophotometer is a relatively simple instrument, as diagrammed in Figure 2.11, that measures the transmittance T of a sample placed in the chamber. The transmittance is defined as $T \equiv I_t/I_0$, where I_t is the intensity of the transmitted beam and I_0 is the intensity of the beam incident on the sample. The incident intensity is measured as a "baseline," which is taken without a sample in the path of the beam. The intensity spectrum measured with the sample in the path of the beam is divided by the baseline to determine the transmittance of the sample. The spectrophotometer used in his project is a Hitachi U-2010 UV/Vis Spectrophotometer, which is capable of measurements in the UV down to $\lambda = 190$ nm and in the near infrared to $\lambda = 1.1$ µm.[62] The instrument uses two lamps: Deuterium for the UV region and tungsten iodide for the visible to near IR. Wavelengths are selected (± 3 nm) using a rotating diffraction grating and a slit of variable width. Light emitted from the slit passes through the sample chamber and is collected with a Si photodiode.

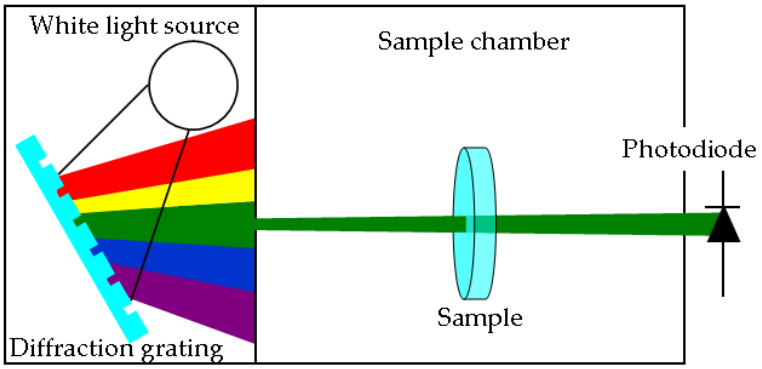

Figure 2.11: Schematic of a spectrophotometer.

Spectrophotometer measurements are useful for ensuring that a coating transmittance matches the design. For the work presented in this thesis, spectrophotometry spectra were used to measure the absorptance of single layers at wavelengths near the band cutoff (λs that are near the wavelength corresponding to the material bandgap energy). Also, the transmittance of a sample was used with ellipsometry measurements (discussed in Section 2.2.3) to determine the optical constants and thickness of single layers. Figure 2.12 gives the transmission spectra measured for an uncoated fused silica substrate and an approximately 200-nm thick single layer of Sc_2O_3 deposited on fused silica.

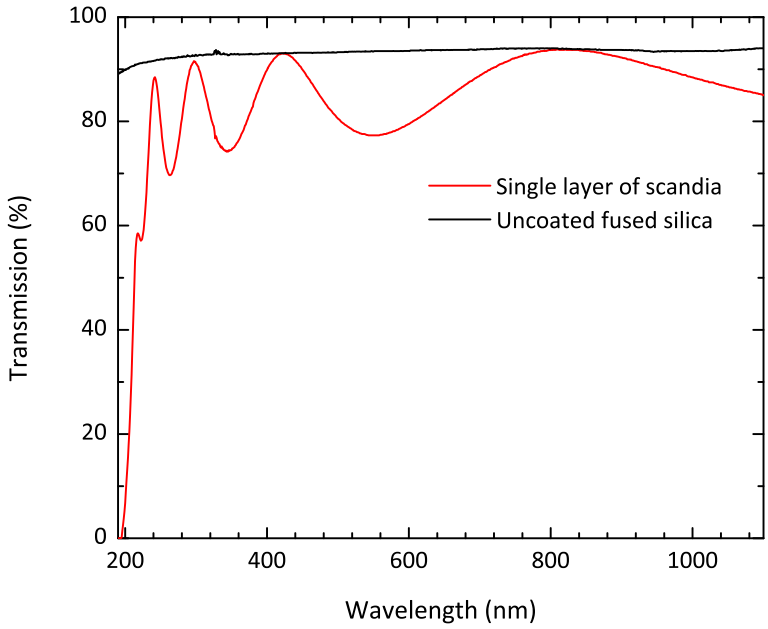

Figure 2.12: UV/Vis spectrophotometry measurements of uncoated fused silica and approximately 200-nm thick scandia on a fused silica substrate. The sharp roll-off observed for the scandia film corresponds with the band edge of the film.

2.2.2 Photothermal commonpath interferometry (PCI)

The optical absorption in the thin films we deposit is measured using the photothermal common-path interferometry technique.[63;15] A schematic of the setup is shown in Figure 2.13.

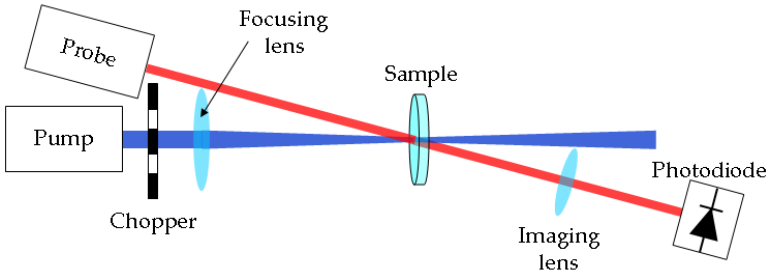

Figure 2.13: Illustration of the PCI setup showing the crossed pump and probe beams.

The technique can measure the absorption (P_a/P_i, where P_a is the absorbed optical power and P_i is the incident power) as low as 1 ppm (1×10^{-6}) in thin films. The technique is a pump-probe technique in which a pump beam is focused into a material with a focusing lens, resulting in heating of the material. The heating causes a local change in the refractive index of the material, resulting in a small lens-like per-

turbation in the material. A second probe beam, with a waist larger than and power less than the heating probe beam, passes through the material. Most of the probe beam passes through unperturbed, but a small fraction of the probe diffracts off of the lenslet and interferes with the unperturbed part of the probe. The interference causes modulation in the time-averaged intensity along the propagation axis of the probe beam. The modulation depth (proportional to the difference between the maximum and minimum in intensity) is proportional to the magnitude of the surface perturbation, which is proportional to the absorbed optical power. The maximum signal occurs at a point in space near to the material perturbation, so to actually record this signal, this point must be imaged. The simplest imaging setup–an imaging lens–is shown in Figure 2.13. The pump is chopped at a few hundred Hertz so that the small signal may be detected with a lock-in amplifier and is focused with a lens.

The pump laser operates at a wavelength of interest for material study. The pump power is limited to power below that which corresponds with the damage fluence of the material but is made as high as possible to maximize the signal-to-noise, and hence, maximize the measurement sensitivity. The requirements on the probe laser are less stringent; higher powers give better signals but if the power is made too high, the probe beam itself will induce a photothermal response in the material. The beams are aligned such that the focal plane of the pump intersects with the probe beam. A coating is scanned along an axis close to parallel with the propagating beams. When the coating passes through the focus of the pump laser, a maximum photothermal perturbation is observed in the coating. The perturbation creates a phase distortion term of $\exp(-i\Delta\phi)$ that is multiplied to the amplitude of the mathematical representation of the probe beam. The phase perturbation $-i\Delta\phi$ is small compared to 1 and can be approximated in this limit, to first order in $\Delta\phi$, to be

$$e^{-i\Delta\phi} \approx 1 - i\Delta\phi. \tag{2.11}$$

When the result of the small-signal expansion in Equation 2.11 is multiplied to the original propagating wave, one is left with the original propagating plane wave and

another weak diffracting wave co-propagating with the original wave. At $z = 0$, where the weak wave originates, the two waves are out of phase by $-\pi/2$ and no intensity contrast exists. When $z = z_R = \pi w_0^2/\lambda$ (the Rayleigh range of the weak wave), the intensity contrast is a maximum and is

$$\frac{\Delta I}{I} = \Delta\phi, \tag{2.12}$$

where w_0 is the radius of the weak wave at $z = 0$, ΔI is the difference between the intensity maximum and minimum and I is approximately the intensity of the much stronger unperturbed wave. To probe $\Delta I/I$ at z_R from the creation of the weak wave, an imaging system is used to capture this point in space on a photodiode.

Even at the signal maximum, the signal is small and requires lock-in amplifier detection. The lock-in amplifier receives a periodic signal from the chopper that modulates the pump beam. The modulated pump creates a material perturbation that is also modulated at the same frequency with some time delay, consequently, the measured interference signal is periodic with the same frequency as the chopper but with some time delay. The lock-in amplifier looks for signals only with the same frequency as the reference signal and amplifies this signal. This reduces the noise from the unperturbed probe wave, which is not chopped, and any other stray signals reaching the detector not at the reference frequency.

An example signal measured by PCI is shown in Figure 2.14.

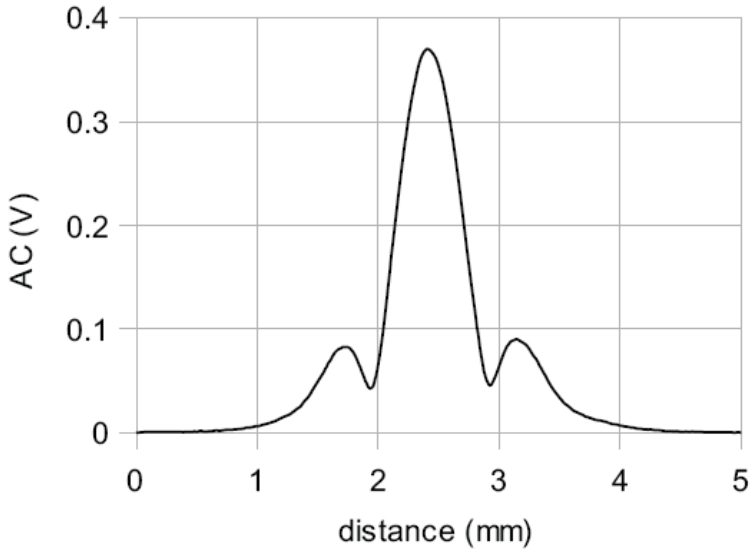

Figure 2.14: An example of a PCI measurement made as a coating is scanned through the focus of the pump beam. The maximum voltage is proportional to the optical power absorbed by the coating. Side fringes are observed on either side of the most intense interferometric fringe. Taken from Alexandrovski *et al*.[15]

The measured signal, which is proportional to the intensity of the light at the image point, is communicated as a voltage. Side interference fringes are visible on either side of the most intense fringe. The peak voltage is converted to an absolute absorption value through a calibration sample. A highly-absorbing thin film absorption, on the same substrate material used for the measurement of the unknown absorber, can be measured using more conventional transmission- and reflection-based techniques. The voltage measurement of the highly-absorbing sample, when measured with the PCI, can be directly converted to absorption. The measured voltage ratio of calibrant to unknown is equivalent to the absorption of the calibrant to the unknown due to the linearity of the measured signal with respect to the material absorption.

2.2.3 Variable angle spectroscopic ellipsometry (VASE)

General description

The complex refractive index, as a function of wavelength and thickness of thin films was measured using a variable angle spectroscopic ellipsometer (VASE) from J. A. Woollam Co. Reference 64 gives a complete description of the system, measurement

and data extraction. A schematic of the technique is shown in Figure 2.15.

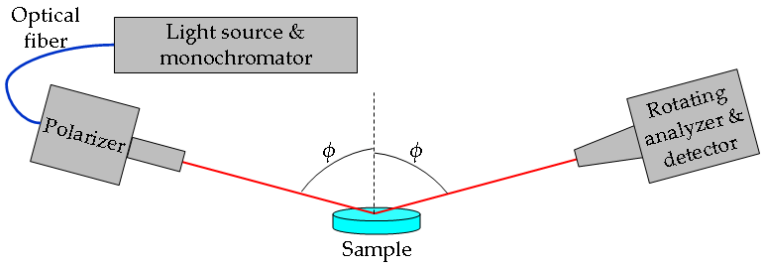

Figure 2.15: Schematic of the J. A. Woollam VASE. The change in polarization upon reflection from a sample is measured as a function of wavelength and angle ϕ.

The VASE system measures the polarization state of a light beam (ellipsometry) as a function of incident angle ϕ and wavelength λ after interacting with a sample, in terms of the ellipsometric variables Δ and Ψ. From the polarization change, measured for many wavelength and incident angle combinations, the thickness and complex refractive index of thin films can be determined.

The wavelength of incident light on the sample is selected from a broad-band light source (Xe arc lamp) using a dispersive monochromator. The Xe arc lamp emits, with sufficient intensity for making measurements, at wavelengths from 260 nm to 2 µm. A monochromator, like the one used in a spectrophotometer, disperses the wavelength spectrum into its components and selects a narrow range of wavelengths. The monochromatic light is chopped (for lock-in detection), and passed down an optical fiber to a polarizer. The optical fiber transmission allows for consistent coupling between different system components.

A polarizer is necessary to generate a polarized optical field from the randomly polarized light passed from the monochromator. The change in polarization measurement requires a well-defined incident polarization. The linear polarizer is a crystalline material with orthogonal optical "fast" and "slow" axes. Ideally, only light with polarization parallel with the fast axis is transmitted, generating light that has a polarization along a line.

Light, with a well-defined polarization, illuminates the sample at an incident angle ϕ determined by the angle of rotation of the sample stage. A second rotating

platform rotates to collect the specular reflection from the sample. On this platform is a rotating analyzer and Si detector. The interaction of the light with the material is considered later. The rotating analyzer is a second linear polarizer that is rotated with some angular frequency ω. The polarization of light incident on the analyzer has an arbitrary ellipsoidal polarization, meaning that the electric field vector traces an ellipse in time. If the sample-reflected polarization is completely linear, then the signal transmitted to the photodiode is different from zero only when the analyzer is parallel with the sample-reflected polarization, leading to a measured voltage that goes to zero and a maximum at angular frequency ω. Conversely, if the sample-reflected polarization is perfectly circular, then the analyzer passes a constant signal to the photodiode. Generally, the signal passed measured by the photodiode is a periodic signal $V(t) = V_{\mathrm{DC}} + a\cos(2\omega t) + b\sin(2\omega t)$. It is from the ratio of a/V_{DC} and b/V_{DC} that Ψ and Δ are calculated.

Basic theory of the measurement

The following analysis is for a single transparent thin film on a thick bulk substrate. The ellipsometric variables measured are Ψ and Δ, which are related to so-called pseudo-Fresnel reflection coefficients $\tilde{R}_s$ and $\tilde{R}_p$ through

$$\rho \equiv \frac{\tilde{R}_p}{\tilde{R}_s} = \tan(\Psi)e^{i\Delta}. \tag{2.13}$$

The pseudo-Fresnel reflection coefficients are calculated independently for s- and p-polarizations and are

$$\tilde{R}_{s,p} = \frac{r_{01} + r_{12}e^{-i2\beta}}{1 + r_{01}r_{12}e^{-i2\beta}}, \tag{2.14}$$

where, for either independent polarization, r_{ij} is the Fresnel reflection coefficient given by Equations 1.8 and 1.9 for the i-j interface. The subscripts $i, j = 0, 1, 2$ represent air, the film and the substrate, respectively. The phase thickness of the thin film with physical thickness d_1 is β and is given by

$$\beta = \frac{2\pi n_1 d_1 \cos(\phi_1)}{\lambda_0}. \tag{2.15}$$

From the measured signal $V(t) = V_{DC} + a\cos(2\omega t) + b\sin(2\omega t)$, the parameters α and ξ are defined as

$$\alpha \equiv \frac{a}{V_{DC}} = \frac{\tan^2(\Psi) - \tan^2(P)}{\tan^2(\Psi) + \tan^2(P)} \tag{2.16}$$

and

$$\xi \equiv \frac{b}{V_{DC}} = \frac{2\tan(\Psi)\tan(P)\cos(\Delta)}{\tan^2(\Psi) + \tan^2(P)}. \tag{2.17}$$

The ellipsometric variables are then computed from the measured signal as

$$\tan(\Psi) = \sqrt{\frac{1+\alpha}{1-\alpha}}\,|\tan(P)| \tag{2.18}$$

and

$$\tan(\Delta) = \frac{\xi\tan(P)}{\sqrt{1-\alpha^2}\,|\tan(P)|}. \tag{2.19}$$

Modeling of a thin film

Values of film n, κ and d are extracted through mathematical models, which contain parameters that are fit to the experimental data. The experimental data include VASE data taken at multiple wavelengths and angles near Brewster's angle for the investigated films and often transmission data taken at normal incidence with a spectrophotometer. A model consists of a substrate with previously measured or known optical constants. A film is placed on the substrate characterized by d and either n and κ at every measured wavelength or by wavelength-dependent physically-relevant functions for n and κ represented as $n = n(c_1, c_2, ..., c_i)$ and $\kappa = \kappa(\gamma_1, \gamma_2, ..., \gamma_j)$. Fitting algorithms are used to fit the c_is and γ_js until they yield n and κ and, consequently, Ψ and Δ that satisfactorily represent the experimentally measured Ψ and Δ. To simultaneously determine three or more parameters from measurements of only Ψ and Δ, a

model must be used. Also, the c_is and γ_js can be physical interpretations of the measurement such as surface roughness, composition and non-uniformities of the film.

The model we typically use for the refractive index of single layers is the Cauchy dispersion model, which is valid for transparent materials, given by

$$n(\lambda) = A_n + \frac{B_n}{\lambda^2} + \frac{C_n}{\lambda^4}. \tag{2.20}$$

The corresponding model for κ is the Urbach absorption tail

$$\kappa(\lambda) = A_\kappa \exp\left[B_\kappa\left(\frac{1}{\lambda} - \frac{1}{C_\kappa}\right)\right]. \tag{2.21}$$

An example of ellipsometric data taken and a fit to the data using a Cauchy dispersion formula is given in Figure 2.16.

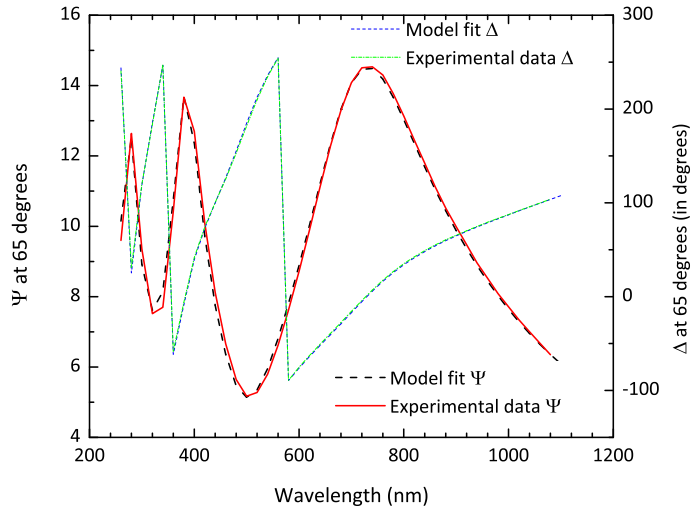

Figure 2.16: Ellipsometric variables Ψ and Δ measured at 65° along with data generated by a Cauchy model fit for a scandium oxide film deposited on fused silica.

The data presented in Figure 2.16 are from a single layer of scandia deposited on fused silica with the ellipsometer set at an incident angle of 65°. Ellipsometric data taken at 60° and 70° were also used to compute the fit and the resulting dispersion curve is given in Figure 2.17.

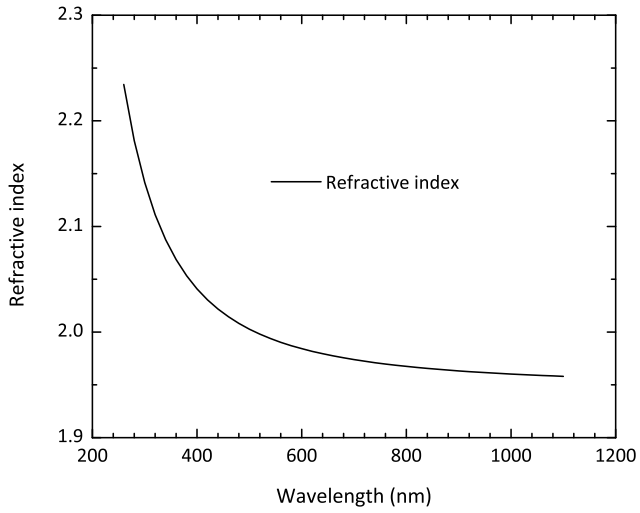

Figure 2.17: Refractive index of a scandia thin film on fused silica calculated from a Cauchy fit to the experimental data presented in Figure 2.17. The extinction coefficient was below the detection limit of the instrument.

The purpose of measuring at multiple angles near Brewster's angle is to acquire multiple data points at each wavelength, making the fit to the data more robust while exploiting the sensitivity gained by the vanishing *p*-component reflection at Brewster's angle. Adding transmission data at wavelengths corresponding with VASE measurements adds accuracy to the fit and also provides a way to compensate for the reflection from the substrate backside that might reach the detector.

2.2.4 Electron paramagnetic resonance (EPR)

Electron paramagnetic resonance (EPR) is a pump-probe absorption technique used to detect magnetic-dipole moments in atoms or molecules, which result from unpaired electrons and magnetic nuclei.[65] Orbital energy levels of a single electron are split using an external magnetic field. The energy difference can be used to absorb electromagnetic radiation, in the microwave regime. The energy of the absorbed photons, for a given applied magnetic field, is characteristic of the environment of the electron or magnetic nuclei. Unpaired electrons are of most interest here.

The splitting of energy levels in an externally applied magnetic field is called the Zeeman effect.[12] A diagram of the effect is shown in Figure 2.18.

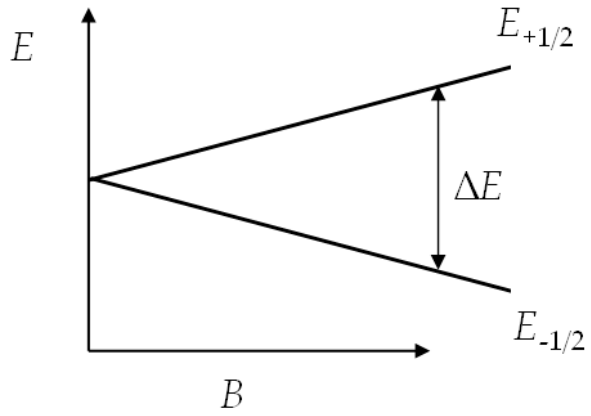

Figure 2.18: Schematic of the Zeeman splitting of the $s = 1/2$ and $s = -1/2$ energy levels E in an external magnetic field with strength B.

Electrons have an intrinsic "spin" characterized by a quantum number s, which can take the value -1/2 (called the spin down state) or 1/2 (spin up). When an external magnetic field is applied, the electron can take two possible states where its spin orients itself either parallel (spin up) or anti-parallel (spin down) with the magnetic field. The two states are separated by $\Delta E = E_{+1/2} - E_{-1/2} = g\mu_B B$, where μ_B is the Bohr magneton and g is the Landé g-factor.[66] For a free electron, the g-factor is $g \approx 2.0023$. Bound electrons have unique g-factors, depending on the local magnetic fields, that can be used to identify the particular "spin species."[65] Unpaired electrons have one of the energy states available. Electrons in the lower energy state $E_{-1/2}$ can absorb photons with energy resonant with ΔE and jump to the $E_{+1/2}$ state. EPR spectroscopy is concerned with determining the photon energy-magnetic field strength pair that produces the resonance condition.

A schematic of an EPR spectrometer is shown in Figure 2.19.

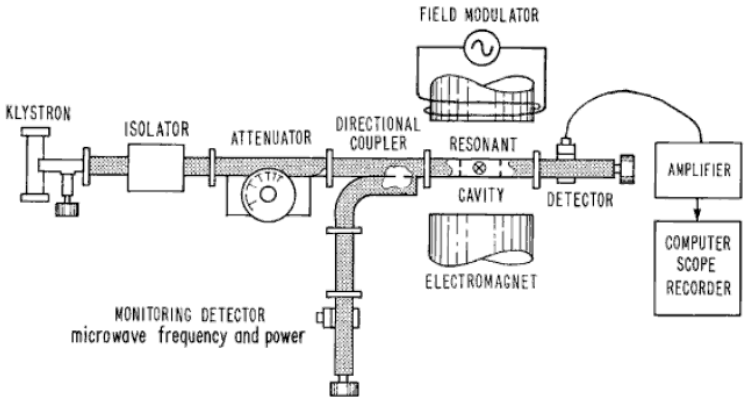

Figure 2.19: Schematic of an EPR spectrometer. Taken from Weil and Bolton.[65]

The particular spectrometer used in our experiments is a Bruker EMX EPR spectrometer.[66] The measurement is conducted by measuring the absorption of microwaves with some energy when the magnetic field strength is swept. The external magnetic field is generated by passing current through a pair of coiled electromagnets. The field strength B is varied by varying the current passing through the coils. The magnetic field is parallel with the common axis of the coils.

Microwaves are generated by a Klystron tube, which is an evacuated metal cavity that resonates at the selected microwave frequency and can be tuned by applying voltages to the klystron.[65] Microwaves are conducted through a waveguide into a resonant cavity (analogous to the optical cavity in a laser system in which the microwaves are confined by a pair of "mirrors") in which the measured sample is placed, surrounded by the electromagnets producing the external field. An iris controls the amount of microwave power admitted into the resonant cavity and matches the impedance of the cavity to the waveguide. At resonance, a standing wave pattern exists, which is generated when a round-trip traveled by the microwaves in the resonant cavity is an integer multiple of the wavelength of the microwave radiation. When the cavity is tuned and resonance achieved, a minimum in reflected power from the cavity and a corresponding maximum in power and measurement sensitivity exists in the cavity. Introducing a sample into the cavity changes the resonant condition and the cavity must be tuned accordingly. When the impedance of the waveguide is matched with the impedance of the cavity, the cavity is said to be critically coupled. Before a mea-

surement, the iris and microwave frequency are adjusted to minimize the reflected microwave power for the current cavity conditions. When the applied magnetic field induces Zeeman splitting corresponding to the microwave energy, the cavity impedance increases and is no longer critically coupled with the waveguide resulting in reflected microwave energy that is measured as the EPR signal, which is proportional to the magnitude of the absorption of the paramagnetic species in the resonant cavity.

The microwave power reflected from the cavity is measured using a Schottky barrier diode. The small absorption signals require the use of phase sensitive detection. The detection scheme works by modulating the magnetic field pump sinusoidally (typically at $\sim$ 100 kHz). Because the applied magnetic field has a time-varying periodic amplitude, the measured absorption also has a time-varying amplitude at the same temporal frequency as the modulated field B. A lock-in amplifier detects and amplifies only measured signals of the same frequency as the B-field modulation, thus, drastically improving the signal-to-noise ratio. If the amplitude of the pump field is small compared to the linewidth of the absorption, then the measured detector current is proportional to the slope (first derivative) of the absorption signal as illustrated in Figure 2.20 taken from Weil and Bolton.[65]

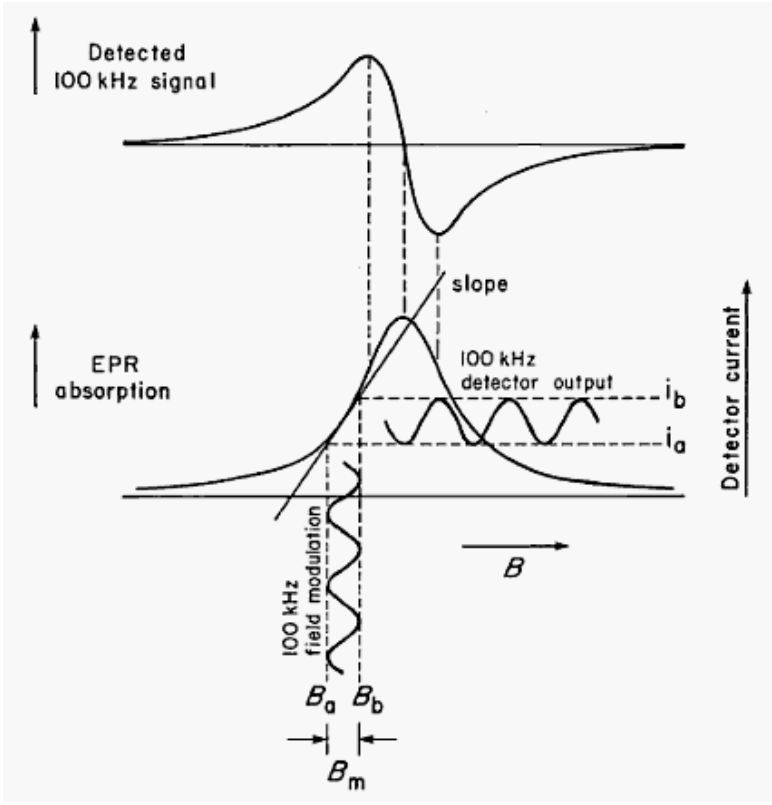

Figure 2.20: Illustration showing how the field modulation results in the detection of the first derivative, with respect to B, of the EPR absorption signal. Taken from Weil and Bolton.[65]

The measured EPR signal versus B, for a known microwave frequency ν ($E = h\nu$), can be used to determine the g-factor through the equation

$$g = \frac{h\nu}{\mu_B B}. \tag{2.22}$$

Because of the interactions of paramagnetic species in solids with surrounding atoms, the g-factor might take on slightly different values for different sample orientations relative to **B** and the polarization of the microwave radiation.[65] Generally, **g** is a tensor that can be expressed in terms of its principle values as $\mathbf{g} = [g_x, g_y, g_z]$ where x, y and z form a right-handed coordinate system. A sample Sc_2O_3 EPR spectrum is shown in Figure 2.21 with a fit using the EasySpin EPR MATLAB tool, which extracted the three principle values of **g**.[67]

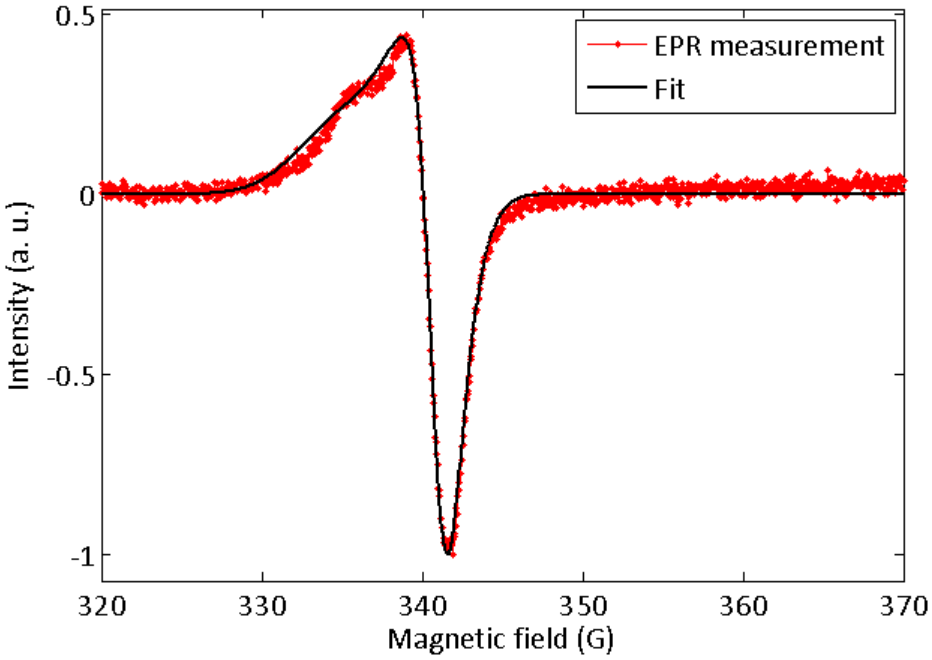

Figure 2.21: EPR spectrum of a scandium oxide layer deposited on fused silica. The EasySpin EPR MATLAB tool was used to extract $\mathbf{g} = [2.07, 2.08, 2.05]$.[67]

2.2.5 X-ray diffraction (XRD)

X-ray diffraction (XRD) is a technique that uses x-ray photons ($\lambda \sim 10^{-8}$ to 10^{-12} m) to scatter off of atoms in a crystal lattice to determine the geometry of the crystal. A comprehensive study of XRD is given in the text of Cullity.[68] X-rays have wavelengths that correspond with atomic spacing in solids ($d \sim 10^{-9}$ m), making it possible for reflections from consecutive planes to interfere. The intensity and angular dependence of peaks resulting from constructive interference are characteristic of a crystal.

A schematic of an XRD system is given in Figure 2.22.

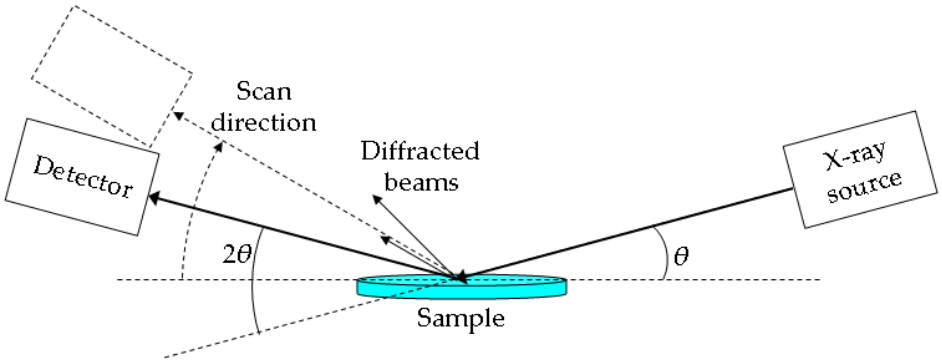

Figure 2.22: Schematic of an XRD diffractometer.

X-rays are emitted from a source and incident on the measured sample. A detector collects the diffracted beams as a function of 2θ. The diffractometer used throughout our experiments is a Bruker D8 Discover. The x-ray source was photon emission from the electron deexcitation from the L-shell to the K-shell in copper (called Cu $K\alpha$ emission). The wavelength of Cu $K\alpha$ is $\lambda = 1.5 \times 10^{-10}$ m. This type of x-ray emission can occur when the x-ray-emitting metal is an anode in a vacuum tube to which electrons are accelerated to high energies. Provided the fast electrons have enough energy, they can remove electrons from the inner K-shell in a metal, such as Cu. Electrons in outer shells can then transition to the vacant lower energy state, emitting photons with energies corresponding to the electronic energy difference.

In our experiments, the measured materials are thin films deposited on substrates. To reduce the diffraction signal from the substrate, the technique called glancing-angle XRD (GAXRD) was used in which the incident angle of the x-rays is made to be very small ($\theta = 0.5°$) and fixed throughout the measurement. The detector is then scanned to collect diffracted x-rays. The shallow incident angle minimizes the depth into the substrate the x-rays can travel.

The detector used in our experiments was a scintillation detector, which works by producing luminescence in a material when ionizing radiation (diffracted x-rays) is incident. A photodetector then measures the intensity of the light emitted, which is proportional to the intensity of the x-rays reaching the detector. The nature of the sample-x-ray interaction is now considered.

Atoms in a crystal form a periodic array. A simple two dimensional array is illustrated in Figure 2.23.

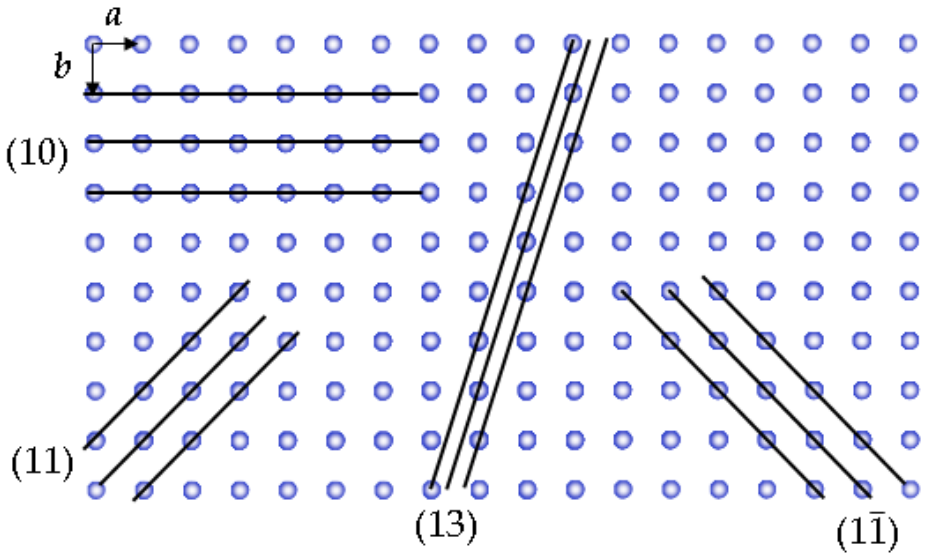

Figure 2.23: Two-dimensional lattice array illustrating crystalline planes with associated Miller indices. After Cullity.[68]

In Figure 2.23, a series of lines has been drawn that represent some of the planes formed by the periodic array. The planes are described by their directions relative to the origin of the array. The array in Figure 2.23 has a unit cell of dimensions $a \times b$ and the Miller indices, which characterize each plane, give the number of unit cells traversed in each direction to locate consecutive atoms along the plane. For instance, the plane denoted (13) in Figure 2.23, requires a to be traveled horizontally and $3b$ to be traveled vertically to draw a line for that plane. For each set of parallel planes (and sets of planes with the same Miller indices) is a unique spacing between planes.

X-rays incident on a crystal reflect and scatter, as diagrammed in Figure 2.24.

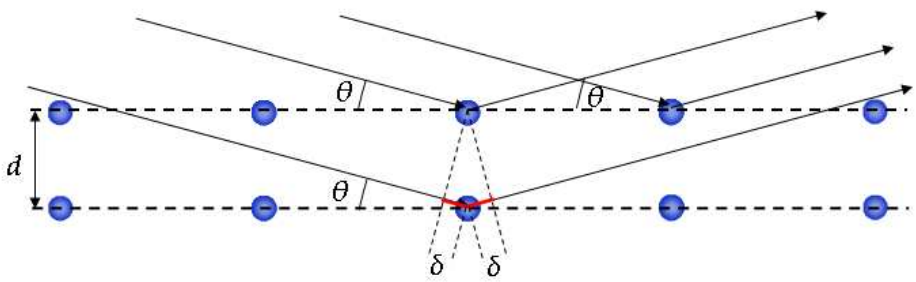

Figure 2.24: Illustration used to demonstrate the Bragg effect in scattering from a periodic array of atoms. After Cullity.[68]

What is observed at the detector is the summation of all of the scattered waves. When the path difference between scattered waves is zero or an integer multiple of λ ($2\delta = 2d\sin(\theta) = m\lambda$), the Bragg condition is met and the waves constructively interfere. At observation angles not satisfied by the Bragg condition, destructive interference occurs and the measured signal is small. The constructive interference upon scattering gives rise to diffraction peaks for given plane separations, which are recorded when a detector is scanned through 2θ. An XRD scan of a bulk quartz crystal and scandium oxide thin film is shown in Figure 2.25.

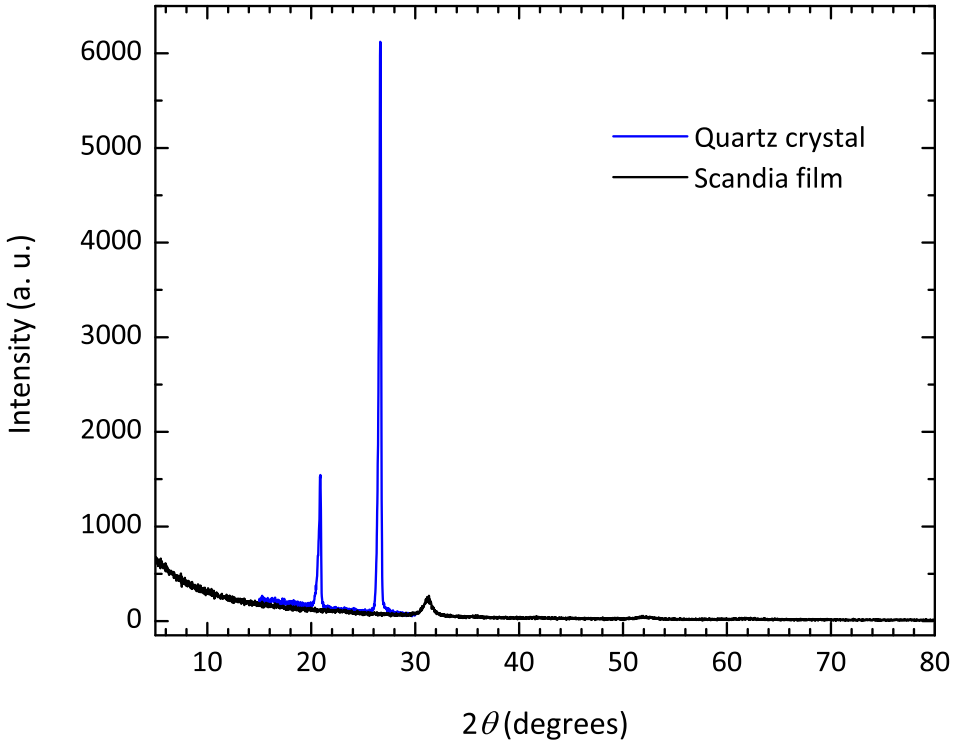

Figure 2.25: Comparison of the diffraction patterns from a bulk quartz crystal and a scandium oxide thin film taken on a Bruker D8 Discover.

The spectrum of the bulk quartz crystal shown in Figure 2.25 represents the "ideal" crystalline solid with distinct and narrow diffraction peaks. The width of the diffraction peak is determined by characteristics of the diffractometer such as linewidth of the x-ray radiation, the spread in angles of the x-ray radiation, the finite aperture of the system, etc, and can be used to quantify the system broadening. Compared to the scandium oxide film, the diffraction peaks of the quartz are much narrower and more intense. This is mostly because the scandia film is amorphous, in other words,

it has short-order periodicity. In a purely amorphous solid or liquid, there exists a broad diffraction peak corresponding to the statistical average of interatomic spacing. The thin film is modeled as a three-dimensional mosaic of small crystallites, with periodicity inside each crystallite, with a spread in orientation relative to each other. Another broadening mechanism in materials is non-uniform microstress, which can add a distribution in planar spacing for a given crystal plane, yielding a distribution in the angular spectrum of the diffraction peaks. Macrostress in the material, in which the entire solid structure is strained, can compress or expand the interatomic spacing; consequently, the diffraction peak can be shifted to higher or lower angles as d is made smaller or larger, respectively.

Chapter 3

Experimental Results

The details and results of a systematic study of single layers of scandium oxide deposited using reactive ion beam sputtering, with varying deposition oxygen partial pressures p, are presented in this chapter. As will be shown, the partial pressure during deposition has a large influence on the near-infrared absorption loss. It is further shown that increasing p causes an increase in the interstitial oxygen defects that, in turn, affect the absorption

3.1 Experimental techniques

3.1.1 Ion beam sputtering of scandia films

Sc_2O_x single layers were deposited on Si and fused silica substrates. A scandium metal target was used to generate scandia thin films when the oxygen was flowed into the deposition chamber resulting in molecular oxygen partial pressures in the deposition chamber in the range from 2 to 40 µTorr as measured by a risidual gas analyzer (RGA) calibrated with an ion gauge. The chamber temperature was maintained at 100°C during deposition. Deposited films had nearly constant thicknesses of 205 nm $\pm$ 7 nm. Transparent films were obtained except for an opaque film deposited with an oxygen partial pressure of 2 µTorr. Argon was used for the ion beams and neutralizers and the Ar partial pressure was fixed at 1.5×10^{-4} Torr during operation. The main sputtering

beam was 16 cm in diameter and had a beam energy of 1.25 keV and beam current of 600 mA. An assist source, directed at the depositing film, was 12 cm in diameter, had 0.2 keV beam energy and 50 mA beam current. The chamber base pressure before deposition was 7×10^{-7} Torr.

3.1.2 Characterization of the optical properties

Optical properties of the transparent films were investigated using a Hitachi U-2010 spectrophotometer (see Section 2.2.1) in the wavelength range 190 to 1100 nm and a J. A. Woollam variable angle spectroscopic ellipsometer (VASE) (see Section 2.2.3) in the wavelength range 250 nm to 1100 nm and at incident angles of 60°, 65° and 70°. The thickness and optical constants of the transparent films were determined using a combination of transmission and ellipsometric data in the range 250 nm to 1100 nm. The refractive index of the opaque film was determined from ellipsometric measurements while its thickness was measured using a Tencor α-step profilometer.

The absorbance of the transparent films, in the ultraviolet, was determined as the difference in the transmittance of an uncoated substrate and the local transmittance maxima of each sample. At the local maxima in the transmittance, the reflections from the air-film and film-substrate interfaces destructively interfere. Any decrease in transmittance from the substrate value is caused by absorption in the thin film.

The optical absorption of the films, deposited on fused silica, was measured at $\lambda = 1.064$ µm with the photothermal commonpath interferometry (PCI) technique (see Section 2.2.2). A 1.064-µm pump beam was used to excite a thermal response in the coating, while commonpath interference of a 633-nm He-Ne probe beam allowed for detection of the absorption of the film at the pump wavelength. The setup used has a detection limit of 0.1 ppm and an absolute accuracy better than 5%.

3.1.3 Stress measurements

A Twyman-Green interferometer, employing a He-Ne laser, was used to determine the stress in the deposited layers on 1-mm thick fused silica substrates. The interferometer

is illustrated in Figure 3.1.

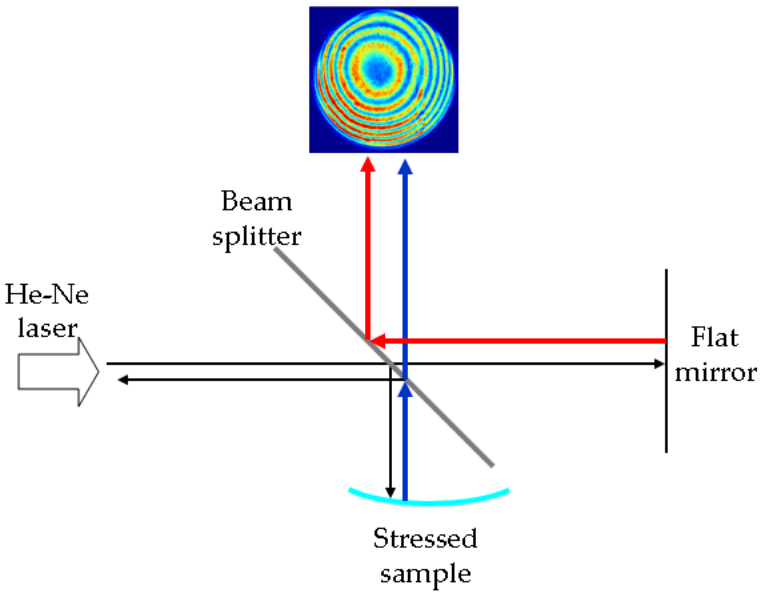

Figure 3.1: Schematic of the Twyman-Green interferometer used to measure the radius of curvature of stressed samples. The curved wavefront and flat wavefront add to produce the concentric ring interference pattern.

A He-Ne laser, with flat wave fronts, is split into two beams using a partially transmitting beam splitter. One beam reflects off of an optically flat mirror, maintaining its wavefront flatness, while the second beam reflects off of a sample and the two beams recombine and are imaged using a charge-coupled device (CCD camera). For a perfectly flat sample, all rays along the cross section of the beams travel a uniform optical path length difference. If, however, the film has stress causing the substrate to flex, the beam reflecting off of the curved surface no longer has a flat wavefront. The combined beams then have traveled different path lengths over the area of the beam, resulting in concentric rings representing areas of the recombined beam where the two beams have a uniform path difference. Fits of five phase-shifted interference patterns to Zernike polynomials were used to determine the radius of curvature of the film-substrate structure based on a calibration of a 30.0-m radius of curvature fused silica standard. Film stress was assumed to be proportional to the inverse of the radius of curvature of the structure.[69]

3.1.4 X-ray diffraction measurements

Glancing angle x-ray diffraction (GAXRD) scans (see Section 2.2.5) were taken as a function of 2θ using a Bruker D8 Discover instrument employing Cu K_α radiation at 0.5° incidence. Data were acquired for films deposited on Si in 0.02° steps in 2θ. The diffraction peak locations and widths were determined from fitting the peaks to a Lorentzian lineshape. Using the full-width at half of the peak maximum (FWHM) of the 26.6° Bragg diffraction peak of a crystalline quartz standard and Scherrer's method, the crystallite size was estimated.[70] The crystallite length is estimated using the equation

$$l = \frac{\lambda}{\beta \cos(\theta)}, \tag{3.1}$$

where $\lambda = 0.15$ nm is the wavelength of the x-rays used, θ gives the angular position of the broadened diffraction peak and β gives the system broadening (in radians) determined from the subtraction of FWHM of the crystalline standard from the FWHM of the broadened peak.

3.1.5 Electron paramagnetic resonance

Electron paramagnetic resonance (EPR) (see Section 2.2.4) studies were carried out using a Bruker EMX EPR spectrometer with 100 kHz field modulation at room temperature. Films were deposited on thin fused silica slides and placed in a quartz sample tube. Spectra for each deposition were taken for nearly equivalent film volumes, in the same cavity, on the same day and with the film surface normal parallel with the microwave propagation. The microwave frequency used to probe the spin populations was 9.6 GHz for the measurements taken. Background spectra collected confirmed that the bare substrates and quartz sample tube contributed negligible signal compared to the signals measured from the scandium oxide. The small background signal was subtracted from the scans of the scandia films. The opaque film was too lossy, such that the system could not be critically coupled, and was not measured.

The relative spin concentrations were determined from the relative areas of the absorption signals, which were determined from integrating the derivative signal that was measured. The EasySpin MATLAB library was used to fit the spectra to extract a g-tensor.[67]

3.1.6 Surface roughness measurements

Atomic force microscopy (AFM) scans were made using a NovaScan AFM in tapping mode on a scandia sample deposited with 2, 5, 17, 38 and 40 µTorr oxygen partial pressure. For the measurements presented here, the scan area was 5×5 µm^2 and 512 samples were taken in each scan direction, except for the 38-µTorr film for which 170 scans were taken. The surface root-mean-square (RMS) was determined using the NovaScan software, which was also used to perform a flattening algorithm on the acquired images to remove any curvature and tilt in the image. The RMS gives a measure of the spread of the distribution of heights measured for a given scan area.

3.1.7 X-ray photoelectron spectroscopy

The chemical bonding properties of scandia films deposited with 5 and 38 µTorr oxygen partial pressure were investigated with x-ray photoelectron spectroscopy (XPS) measurements. The measurements reported in the following section were carried out employing an Al K_α monochromatic x-ray source with 1.487 keV photon energy. The incident x-ray beam made a 45° angle with the sample surface plane. Due to electron scattering in the scandia, the probe depth of the experiment is less than 10 nm from the surface. Survey scans (scans over a large range of binding energies) as well as high resolution scans (scans over a narrow range with higher resolution in energy) of the C 1s, Sc 2p and O 1s regions of the spectra were taken at the surface. To mitigate the effects of surface oxidation and organic contamination, measurements were taken after 15 min of in-situ argon ion sputtering of the surface. The argon ion beam had an energy of 2 keV and was rastered to generate a 3 mm $\times$ 1 mm spot. The C 1s peak from redeposited carbon was used to shift the XPS spectra and, hence, com-

pensate for charge-induced shifts in the spectra. The oxygen-scandium stoichiometry was calculated from the areas of the high-resolution scans, while factoring in the sensitivity factors, σ, for each element provided by the manufacturer of the XPS hardware and software, Physical Electronics. The equation used to determine the stoichiometric ratio is

$$\frac{[\mathrm{O}]}{[\mathrm{Sc}]} = \frac{\sigma_{\mathrm{Sc2p}} A_{\mathrm{O1s}}}{\sigma_{\mathrm{O1s}} A_{\mathrm{Sc2p}}}, \tag{3.2}$$

where A_i is the peak area of the ith electronic orbital and the sensitivity factors are $\sigma_{\mathrm{Sc2p}} = 1.959$ and $\sigma_{\mathrm{O1s}} = 0.733$.

3.1.8 Fourier transform infrared spectroscopy

Fourier transform infrared (FTIR) spectroscopy was used to investigate the chemical bonds in the scandia thin films deposited on Si substrates. The peaks in absorption were used to identify chemical bonds that were (and were not) evident in the scandia films presented. A scan of a bare Si substrate was subtracted from the film measurements to eliminate its contribution to the signal.

3.2 Results and discussion

3.2.1 Influence the oxygen partial pressure on the deposition rates

The deposition rates of the films deposited, as determined from thickness measurements and time of deposition, are given in Figure 3.2 as a function of oxygen partial pressure p.

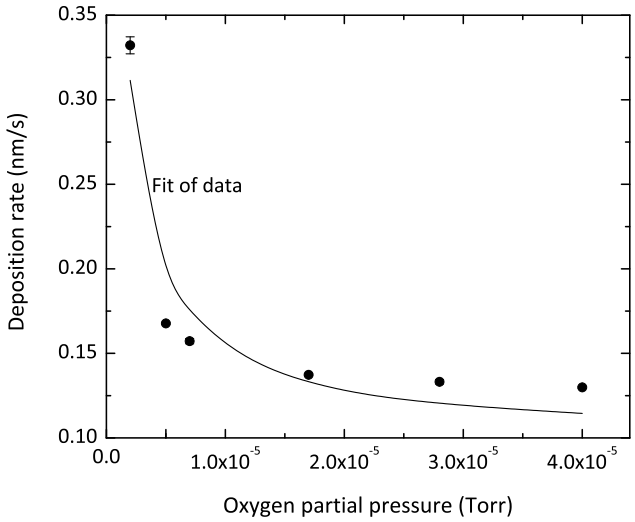

Figure 3.2: Film deposition rates varying with deposition oxygen partial pressure. The error bars are determined from uncertainties in the thickness measurements. The fit to the data is a fit of the same functional form as the target erosion rate given in Equation 2.7

The deposition rates decrease as a higher fraction of the target surface becomes oxidized. This is the well known target poisoning phenomenon and has been modeled for the reactive magnetron sputtering process.[56;55] Experimental data for the deposition rate of ZrO_2 films deposited by ion beam sputtering, for various oxygen partial pressures, showed a similar decrease in the deposition rate.[71] A corresponding model for the deposition rate is given in Reference 71. The semi-transparent film, presented here, was deposited ≈ 2.5 times faster than the transparent scandia films.

A fit to the experimental data is shown in Figure 3.2. The deposition rate was calculated from the sputtering rate given in Equation 2.7 and using the form of Equation 2.6 for the target surface coverage. The measured deposition rate has a sharper transition from metallic to oxidized sputtering than suggested by the fit. The fit yields an isothermal rate constant $k_t \sim 1 \times 10^6$ Torr^{-1}. As will be shown, films deposited with $p > 5$ µTorr were transparent.

3.2.2 Surface roughness

An AFM image of a deposited scandia surface at $p = 38$ µTorr is shown in Figure 3.3.

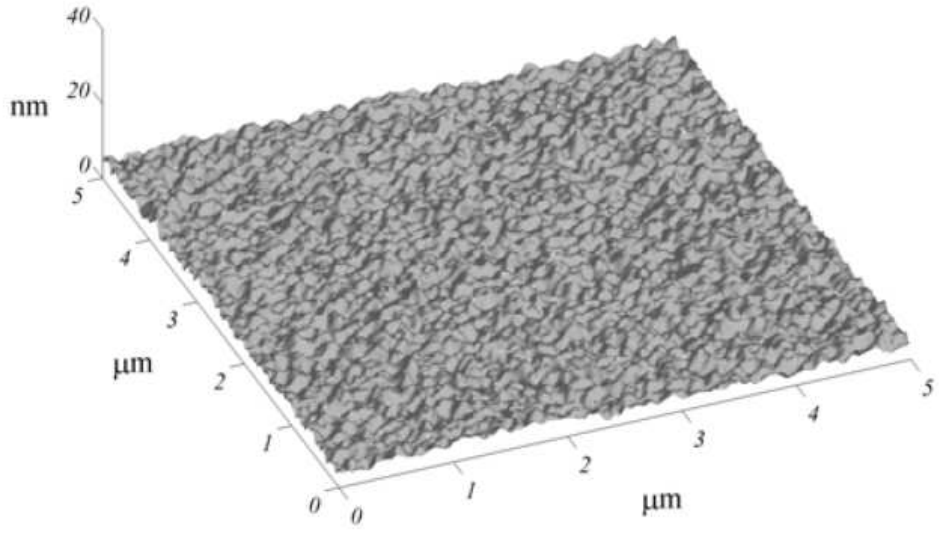

Figure 3.3: A 5×5 μm^2 section of a scandia single layer recorded by an AFM. This film has a surface roughness RMS value of 1.1 ± 0.3 nm.

The surface roughness RMS of the film shown in Figure 3.3 is 1.1 ± 0.3 nm. Other samples, deposited with 2 to 40 µTorr, have surface roughness 0.6 to 0.8 nm as shown in Table 3.1. The surface roughness of the substrate is nearly within the error bars of the measurement.

Oxygen partial pressure (µTorr)	RMS surface roughness (nm)
2	0.8
5	0.6
17	0.7
38	1.1
40	0.7

Table 3.1: RMS surface roughness of Sc_2O_x films at various oxygen partial pressures measured with an AFM.

Besides the roughest film deposited with 38 µTorr oxygen partial pressure, the scandium oxide films are comparable to the lowest rms reported for reactive PVD (reactive PLD-deposited) scandia coatings in Reference 44 of 0.5 nm. It is important to note that these results to not reveal a drastic influence of the oxygen partial pressure on the surface roughness.

3.2.3 Optical constants

The refractive index of the films was calculated from the ellipsometric measurements of Ψ and Δ. The extinction coefficient in the transparent films is below the detection limit of the VASE instrument over 350 nm $\leq \lambda \leq$ 1100 nm. Figure 3.4 shows the dispersion for the scandium oxide thin film deposited at 5 µTorr oxygen partial pressure.

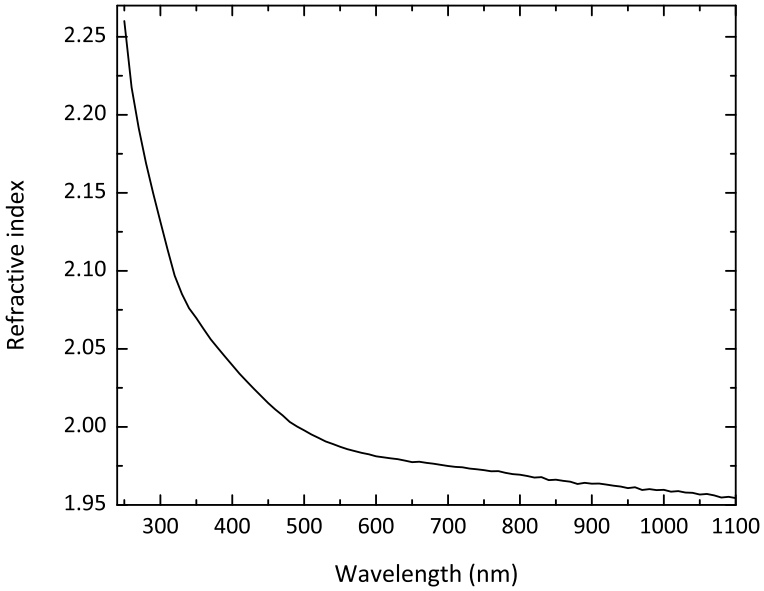

Figure 3.4: Refractive index of scandium oxide deposited with 5 µTorr oxygen partial pressure.

The refractive index in transparent samples at $\lambda = 1.06$ µm is summarized in Table 3.2.

Oxygen partial pressure (µTorr)	Refractive index at $\lambda = 1.060$ µm
5	1.957(2)
7	1.954(2)
17	1.952(3)
28	1.951(3)
40	1.951(5)

Table 3.2: The refractive index at $\lambda = 1.060$ µm at various oxygen partial pressures during deposition. The number in parentheses is the uncertainty in the last reported digit.

It is observed that the refractive index is inversely related to the oxygen partial pressure but does not vary by more than 0.3%. The refracive index of these scandia films is approximately equivalent to those of crystalline scandia measured by Xu *et al.*[40]

The refractive index of the semi-transparent film is 1.932 and 2.480 with an extinction coefficient of 0.965 and 1.269 at 0.5 and 1 µm, respectively. The transmission spectra (not pictured) show the transparent films to have UV cut-offs (half transmittance points) between $\lambda = 211$ and 213 nm. while the opaque film transmits $\sim 1\%$ over the wavlengths measured.

3.2.4 Absorption loss at λ = 1.064 µm

The 1.064-µm absorption, for all seven Sc_2O_x coatings versus oxygen partial pressure, is shown in Figure 3.5.

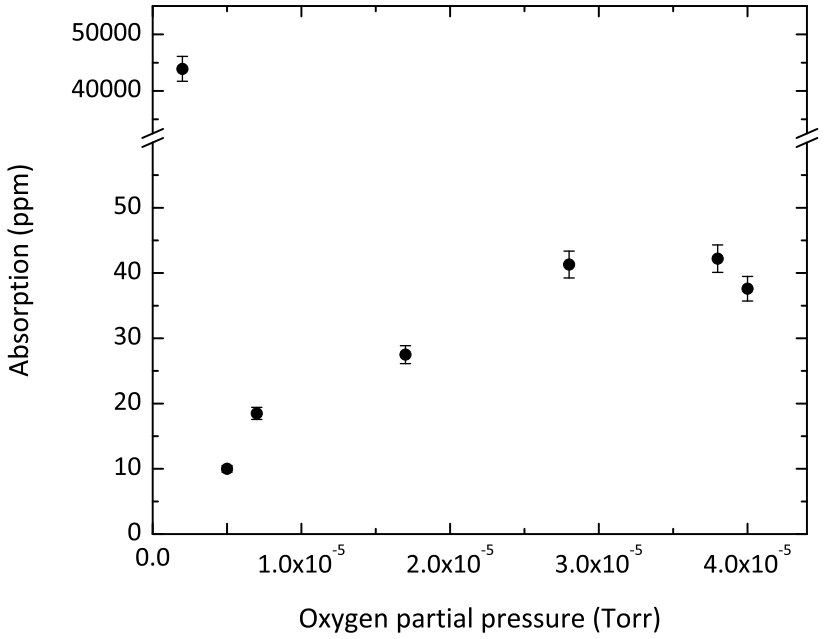

Figure 3.5: Absorption loss at $\lambda = 1.064$ µm, given in ppm, for various oxygen partial pressures during deposition. The film at 2 µTorr is opaque, while films deposited at higher oxygen partial pressures are transparent. The error bars represent the 5% accuracy in the absolute absorption measurement.

Figure 3.5 shows that there is a narrow range of oxygen partial pressures, for the given ion beam parameters, for which the absorption loss is minimum. The minimum in absorption loss at $p = 5$ µTorr is 10 ± 0.5 ppm. At lower oxygen partial pressures, the target oxide coverage is low, deposition rates are high and the films are oxygen

deficient and metal-like (on average Sc_2O_x with $x < 3$). At $p > 5$ µTorr, there is an increase in absorption, possibly due to the increased density of oxygen-created defects. A similar behavior (Figure 2.10) is seen in the extinction coefficient at $\lambda = 467$ nm in TiO_x reactively magnetron sputtered in varying oxygen partial pressures in which the extinction coefficient increases for increasing oxygen partial pressure. The increase in absorption corresponds with an increase in the O/Ti ratio above the ideal stoichiometric ratio of 2.[61] This, along with the data presented next, suggests that a similar excess-oxygen concentration develops in our reactively sputtered scandium oxide films.

The bandgap of scandium oxide is ≈ 6 eV (Table1.2) and is such that photons with 1.064 µm wavelength (1.165 eV) can only be absorbed in multi-photon processes or when defect-created band states exist in the material.

3.2.5 Near-band absorption

The near-band absorbance, shown in Fig. 3.6, demonstrates that for increasing p above 5 µTorr, the absorbance increases, indicating increasing densities of shallow energy states.

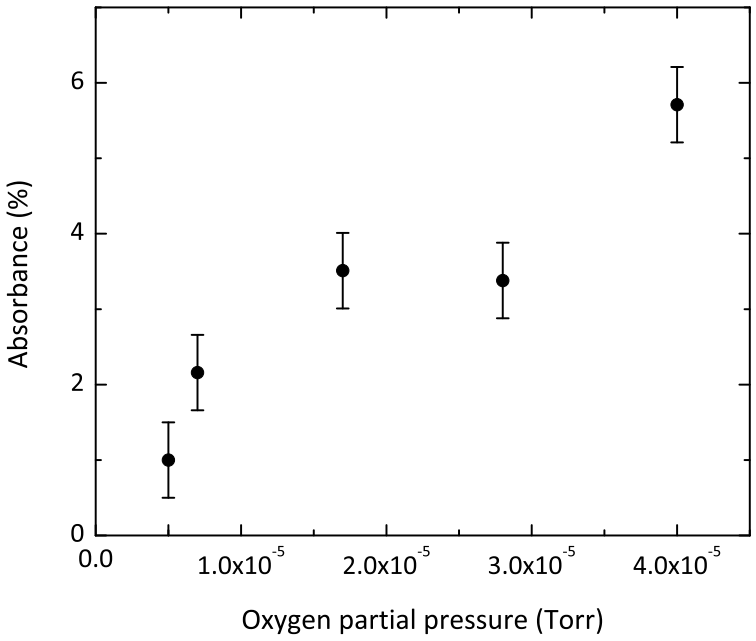

Figure 3.6: Absorbance in transparent scandia films, at $\lambda = 296$ nm, calculated from the difference in the transmittance of an uncoated fused silica substrate and the film transmittance at a maximum. The wavelengths of the maxima are indicated. Error bars are estimated based on accuracy of the transmittance measurements and the variation in wavelength of the transmittance maxima.

These results correspond with the absorption results presented in the previous section. A similar phenomenon has been reported for reactive DC magnetron sputtering of TiO_2 where excess oxygen was measured and blamed for decreasing the effective bandgap of the films when high oxygen partial pressures were used during deposition.[72]

3.2.6 X-ray photoelectron spectroscopy results

The chemical composition of transparent scandia films deposited with 5 and 38 µTorr was investigated using XPS. Survey scans showed the presence of oxygen, scandium, carbon (in very small quantities following sputtering) and argon. The carbon atomic percentage is $\sim 30\%$ of the survey signal on pre-sputtered surfaces and drops to $\sim 3\%$ after the sputter cycle. Argon, which was likely implanted during deposition and after in-situ sputtering, composes $\sim 3\%$ of the survey spectrum in the sputtered films. The

majority of the Sc 2p high-resolution signal for the 38-µTorr sample, shown in Figure 3.7, is seen to be in a single binding environment (Sc_2O_3).

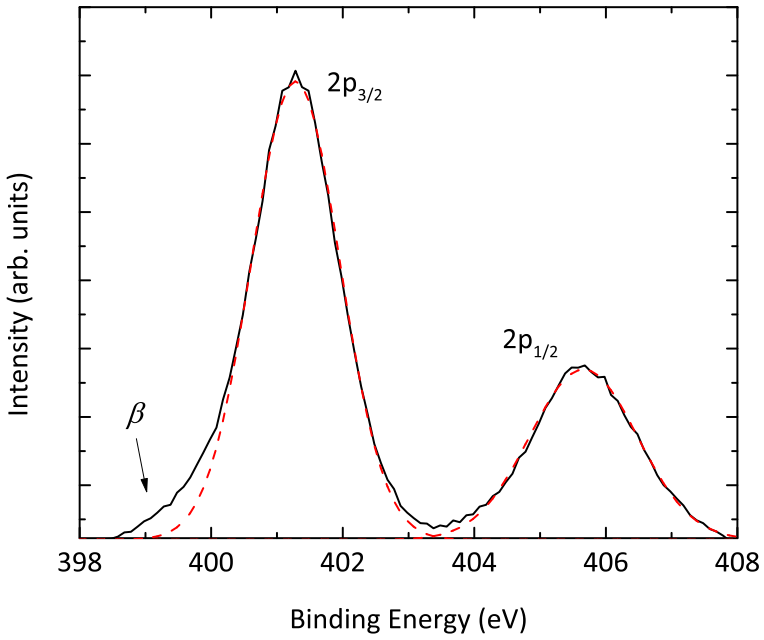

Figure 3.7: A typical Sc 2p high-resolution XPS spectrum following 15 min of Ar ion beam sputtering. The signal is deconvolved into a doublet representing Sc bound to O in Sc_2O_3. A small shoulder β is an artifact of the in-situ sputtering process.

A similar spectrum is observed for the sample deposited at 5×10^{-6} Torr. The shoulder, labeled β, does not appear in the pre-sputter scans and is considered an artifact of the Ar sputtering process during the XPS measurement. The spectra taken after sputtering of the transparent films show that β accounts for 6% to 7% of the Sc 2p signal and was accounted for in the calculation of the stoichiometry.

A post-sputter high-resolution scan of the O 1s region for the 38-µTorr sample is shown in Figure 3.8.

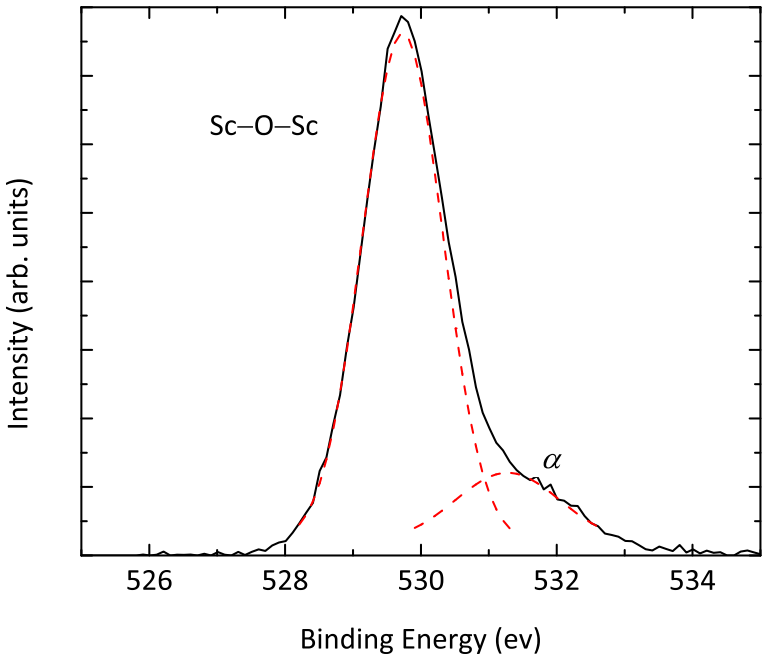

Figure 3.8: A typical O 1s high-resolution XPS spectrum following 15 min of Ar ion beam sputtering. The signal is deconvolved into two components representing Sc_2O_3 and α, indicative of oxygen-related defects and impurities.

The O 1s signal is deconvolved into 2 components 1.8 eV apart. The component at lower binding energy (529.2 eV) corresponds to oxygen in Sc–O–Sc bonds in Sc_2O_3.[41] The component labeled α in Figure 3.8 is associated with oxygen defects. The α-peak has been reported to be associated with Sc–OH and Sc–CO_3 bonds.[41] Since negligible quantities of C are measured in the sputtered samples, the α-peak is interpreted to correspond to either OH-groups or another form of oxygen. As discussed later, FTIR scans showed no evidence of OH-groups in the film bulk. The integrated area of the α component of the sputtered O 1s spectrum is 5% and 15% of the entire oxygen signal for the samples deposited with 5 and 38 µTorr, respectively. When α is accounted for in calculating the stoichiometry, a stoichimoetric ratio [O]/[Sc] $= 1.86$ and 2.05 ± 0.01 for the films deposited at $p = 5$ µTorr and 38 µTorr, respectively. Neglecting α, the stoichiometric ratio [O]/[Sc] $= 1.76$ and 1.73 ± 0.01, respectively, compared to the ideal ratio in Sc_2O_3 [O]/[Sc] $= 1.5$. Even neglecting α, the measured stoichiometric ratio demonstrates excessive oxygen in the scandia film. More accurate stoichiometric measurements could be taken using a calibration standard with a known O-Sc stoichiometry instead of relying on manufacturer-specified sensitiveity factors. The film

deposited at 5 µTorr has a significantly smaller amount of the defect-related α peak, compared with the film deposited at 38 µTorr.

3.2.7 Fourier transform infrared spectroscopy

FTIR spectra, given in Figure 3.9 showed evidence of the Sc–O bond vibration at 633 cm^{-1}.[73]

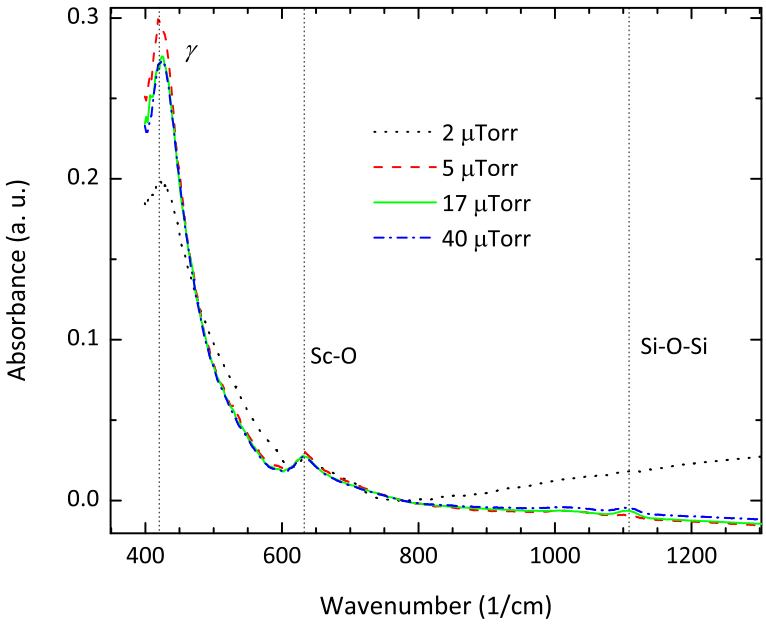

Figure 3.9: FTIR spectra of Sc_2O_x films deposited on Si. The three peaks apparent in the measurement are an unknown peak (γ) along with peaks corresponding to Sc–O and Si–O.

Also observed is a peak associated with Si–O bonds, which is likely to be an interfacial layer between substrate and film.[74] The Si–O peak is not measured in the metallic sample (2 µTorr) and is higher in the films deposited in higher oxygen partial pressures. This is not surprising, as it indicates the reaction of the silicon substrate with increasing pressures of oxygen in the deposition chamber. A third peak, labeled γ, is also seen in Reference 73. In Reference 73, this peak is seen to increase for more crystalline Sc_2O_3, though no direct mention of it is made. There are no other measurable peaks at higher wavenumbers (measurements were taken from 400 to 4000 cm^{-1}) that can be associated with OH-bonds in the films. This agrees with the fact that dense deposited IBS films should not allow for significant water absorption from the atmo-

sphere, nor should significant OH be incorporated into the film with low chamber base pressures.

3.2.8 Electron paramagnetic spectroscopy results

The nature of scandium oxide defects seen at $p > 5$ μTorr was investigated through EPR measurements. Figure 3.10 gives the EPR spectra of the transparent scandium oxide films.

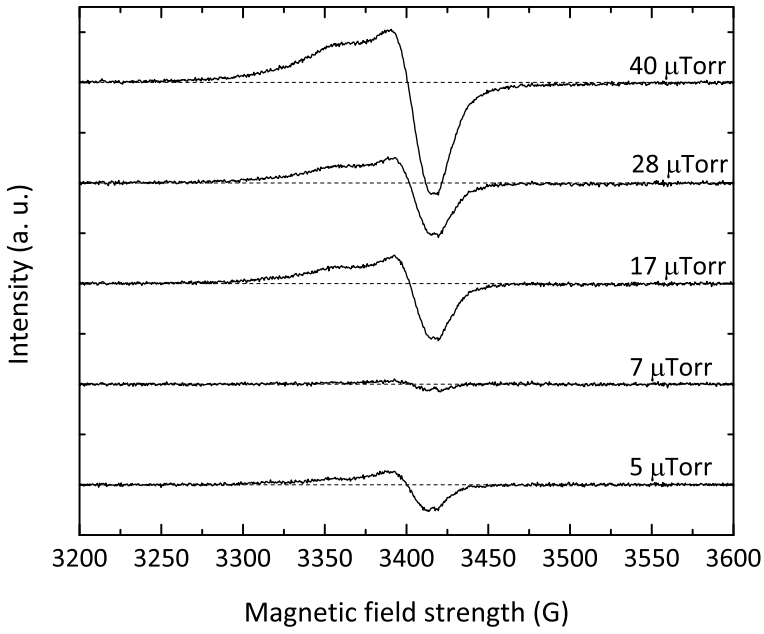

Figure 3.10: EPR signals of the transparent films aligned vertically for clarity of presentation. The oxygen partial pressure during deposition is indicated for each trace.

The EPR signals were characterized by a g-tensor $[g_{xx}, g_{yy}, g_{zz}]$ = [2.0182(4), 2.019(1), 2.0576(4)], where the number in parentheses represents the uncertainty in the last reported digit as determined from averages of fits of each sample. The concentration of the spin center increases with increasing partial pressure as shown in Figure 3.11.

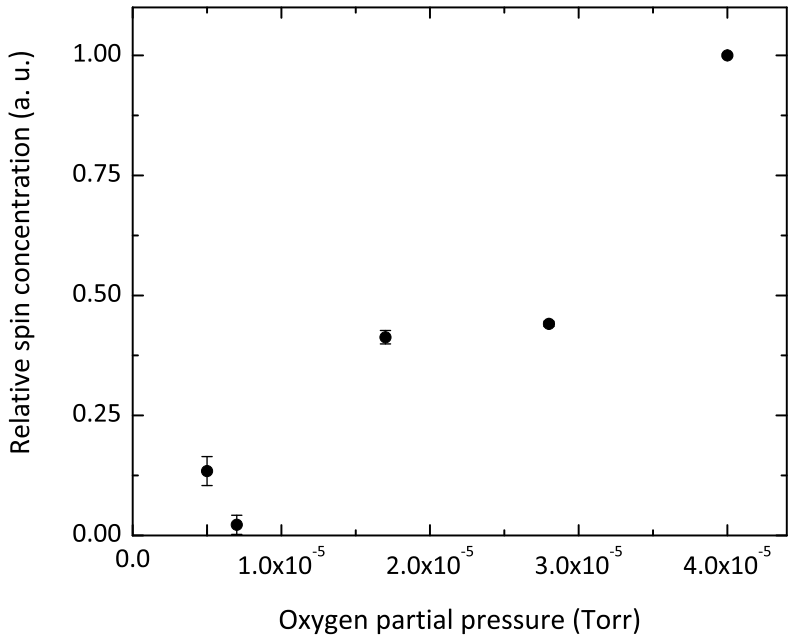

Figure 3.11: Relative spin (unpaired electron) concentrations in the transparent scandia films (proportional to the area of absorption signal) normalized to the highest concentration at 40 µTorr. The error bars result from the uncertainty in the absorption peak area determination.

The relative spin defect concentration is assumed to be proportional to the area of the absorption signal computed from the EPR spectra. Because the spin concentrations generally increase for increasing p, the measured signal is assumed to be associated with charged oxygen defects. An EPR signal in γ-irradiated ZrO_2 granulates with $[g_{xx}, g_{yy}, g_{zz}]$ = [2.0045(3), 2.0105(3), 2.0304(3)] (similar to our measured g-values) was associated with O_2^-.[75] It should be noted that the films deposited with 7 and 28 µTorr were generated nearly six months prior to the rest of the films and that environmental and laboratory incubation effects might have caused the reduction in unpaired electron defects compared to the other films.

3.2.9 X-ray diffraction and stress variation with oxygen partial pressure

X-ray diffraction scans are shown for samples investigated in this work in Figure 3.12.

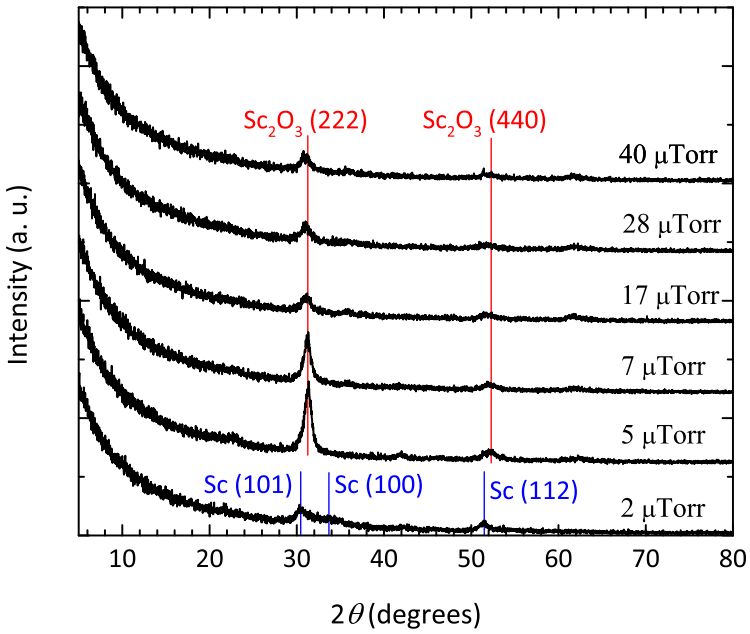

Figure 3.12: GAXRD spectra with the O_2 partial pressure indicated for each scan. Some of the diffraction planes for body-centered cubic Sc and Sc_2O_3 are indicated.

The most intense diffraction peak in the oxide films is near $2\theta = 31^\circ$ and is attributed to the (222) plane in body-centered cubic Sc_2O_3.[44;40] The films are considered amorphous as the crystallite size is determined to be $\sim$ 10 nm based on the FWHM of the (222) peak of the 5-μTorr sample compared with the crystalline quartz standard. The opaque film, deposited with 2 μTorr O_2, has diffraction peaks corresponding with the body-centered cubic phase of metallic scandium.[76]

The peak positions and FWHM for the (222)-peak in the transparent films are given in Figure 3.13.

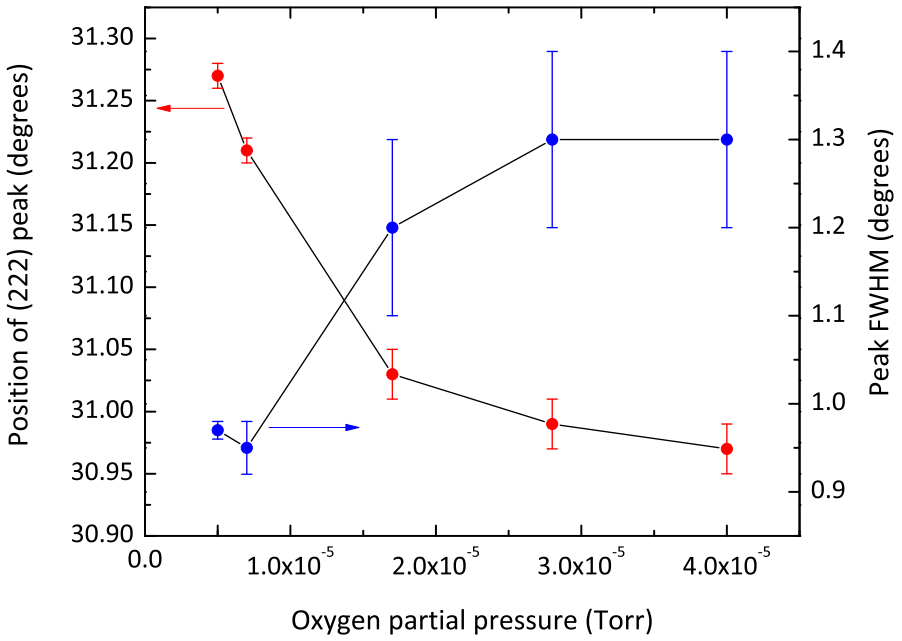

Figure 3.13: Position and FWHM of the (222) peak for the transparent films versus oxygen partial pressure. The position, FWHM and associated error bars were determined from Lorentzian peak fits.

The peak shift indicates that the lattice parameter increases with higher O_2 partial pressure. From $p = 5$ to 40 µTorr, the lattice constant increases by 0.9%. Similarly, the diffraction peak broadens with higher p, signaling a decrease in the crystallite size, strain broadening due to microstrain (plastic deformation) or both.[68] The FWHM broadens 30% over $p = 5$ to 40 µTorr.

The stress of films deposited on 1-mm thick fused silica substrates is given in in Figure 3.14.

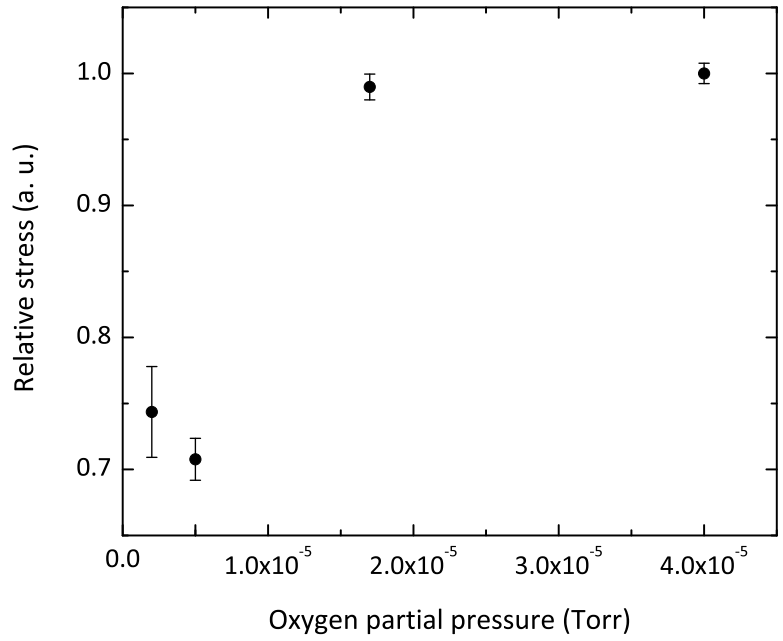

Figure 3.14: Relative stress (normalized to the highest value at $p = 40$ µTorr of 1.2 GPa) in single Sc_2O_x layers deposited on 1-mm thick fused silica substrates. The error bars represent the scatter in repeated measurements of the radius of curvature of the film-substrate structures. The minimum in stress, measured at $p = 5$ µTorr, is 0.77 GPa.

The stress ranged from 0.77 GPa ($p = 5$ µTorr) to 1.19 GPa ($p = 40$ µTorr). An increasing diffraction peak shift indicates an increasing degree in the macrostrain of the material and correlates with the increase in the measured stress.[68] Similar lattice expansions and diffraction peak broadening have been reported for ZrO_2 deposited by reactive ion beam sputtering of a Zr target, though the peak broadening was considered only due to crystallite size changes.[71] Similar lattice expansion, due to interstitial nitrogen incorporation, has also been reported in reactively-sputtered W_2N films when the reactive gas concentration in the chamber was increased during sputtering.[77] We attribute the lattice expansion and the associated stress in the scandia films to increasing interstitial oxygen incorporation in the film matrix.

Chapter 4

Conclusions and Future Work

The motivation of the work presented in this thesis was to explore Sc_2O_3 as a high-index material for interference coatings that will enable the power scaling of high-power lasers that operate in the near-infrared wavelength regime with sub-picosecond pulsewidths. Scandia deposited via ion beam sputtering (IBS) potentially has a higher damage threshold than hafnia, which is currently used in high-power laser optical coatings. The work presented here is the first in investigating scandia via IBS. It was found that the properties of the scandia films are sensitive to the oxygen partial pressure in the chamber during deposition. A minimum in the absorption loss at $\lambda = 1.064$ µm was 10 ppm at 5 µTorr oxygen partial pressure. When less oxygen existed in the chamber, the films deposited were metallic and highly absorbing. Above the optimum oxygen partial pressure, the 1-µm absorption loss increased. This behavior results from an increase of shallow level defects that are separated by ≤ 1.165 eV from either the conduction band or valence band states. This is confirmed by absorption measurements in the UV, near the optical band edge of the material. These defects are likely to have unpaired electrons as determined from electron paramagnetic resonance (EPR) measurements. EPR measurements showed that above the optimum partial pressure, the density of unpaired electrons in the scandia films increased with increasing oxygen partial pressure. These unpaired electrons possibly are a result of interstitial O_2^- ions as suggested by previous work done on similar metal oxides. An increase of 3 times in defect-related oxygen is observed in O 1s XPS spectra in a film

deposited at 38 μTorr compared to the film deposited at $p = 5$ μTorr. The presence of interstitial oxygen is also suggested by XRD data, which show that increased partial pressures cause the diffraction peak to shift, evidence of increasing film macrostrain, and increasing peak widths (evidence of increasing microstrain or decreasing crystallite size). The measured increase in macrostrain from XRD corresponds with the increase in film stress, from 0.77 GPa at $p = 5$ μTorr to 1.19 GPa at $p = 40$ μTorr.

To be comparable to the best available coatings, scandia layers need to have total losses $\lesssim 1$ ppm. The absorption loss in a single layer needs to be reduced at least an order of magnitude. It is important to state that no annealing work was done on the films presented here. It is possible to reduce the absorption loss with post-deposition annealing. The scattering losses, which are related to surface roughness, must be eventually measured. Also, the damage threshold of scandia needs to be reliably tested against the current standards, like hafnia.

The work suggests the defects investigated here are excess oxygen, therefore, future work should include studies that lead to the understanding of how the excess oxygen incorporates into the film so that the defect incorporation can be mitigated.

To improve the properties of scandia films, more dimensions in the deposition parameter space should be explored, such as assist beam energy and flux, target purity and pure metal versus pure oxide sputtering targets. Post-deposition annealing recipes should also be investigated in terms of annealing temperature, time and atmosphere.

References

[1] E. Hecht, *Optics*, Addison Wesley, 2002.

[2] Jefferson National Laboratory, *http://www.jlab.org/FEL/feldescrip.html*, April 2010.

[3] A. W. Thomas, G. P. Williams, "The free electron laser at Jefferson Lab: the technology and the science," *Proc. IEEE* **95**, p. 1679, 2007.

[4] E. J. Montgomery, D. W. Feldman, P. G. O'Shea, Z. Pan, N. A. Moody, K. L. Jensen, "Fabrication and measurement of effecient, robust cesiated dispenser photocathodes," *Proc. PAC07* **TUPMS010**, p. 1206, 2007.

[5] Cornell University Superconducting Radio Frequency Group, *http://www.lepp.cornell.edu/Research/AP/SRF/SrfCavitiesAPrimer.html*, April 2010.

[6] J. M. J. Madey, "Stimulated emission of Bremsstrahlung in a periodic magnetic field," *J. Appl. Phys.* **42**, p. 1906, 1971.

[7] M. Shinn, C. Behre, S. Benson, D. Douglas, F. Dylla, C. Gould, J. Gubeli, D. Hardy, K. Jordan, G. Neil, S. Zhang, "Xtreme optics–the behavior of cavity optics for the Jefferson Lab free-electron laser," *Proc. SPIE* **6403**, p. 64030Y, 2006.

[8] M. Shinn, C. Behre, S. Benson, M. Bevins, D. Bullard, J. Coleman, L. Dillon-Townes, T. Elliot, J. Gubeli, D. Hardy, K. Jordan, R. Lassiter, G. Neil, S. Zhang, "High average power operation of a scraper-outcoupled free-electron laser," *Proc. FEL Conf.* **TUBOS03**, p. 222, 2004.

[9] H. A. Macleod, *Thin-Film Optical Filters*, Institute of Physics Publications, 2001.

[10] P. W. Baumeister, *Optical Coating Technology*, SPIE Press, 2004.

[11] E. Welsch, eds. R. E. Hummel, K. H. Guenther, *Handbook of Optical Properties*, CRC Press, 1995.

[12] D. J. Griffiths, *Introduction to Quantum Mechanics*, Pearson Prentice Hall, 2005.

[13] M. S. Tyagi, *Introduction to Semiconductor Materials and Devices*, John Wiley and Sons, 1991.

[14] J. S. Blakemore, *Solid State Physics*, W. B. Saunders Company, 1974.

[15] A. Alexandrovski, M. Fejer, A. Markosyan, R. Route, "Photothermal common-path interferometry (PCI): new developments," *Proc. SPIE* **7193**, p. 71930D, 2009.

[16] M. Mero, J. Liu, W. Rudolph, D. Ristau, K. Starke, "Scaling laws of femtosecond laser pulse induced breakdown in oxide films," *Phys. Rev. B* **71**, p. 115109, 2005.

[17] D. Grosso, P. A. Sermon, "Scandia optical coatings for application at 351 nm," *Thin Solid Films* **368**, p. 116, 2000.

[18] A. M. Herrero, B. P. Gila, C. R. Abernathy, S. J. Pearton, V. Craciun, K. Siebein, F. Ren, "Epitaxial growth of Sc_2O_3 films on GaN," *Appl. Phys. Lett.* **89**, p. 092117, 2006.

[19] D. Adler, eds. H. Fritzsche, D. Han, C. C. Tsai, *Proceedings of the International Workshop on Amorphous Semiconductors*, World Scientific Publishing, 1987.

[20] CVI Lasers, LLC., *www.cvimellesgriot.com/products/Documents/HELaserDamage.pdf*, April 2010.

[21] B. C. Stuart, M. D. Feit, S. Herman, A. M. Rubenchik, B. W. Shore, M. D. Perry, "Optical ablation by high-power short-pulse lasers," *J. Opt. Soc. Am. B* **13**, p. 459, 1996.

[22] B. Rethfeld, K. Sokolowski-Tinten, D. Von Der Linde, A. I. Anisimov, "Timescales in the response of materials to femtosecond laser excitation," *Appl. Phys. A.* **79**, p. 767, 2004.

[23] C. W. Carr, H. B. Radousky, S. G. Demos, "Wavelength dependence of laser-induced damage: determining the damage initiation mechanisms," *Phys. Rev. Lett.* **91**, p. 127402, 2003.

[24] D. N. Nguyen, L. A. Emmert, M. Mero, W. Rudolph, D. Patel, E. Krous, C. S. Menoni, "The effect of annealing on the subpicosecond breakdown behavior of hafnia films," *Proc. SPIE* **7132**, p. 71320N, 2008.

[25] W. Kern, V. S. Ban, eds. J. L. Vossen, W. Kern, *Thin Film Processes*, Academic Press, 1978.

[26] P. L. Houston, *Chemical Kinetics and Reaction Dynamics*, Dover Publications, 2001.

[27] J. S. Becker, *Atomic Layer Deposition of Metal Oxide and Nitride Thin Films*. PhD thesis, Harvard University, 2002.

[28] O. Lyngnes, N. Traggis, K. L. Dessau, C. Myatt, "Coating technologies for high-damage-threshold optics," tech. rep., Precision Photonics Corporation, 2006.

[29] L. Gallais, J. Capoulade, J. Y. Natoli, M. Commandré, M. Cathelinaud, C. Koc, M. Lequime, "Laser damage resistance of hafnia thin films deposited by electron beam deposition, reactive low voltage ion plating, and dual ion beam sputtering," *Appl. Opt.* **47**, p. C107, 2008.

[30] P. C. Zalm, eds. J. J. Cuomo, S. M. Rossnagel, H. R. Kaufman, *Handbook of Ion Beam Processing Technology*, Noyes Publications, 1989.

[31] P. J. Martin, R. P. Netterfield, eds. J. J. Cuomo, S. M. Rossnagel, H. R. Kaufman, *Handbook of Ion Beam Processing Technology*, Noyes Publications, 1989.

[32] R. Herrmann, G. Bräuer, eds. R. E. Hummel, K. H. Guenther, *Handbook of Optical Properties*, CRC Press, 1995.

[33] Precision Photonics Corporation, *http://www.precisionphotonics.com/individual-_technology_tp.asp?id=6*, April 2010.

[34] Advanced Thin Films, *http://www.atfilms.com/technology.html*, April 2010.

[35] MLD Technologies, LLC., *http://www.mldtech.com/technology.php*, April 2010.

[36] J. Becker, eds. R. E. Hummel, K. H. Guenther, *Handbook of Optical Properties*, CRC Press, 1995.

[37] J. M. E. Harper eds. J. L. Vossen, W. Kern, *Thin Film Processes*, Academic Press, 1978.

[38] F. Rainer, W. H. Lowdermilk, D. Milam, T. Tuttle Hart, T. L. Lichtenstein, C. K. Carniglia, "Scandium oxide coatings for high-power UV laser applications," *Appl. Opt.* **21**, p. 3685, 1982.

[39] S. Tamura, S. Kimura, Y. Sato, H. Yoshida, K. Yoshida, "Laser-damage threshold of Sc_2O_3/SiO_2 high reflector coatings for a laser wavelength of 355 nm," *Thin Solid Films* **228**, p. 222, 1993.

[40] Z. Xu, A. Daga, H. Chen, "Microstructure and optical properties of scandium oxide thin films prepared by metalorganic chemical-vapor deposition," *Appl. Phys. Lett.* **79**, p. 3782, 2001.

[41] M. F. Al-Kuhaili, "Optical properties of scandium oxide films prepared by electron beam evaporation," *Thin Solid Films* **426**, p. 178, 2003.

[42] W. Heitmann, "Reactively evaporated films of scandia and yttria," *Appl. Opt.* **12**, p. 394, 1973.

[43] P. de Rouffignac, A. P. Yousef, K. H. Kim, R. G. Gordon, "ALD of scandium oxide from scandium tris(*N*,*N*'-diisopropylacetamidinate) and water," *Electrochem. Solid-State Lett.* **9**, p. F45, 2006.

[44] C. Liu, E. F. Chor, L. S. Tan, "Epitaxial growth of Sc_2O_3 films on GaN (0001) by pulsed laser deposition," *J. Vac. Sci. Technol. B* **25**, p. 754, 2007.

[45] Veeco-Ion Tech, Inc., 2330 East Prospect, Fort Collins, CO 80525, Spector user's manual, 1999.

[46] Helix Technology Corporation, Nine Hampshire St., Mansfield, MA 02048, On-Board Cryopump Installation and Maintenance Instructions, 1999.

[47] Inficon, Two Technology Place East Syracuse, NY 13057, *Transpector2 Gas Analysis System Operating Manual*, 2000.

[48] Advanced Energy Industries, Inc., 1625 Sharp Point Dr. Fort Collins, CO 80524, Inductively Coupled Plasma Source (ICP) User Manual, 2001.

[49] A. Fitzgerald Dummer, "Ion-Beam Sputter Deposition of High Damage Threshold Oxide Multilayers for Short-Pulse Laser Applications," Master's thesis, Colorado State University, 2005.

[50] F. F. Chen, *Introduction to Plasma Physics and Controlled Fusion*, vol. 1, Plenum Press, 2nd ed., 1983.

[51] G. Franz, *Low Pressure Plasmas and Microstructuring Technology*, ch. 8. Springer, 2009.

[52] J. J. Cuomo, S. M. Rossnagel, H. R. Kaufman, *Handbook of Ion Beam Processing Technology*, Noyes Publications, 1989.

[53] H. Neumann, M. Tartz, F. Scholze, T. Chassé, H. Kersten, H. Leiter, "Broad beam ion sources for electrostatic space propulsion and surface modification processes: from roots to present applications," *Contrib. Plasma Phys.* **47**, p. 487, 2007.

[54] J.-C. Pivin, "An overview of ion sputtering physics and practical implications," *J. Mater. Sci* **18**, p. 1267, 1983.

[55] A. A. Barybin, V. I. Shapovalov, "Nonisothermal chemical model of reactive sputtering," *J. Appl. Phys.* **101**, p. 054905, 2007.

[56] S. Berg, T. Nyberg, "Fundamental understanding and modeling of reactive sputtering processes," *Thin Solid Films* **476**, p. 215, 2005.

[57] N. Kaiser, "Review of fundamentals of film growth," *Appl. Opt.* **41**, p. 3053, 2002.

[58] P. C. Hiemenz, R. Rajagopalan, *Principles of Colloid and Surface Chemistry*, CRC Press, 1997.

[59] K.-H. Muller, eds. J. J. Cuomo, S. M. Rossnagel, H. R. Kaufman, *Handbook of Ion Beam Processing Technology*, Noyes Publications, 1989.

[60] D. Patel, P. Langston, A. Markosyan, E. M. Krous, B. Langdon, F. Furch, B. Reagan, R. Route, M. M. Fejer, J. J. Rocca, C. S. Menoni, "SiO_2/HfO_2 multilayers: impact of process parameters and stack geometry on the optical and structural properties," *Proc. SPIE* **7132**, p. 71320L, 2008.

[61] S. Schiller, G. Beister, W. Sieber, "Reactive high rate DC sputtering: deposition rate, stoichiometry and features of TiO_x and TiN_x films with respect to the target mode," *Thin Solid Films* **111**, p. 259, 1984.

[62] Hitachi Instruments, Inc., 3100 North First Street San Jose, CA 95134, *Model U-2010 UV/Vis Spectrophotometer Users Manual*, 1996.

[63] Stanford Photo-Thermal Solutions, *http://www.stan-pts.com/howitworks.html*, May 2010.

[64] J. A. Woollam Co., Inc., 645 M Street, Suite 102 Lincoln, NE 68508, *Guide to Using WVASE32*.

[65] J. A. Weil, J. R. Bolton, *Electron Paramagnetic Resonance: Elementary Theory and Practical Applications*, John Wiley and Sons, Inc., 2007.

[66] R. T. Weber, J. J. Jiang, D. P. Barr, *EMX User's Manual*. EPR Division, Bruker Instruments, Inc., 19 Fortune Drive, Manning Park, Billerica, MA 01821, 1998.

[67] S. Stoll, A. Schweiger, "EasySpin, a comprehensive software package for spectral simulation and analysis in EPR," *J. Magn. Reson.* **178**, p. 42, 2006.

[68] B. D. Cullity, *Elements of X-Ray Diffraction*, Addison-Wesley Publishing Company, 1959.

[69] P. A. Flinn, D. S. Gardner, W. D. Nix, "Measurement and interpretation of stress in aluminum-based metallization as a function of thermal history," *IEEE Trans. Electron Devices* **ED-34**, p. 689, 1987.

[70] J. I. Langford, A. J. C. Wilson, "Scherrer after sixty years: a survey and some new results in the determination of crystallite size," *J. Appl. Cryst.* **11**, p. 102, 1978.

[71] M. Yoshitake, K. Takiguchi, Y. Suzuki, S. Ogawa, "Effects of oxygen partial pressure in reactive ion beam sputter deposition of zirconium oxides," *J. Vac. Sci. Technol. A* **6**, p. 2326, 1988.

[72] A. Pérez-Pacheco, C. Prieto, R. Castañeda-Guzmán, J. García-López, "Influence of the growth conditions on the stoichiometry and on the optical properties of titanium oxide thin films prepared by reactive sputtering," *Thin Solid Films* **517**, p. 5418, 2009.

[73] J.-G. Li, T. Ikegami, T. Mori, "Fabrication of transparent, sintered Sc_2O_3 ceramics," *J. Am. Ceram. Soc.* **88**, p. 817, 2005.

[74] M.-T. Ho, Y. Wang, R. T. Brewer, L. S. Wielunski, Y. J. Chabal, "In situ infrared spectroscopy of hafnium oxide growth on hydrogen-terminated silicon surfaces by atomic layer deposition," *Appl. Phys. Lett.* **87**, p. 133103, 2005.

[75] R. C. Barklie, S. Wright, "Electron paramagnetic resonance characterization of defects in HfO_2 and ZrO_2 powders and films," *J. Vac. Sci. Technol. B* **27**, p. 317, 2009.

[76] J. Akella, J. Xu, G. S. Smith, "Static high pressure studies on Nd and Sc," *Physica B + C* **139**, p. 285, 1986.

[77] C. C. Baker, S. I. Shah, "Reactive sputter deposition of tungsten nitride thin films," *J. Vac. Sci. Technol. A* **20**, p. 1699, 2002.